Heat Storage Based on PCM for Concentrated Solar Power Applications

With $NaNO_3$-KNO_3 eutectic mixture as PCM

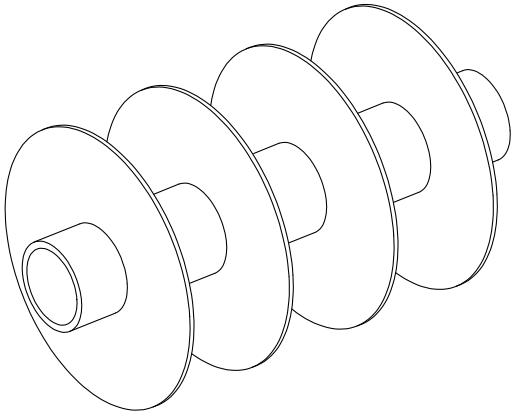

MASTER'S THESIS

within

THERMAL ENERGY AND PROCESS ENGINEERING

by

JAN KRAGBÆK & NIS PETER REINHOLDT

Department of Energy Technology
University of Aalborg, Denmark

June 9*th* 2011

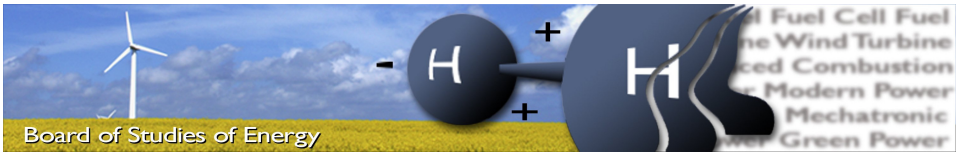

Title:	Heat Storage Based on PCM for Concentrated Solar Power Applications
Semester:	4*th*, Thermal Energy and Process Engineering
Semester theme:	Master's Thesis
Project period:	01.02.2011 - 09.06.2011
ECTS:	30
Supervisor:	Thomas Joseph Condra, Aalborg University
Project group:	TEPE4-1040

Jan KRAGBÆK

Nis Peter REINHOLDT

ABSTRACT:

The purpose of this work was to investigate heat transfer in a KNO_3-$NaNO_3$-based PCM heat storage for concentrated solar power applications. This was done by appling a CFD tool and a numerical approach. The work was done in three stages, covering quasi-1D, 2D and finally 3D. Results were based on evaluation of two models with graphite and steel fins, respectively. Each model was simulated for 3, 10, 30 and 60 minutes. The conclusion of this work was that the choice of the fin material was of less importance during discharge mode, as PCM solidifies on the heating surfaces, which acts as a thermal insulator. This results in reduced heat transfer through the heating surface. Furthermore, it was discovered that natural convection in the liquid PCM was of great importance to the heat transfer.

Copies:	5
Pages, total:	136
Appendices:	6
Supplements:	None

By signing this document, each member of the group confirms that all participated in the project work and thereby all members are collectively liable for the content of the report.

Preface

This report is a Master's Thesis from Aalborg University, Denmark, within the field of Thermal Energy and Process Engineering at The Department of Energy Technology. The topic of the report is heat transfer and phase change in connection with the heating surface of a latent thermal heat storage. It is the result of the investigation of a new design for a heat storage as proposed by the Aalborg-based engineering company Aalborg CSP which specialises in steam generators for concentrated solar power plants. In connection with the making of this report, the authors would like to extend a special thanks to a number of people: Søren Bøgh, M.Sc., Project Manager at Aalborg CSP; Matthias Mandø, PhD, Institute of Energy Technology, Aalborg University Esbjerg; Chungen Yin, PhD, Department of Energy Technology, Aalborg University; and Mikael Larsen, PhD, Department of Mechanical and Manufacturing Engineering, Aalborg University. Mr. Matthias Mandø and Mr. Chungen Yin have provided guidance with respect to the CFD aspect of the project, and Mr. Mikael Larsen have been consulted in the regard of nitrate salt microstructures and its solidification process. Mr. Søren Bøgh have provided data for pratical solutions and design criteria.
Regarding the software used for providing the results presented in this report, MathWorks MATLAB is used to numerically calculate the heat transmission in the Stefan-type problem encountered in this work. For CFD simulations, the commercial software ANSYS FLUENT is used. Both programs are provided by Aalborg University and used under the given licences connected hereto.

Contact information of the authors is given below.

- Jan Kragbæk; tlf.: (+45) 20 12 92 97, email: jan@kragbaek.dk
- Nis Peter Reinholdt; tlf.: (+45) 22 76 74 79, email: peter_reinholdt@mail.com

The frontmatter of this report includes a summary, the table of contents, lists of appearing figures and tables, and a list explaining the nomenclature. The main body of this text is comprised of four major parts, named: *Introduction*, *Quasi-1D study*, *2D study* and *3D study*. The first part describes the motive and perspectives of this investigation, and presents the necessary background information for the reader to fully appreciate the remaining parts. Moreover, it contains the problem statement which is located in chapter 3. The second part concentrates on a relatively simple numerical model compared to a CFD constructed numerical model in 1D. Third part includes 2D in the CFD numerical model, where more aspects are included. The fourth part focuses on a 3D CFD numerical model. Finally, a bibliography and appendices follows after the main part of the text. Citations are done as prescribed by the Chicago-method, which in text is given as (Author, Year). With the report

is given a CD containing the report in PDF format, necessary files to run MATLAB models of various aspects of the problem investigated, and case files from the CFD analysis. The CD is placed on the last page in this report.
All specifications of pressures are presented in the form of absolute pressure throughout this report, meaning bar = bar(a).

Project Summary

The scope of the project is to study the heat transfer and phase change mechanisms of a latent heat storage facility for concentrated solar power plants. The aim of the investigation is to determine a suitable design for the heating surface with the storage unit. The work in this report is based on an idea for a simple design concept involving a stationary phase change material. This idea for future development of storage units was set forth by an engineering company with in the field of concentrated solar power. The phase change material used in the storage considered, is an eutectic composition of potassium nitrate and sodium nitrate salt ($NaNO_3$-KNO_3), which possesses a number of advantageous properties with respect to stability, corrosion, and price. A commercial CFD software and programmed model using a numerical mathematical method were the primary tool used in the present work. CFD simulations were carried out for one, two and three dimensions, while the numerical model was limited to considering 1D problems only, however, good similarity was seen in the 1D-based results for the model and the CFD simulations.

The 2D and 3D aspects of the CFD work included modelling of natural convection flows occurring in the liquid phase change material. Results of the investigation indicated that buoyancy driven natural convection has a significant impact on heat transfer and shape of the solid-liquid interface. Furthermore, studies suggested that the choice of fin material for the heating surface was of minor importance when considering the discharge aspect of the heat storage. This was due to the thermal resistance associated with deposition of solid phase change material on the heating surface being the limiting factor of heat transfer.

Contents

Contents **xi**

List of Figures **xv**

List of Tables **xx**

Nomenclature **xxiii**
Subscripts xxiv
Abbreviations xxiv

I Introduction **1**

1 Introduction **3**
1.1 Heat Storage in Solar Power Applications 3
1.2 State-of-the-Art 7

2 Project Background **15**
2.1 Heat Storage Configurations for CSP 15
2.2 Requirement Specification 19
2.3 Initial Problem 20
2.4 Project Outline 20

3 Problem Statement **23**
3.1 Problem Definition 23
3.2 Methods and Delimitation 23

II Quasi-1D Study **25**

4 Material Properties **27**
4.1 Thermophysical Material Properties 27
4.2 Microstructures 34
4.3 PCM Stability 37
4.4 Corrosion 38
4.5 Summary of Material Properties 40

5 General Modelling Approach **43**
5.1 Quasi-1D Geometry 43
5.2 Boundary Conditions and Assumptions 44
5.3 Boundary Condition Simplification 45
5.4 Delimitation - Charge mode modelling in 2D 47

6 Quasi-1D CFD Analysis **49**
6.1 Governing Equations and the Solidification Model 49
6.2 Solver Settings in FLUENT 52
6.3 Quasi-1D CFD Simulation Presentation 55
6.4 Grid Independence 56
6.5 Grid Quality 59
6.6 Quasi-1D CFD Results 60

7 Quasi-1D Numerical Model **65**
7.1 Overall Heat Transfer Coefficient 65
7.2 Numerical model 70
7.3 Heat Balance 71
7.4 Phase Change Model 72
7.5 Time Step Analysis 75
7.6 Grid Independency Analysis 77
7.7 Results 78
7.8 Computational Time 79
7.9 Model Validation 81

III 2D Study **83**

8 Natural Convection Contribution **85**
8.1 Volume Expansion Coefficient 85
8.2 Grashof number 85
8.3 Prandtl number 86
8.4 Nusselt number 86
8.5 Evaluation of Natural Convection Present 86

9 Finned Tubes **89**
9.1 Finned Surfaces in Latent Heat Storage Applications 89
9.2 Fin Efficiency 90
9.3 Finned Tube Material Consumption and Design Selection 98

10 2D CFD Analysis **103**
10.1 2D Simulation of Smooth Vertical Pipe 103
10.2 2D Simulation of Circular Annular Finned Tube 109
10.3 Summary of 2D CFD Analysis 112

IV 3D Study **115**

11 3D CFD Analysis **117**
11.1 3D Grid Independence 118
11.2 3D CFD Results 122
11.3 Summary of 3D CFD Analysis 126

12 Heating Surface Design **127**

12.1 Future Work 130

13 Conclusion **131**

Bibliography **133**

V Appendices **137**

A Parabolic Trough Collectors **139**

B Weight Loss and Thermal Cycling of Ternary Salt Mixture **147**

C Steamlines in the Liquid Melt Around a Vertical Pipe **149**

D Practical Approach of CFD-simulations **151**

E Fin Efficiency Plots **153**

F Mail Correspondence, Nitrate Salt Properties **155**

List of Figures

1.1 EuroTrough parabolic trough collector prototype. Taken from Price et al. (2002) . . . 3
1.2 Power productionof a CSP plant during a day. To illustrate an example, a midsummer day in Aalborg Denmark is shown. The data are obtained from a program developed by Mr. Palle Wendelboe (Aalborg CSP). . . . 4
1.3 Illustration of feasible locations for CSP plants. The figure is based on average annual ground solar energy (1983-2005) - Clear sky insolation incident horizontal surface [kWh/m^2/day]. . . . 4
1.4 Example of daily electricity price and production fluctuations for the Danish electricity grid in 2010. Note the Y-axis starting point (Energinet.dk, 2011). . . . 5
1.5 When heat storage is used in a CSP plant, power production is evened out. 6
1.6 Example of isentropic efficiency curve for a steam turbine as a function of mass flow rate in T/h (Bloch, 1995). . . . 6
1.7 Stiff-walled capsules filled with KNO_3-$NaNO_3$ and gas ready for testing, and a plot of the effect of initial gas volume in the capsules. Taken from Steinmann and Tamme (2008). . . . 9
1.8 Graphite matrix infiltrated with PCM and cyclic behaviour of a cold compressed compound. Taken from Pincemin et al. (2008). . . . 10
1.9 Composite material heat storage unit and proved effect of graphite content in the composite. Quantities are presented as mass fraction. Taken from Steinmann and Tamme (2008). . . . 10
1.10 Annual electricity production in countries surrounding the Mediterranean and countries of the Arabian Peninsula considered in the scenario of the MED-CSP study. From DLR (2005). . . . 12

2.1 Illustration of steam accumulator. . . . 16
2.2 Illustration of two tank molten storage at two different states. . . . 17
2.3 Illustration of proposed PCM subjected to further investigation in this report. Here schematics are shown for charge and discharge stages. . . . 18
2.4 Suggestion for main study areas of the heat storage project from Aalborg CSP. . . . 20

4.1 Composition dependence of the thermal conductivity of KNO_3-$NaNO_3$ system as given in Omotani et al. (1982). . . . 29
4.2 Thermophysical properties of molten salt $NaNO_3$-KNO_3 60/40 mass % in the temperature range 270 to 600 °C Pacheco et al. (1995). Original data are marked, while the curve fits in equations 4.2 to 4.5 are represented with a solid line. . . . 33
4.3 The classical binary phase diagram. From Kerridge et al. (2009). . . . 35

4.4 A phase diagram of the KNO_3-$NaNO_3$ system as presented in Zhang et al. (2003). 35
4.5 Forming of a lamellar microstructure during nucleation due to molecular diffusion of the two phases α and β. Taken from Kerridge et al. (2009). 36
4.6 DSC and DTA experiments with of sodium and potassium nitrates and nitrites. Taken from Kramer et al. (1982). 38
4.7 Experimental results of corrosion rates in terms of descaled carbon steel weight loss. Please note that #1 denotes a low-chloride salt composition and #7 denotes a highly impure salt composition with a high chloride concentration. Taken from Goods and Bradshaw (2004). 39
4.8 Plant schematics of Solar Two. Taken from Herrmann and Kearney (2002). 40

5.1 Illustration of the quasi-1D domain. Please notice the emphasised section, which illustrates the one dimensional plane. 44
5.2 The figure shows how HTF is let in to the pipe, and how the temperature of the HTF is increased as it flows along the x-axis. The numbers in the circles indicate different time scenarios. The higher the number, the longer the time. 46
5.3 Schematics of the example "melting around a vertical pipe". Taken from Patankar (1980). 47

6.1 Section close-up of grid 100. 55
6.2 Full view of the grid (denoted *grid 100*) used for the quasi-1D simulation. 56
6.3 Time dependent temperature profiles of the PCM evaluated along a line in the radial direction. Here shown for an example of discharge mode. . 57
6.4 Temperature profiles of the grids reviewed in the grid independency study (discharge mode 1, 10 minutes). 58
6.5 Computational time for the reviewed grids. Note that the sudden jump in computational time from grid 100 to grid 375 is caused by significant increase in the number of cells. 58
6.6 Angles and areas used for evaluation of angular skewness and size change of cells. Here showed for a 2D grid. Reproduced by the authors from Mandø (2009). 60
6.7 Residuals of the energy equation for the 1D CFD simulation. A fixed time step size of 0.1 s is applied. 61
6.8 Temperature contours of the four simulation periods; 3, 10, 30 and 60 minutes, depicted in each corner of the figure. Note the temperature scale is presented in K. 62
6.9 Contours of the solid/liqiud fraction shown for the four simulation periods; 3, 10, 30 and 60 minutes. 63
6.10 Distorted interface shape experienced with second order schemes. Depicted here for 30 minutes. 63
6.11 Temperature profile in the radial direction. 64
6.12 Plot of the liquid fraction vs. time and radial position. 64

7.1 Illustration of the heat transfer through pipe wall and solid PCM. . . . 66

7.2 Presentation of thermal resistance in PCM layer as a function of layer thickness. Inner radius is set as equal to the outer radius of the pipe, and is thereby fixed. 69
7.3 Illustration of a node volume. 70
7.4 The absolute value of heat flux is decreasing with time according the decrease in temperature difference. The steps are due to phase change in nodal points. 72
7.5 The diagram shows how the phase change is evaluated, and how temperature is regulated according to phase change (diagram produced by the authors). 75
7.6 Temperature plot of simulations with three different time steps. All have 100 nodal points in radial direction and a starting temperature of 251 °C and HFT temperature of 180°C 76
7.7 Temperature profile of evaluated grid sizes for each simulation time. . . 78
7.8 Temperature plot of four different simulation times, showing the temperature distribution in the PCM. 79
7.9 Plot of temperature profiles from the CFD analysis and the numerical model at a simulation time of 10 minutes. 81

8.1 Plot of non-dimensional density with a pipe temperature of 275°C and a PCM temperature of 221°C 87

9.1 Charge state vs. time for various fin thicknesses of steel fins compared to graphite fins and a plain tube. Taken from Laing et al. (2009). 90
9.2 Section cut view of a pipe with circular fins and corresponding nomenclature adopted from Brandt (1985) for pipe and fin dimensions. 92
9.3 Efficiency of circular steel fins vs. fin height and pitch l_p, discharge mode 1. 95
9.4 Efficiency of circular graphite fins vs. fin height and pitch l_p, discharge mode 1. 96
9.5 Section cut view of the Sunrod tube and corresponding nomenclature for pipe and fin dimensions. 97
9.6 Efficiency of pins on the Sunrod tube as a function of pin length and diameter. 98
9.7 Volume of fin material vs. fin efficiency for the Sunrod tube. 98
9.8 Volumetric material use for the selected fins per meter of pipe. 100

10.1 Grid and geometrical ratios of the 2D smooth vertical pipe computational domain. 104
10.2 Temperature profiles along the x-axis of the domain cf. figure 10.2 for the three grids of the grid independence study. Shown for discharge mode 1, 10 minutes. 105
10.3 Solid-liquid interface of grids 24, 100, and 240. Included are all cells with liquid fraction from 0 to 0.7. Discharge mode 1, 10 minutes elapsed time. Note that the white triangles are merely graphical errors without connection to the solution. 105

10.4 Velocity vector plot of the start-up behaviour shown for 2, 4.5 , and 7 minutes. Note the scale is presented in $^m/_s$. Discharge mode 1. 106
10.5 Temperature contours of both modes of discharge after 60 minutes elapsed time. Graphics are produced by reflection around the y-axis (see figure 10.1). Note temperature scales are presented in K. 107
10.6 Contours of liquid fraction for discharge modes 1 and 2 after 60 minutes simulation time. Graphics are reflected with respect to the y-axis (see figure 10.1). 107
10.7 Section cut view of a pipe with circular fins, and a presentation of the CFD grid. 109
10.8 Temperature profiles of the grids considered for the grid independency study (discharge mode 1, 10 minutes simulation time). 110
10.9 Residuals of the first 16 time steps of the discharge 1 simulation. 111
10.10Contour plots of temperature in the computational domain after 60 minutes of elapsed time. Note that plots are reflected around the left vertical boundary of the domain and that temperatures are presented in K. . . . 112
10.11Liquid fraction contours for both modes of discharge. Evaluated after 60 minutes. Plots are reflected around the left vertical boundary of the domain. 112

11.1 Tube with circular fins marked with the section considered for the 3D computational domain. 117
11.2 Presentation of pipe grid from two differenct views. The figure clearly shows the grading in the axial direction. 118
11.3 Presentation of the grid of the fin in radial direction. It is clearly shown, that the radial grading ensures a low change in aspect ratio. 119
11.4 The fin edges only contains few cells across. No grading is present. . . . 119
11.5 The figure presents the domain which only contains PCM. 120
11.6 Temperature plot for five different grid sizes. 121
11.7 Convergence history for the 3D simulation for the pipe with circular fins. 122
11.8 Illustration of the location of the five planes. 123
11.9 All five planes are presented here. From left to right, it is north, north-east, east, south-east and south, according to figure 11.8a. Presented here is 2 mm graphite fins after 60 minuts of simulation time. 123
11.10Steel fins are here modelled and presented in the five planes. From left to right, it is north, north-east, east, south-east and south, according to figure 11.8a. 124
11.11Liquid fraction for both graphite and steel fins is plotted according to the four simulation times. 125
11.12Heat flux as a function of simulation time. This is applicable for both graphite and steel fins. 125
11.13The figure shows the behavior of the PCM mean temperature as a function of simulation time. 126

12.1 Temperature plot of north face with graphite fins. 127
12.2 Illustration of the design changes purposed. 128

12.3 Plot of teh heat flux of the new fin designs. The new models are simulated for 3 and 10 minutes. 129
12.4 To ensure minimum risk of damage during tube bend, a minimum bending radius is used. This bend is illustrated in the figure. 129
12.5 When placing fins on a tube, it must be considered according to the neighboring tube. This is to reduce risk of fin contact. 130

A.1 MW_e of collector technology used in CSP plants worldwide currently under construction. Number are of 2010. Plot reproduced by the authors with data from Baker et al. (2010). 139
A.2 MW_e of collector technology of planned CSP plants worldwide. Number are of 2010. Plot reproduced by the authors with data from Baker et al. (2010). 140
A.3 Characteristics of SEGS I through IX in Kramer Junction, California, and characteristics of different of parabolic trough collector designs. From Price et al. (2002). 141
A.4 Installed CSP capacity in relation to countries and collector technology as reported by 2010. Plots reproduced by the authors with data from Baker et al. (2010). 142
A.5 Details of the double pipe absorber design. Taken from Price et al. (2002). 143
A.6 Schematics of the once through and recirculation processes of DSG. Modified from Price et al. (2002). 145
A.7 Operation in once-through mode at 60 bar. From Zarza et al. (2004). . . 145

B.1 Weight loss plotted against temperature for ternary nitrate salt. Taken from Peng et al. (2010). 147
B.2 Cooling curve of 14 thermal cycles of ternary nitrate salt ($NaNO_3$, KNO_3 and $NaNO_2$, 7/53/40 mass %). Taken from Peng et al. (2010). 147

C.1 Representative streamlines of the fluid flow. (a) shows the rectangular shape of the cavity at small simulation times, while (b) and (c) clearly shows the effects of heat transfer dominated by natural convection at later times. Taken from Patankar (1980). 149

D.1 Sketch of the basic communication between a student laptop and the computational cluster at The Department of Energy Technology, Aalborg University. 152

E.1 Fin efficiency vs. fin height and pitch c_{Ro}. 1 mm thick circular steel fin, discharge mode 1. 153
E.2 Fin efficiency vs. fin height and pitch c_{Ro}. 3 mm thick circular expanded graphite fin, discharge mode 1. 153

F.1 Mail correspondence with Mr. Nils Gathmann of Flagsol GmbH 155

List of Tables

2.1 Technologies used at present time and technologies emerging. 15
2.2 The energy stored in each system is calculated by the specific heat capacity at maximum and minimum temperature. If latent heat is utilised this is added to the total energy. Stored energy is based on one kg of storage material. 18
2.3 The table presents the minimum and maximum pressure and temperatures the power plants work under. The data is to be used for specifying design of the heat storage. 19

4.1 Thermal properties of steel type St.35.8. Taken from Witte (1976) and LOGSTOR (2011). 27
4.2 Chemical composition of alloy elements in steel type St.35.8. Taken from Witte (1976). 28
4.3 Thermal properties of expanded graphite. Taken from and Bayón et al. (2010). 28
4.4 Thermal properties of potassium and sodium nitrate salt mixtures found in the literature. Please note this table is compiled by the authors. . . . 30
4.5 Thermal properties of the potassium and sodium nitrate salt composition used in the analysis of the phase change process. 31

5.1 Dimensions of the quasi-1D modelling domain. 44
5.2 Boundary and initial temperatures suggested for the quasi-1D study. Two examples each of the charge and discharge modes are chosen. 45
5.3 Simulation times at which the progress of melting/solidifying PCM is evaluated. 45

6.1 Absolute convergence criteria of the computation residual used for all CFD simulations. 54
6.2 Grid size details of the six grids considered for the grid independency study. 56
6.3 Characteristic numbers of the grid quality. 60

7.1 Heat transfer coefficient for the different scenarios evalutated for the temperatures presented in table 5.2. 68
7.2 Thermal resistances for condensation and boiling of HTF and conduction in PCM. 70
7.3 List of amounts of energy for different simulations times and modes. All energy amounts in discharge mode are negative, as energy is drawn out of the system. 72
7.4 Standard deviations for a 1D simulation of a solidifying phase change (Poirier and Salcudean, 1988). 74

7.5 Seven different grid sizes have been evaluated. The time step is for each grid evaluated by the stability criterion in equation 7.23. 77
7.6 Computation time for four different variations of the model is presented. As computation time is also depended on the computer on which the model is run, index numbers are used for showing differences in calculation time. 80

8.1 Non-dimensional figures for evaluation of natural convection of 1 meter heat pipe at 275°C and PCM at 221°C. Simulation is in charge mode 1. 88
8.2 Non-dimensional figures for evaluation of natural convection of 1 meter heat pipe at 226°C and PCM at 221°C. Simulation is in charge mode 2. 88

9.1 Thermophysical properties used for fin efficiency calculations. The properties are evaluated for the mean liquid temperature of discharge mode 1; 236 °C. 95
9.2 Specific circular fin design preliminary chosen on the basis of efficiency. . 99
9.3 Sunrod tube design chosen on the basis of efficiency. 99
9.4 Estimated prices on fin material on a volume basis. Extracted from Laing et al. (2009) 100
9.5 Final fin designs selected for further CFD based studies. 101
9.6 Outer heat transfer coefficient h_a of selected circular fin designs. 101

10.1 Grid size details and characteristic numbers for the grid qualities of the three grids considered for the 2D smooth pipe grid. 104
10.2 Physical dimensions of the computational domain of the 2D circular fin grid. Characteristic names refer to figure 10.7a. 109
10.3 Grid size details and characteristic numbers for the grid qualities of the three grids considered for the 2D circular fin grid. 110

11.1 Grid size details of the five grids considered for this grid independency study. 120
11.2 Characteristic numbers of the grid quality. 120
11.3 Final grid dimensions for evaluating the 3D model. 121
11.4 Characteristic numbers of the final grid quality. 121

12.1 Four new models are created with different dimensions. All dimensions mentioned are in mm. 128

A.1 Details of the DSG operated PTC solar field at Plataforma Solar de Almeria, Spain, in connection with the DISS project. Extract from Zarza et al. (2004). 144

D.1 Hardware details of the student node of the cluster used for all quasi-1D CFD simulations. 152

Nomenclature

a	m^2	Area
c_p	$kJ/kg \cdot K$	Specific heat
g	m/s^2	Gravitational acceleration
h	kJ/kg	Specific enthalpy
h	kJ/kg	Sensible enthalpy
h	$-$	Hour
k	W/mK	Thermal conductivity
l	m	Length
$mass\%$	$-$	Mass fraction
$\dot{m}$	kg/s	Mass flow rate
r	m	Radius
t	s	Time
t	m	Thickness
$\dot{q}$	Q/m^2	Heat flux
A	m^2	Area
C	$-$	Fluid-Surface Coefficient
C	$^\circ$	Celcius
C	kJ/K	Capitance
Gr	$-$	Grasshof number
H	kJ	Enthalpy
J	$Joule$	Energy
K	$Kelvin$	Kelvin
L	m	Length
Nu	$-$	Nusselt number
P	bar	Pressure (absolute)
Pr	$-$	Prandtl number
R	K/W	Thermal resistance
Ra	$-$	Rayleigh number
Re	$-$	Reynolds number
T	$^\circ C$	Temperature
T	$10^3 kg$	Ton
U	W/m^2K	Overall heat transfer coefficient
V	m/s	Velocity
W	J/s	Watt
$\sim$		Approximately
α	m^2/s	Thermal diffusivity
β		Volume expansion coefficient
η	$-$	Efficiency

ν	m^2/s	Kinematic viscosity
μ	$Pa \cdot s$	Dynamic viscosity
ϕ		Radians
ρ	kg/m^3	Density
σ	N/m	Surface tension
θ	$^\circ$	Degree
$*$		Non-dimensional

Subscripts

Ar	Aspect ratio
av	Average
c	Characteristic
cr	Cross-sectional
e	Electric
EAS	Angular skewness
f	Phase changing
fg	Latent heat of vaporization
i	Time step
liq	Liquidus
lm	Logarithmic mean
m	Mean
p	Pipe
p	Pitch
s	Surface
SC	Size change
sf	Surface-fluid
sat	Saturation
sl	Latent heat of fusion (solid-liquid)
sol	Solidus
th	Thermal
tot	Total
v	Vapour
L	Liquid
S	Solid
PC	Phase change
∞	Far from the surface

Abbreviations

CSP	Concentrated Solar Power
CFD	Computational Fluid Dynamics
DTA	Differential Thermal Analysis
DSC	Differential Scanning Calorimetry
DSG	Direct Steam Generation
ENG	Expanded Natural Graphite
GEG	Ground Expanded Graphite Powder
HS	Heating Surface
HTF	Heat Transfer Fluid
NGF	Natural Graphite Flakes
PCM	Phase Change Material
PSA	Plataforma Solar de Almeria
TES	Thermal Energy Storage
USD	United States of America, Dollars
eqn	Equation

Part I

Introduction

Chapter

1

Introduction

1.1 Heat Storage in Solar Power Applications

Concentrated Solar Power (CSP) is the common denominator for four different technologies: Parabolic trough, Fresnel, Central receiver and Dish Sterling. An example of a parabolic trough collector (PTC) is presented in figure 1.1. Both PTC and Fresnel use reflectors to heat a heat transfer fluid (HTF), which is circulated in the absorber pipe placed in the focal point of the reflector mirrors. In these systems, the HTF is usually a thermal oil. The HTF then runs to a heat exchanger where pressurized water is evaporated and superheated. The central receiver technology uses heliostats to reflect the sunlight onto a receiver mounted on a tower. The HTF in these systems is typically water, which, under pressure, runs through the central receiver and is evaporated.

Figure 1.1: *EuroTrough parabolic trough collector prototype. Taken from Price et al. (2002)*

Beyond the point in the system, where water is evaporated, and in some cases superheated, the three systems are not very different from each other. The steam now runs through a steam turbine producing electricity. The low grade steam is then condensed in a condenser before it is pressurised and heated once again in a repeating cycle. Dish Sterling, on the other hand, is different from these systems. A large parabolic receiver focuses sunlight on a Sterling engine which runs a small generator. This means that each receiver is a small power plant in itself, but also

that heat storage is not an option.
Regardless of the technology, the steam production undergoes large variations during the day, as the production follows movement of the sun across the sky. The production is illustrated in figure 1.2, where it is shown that production is only possible within a given time frame during the day.
This time frame varies with the latitude of placement of the CSP plant. The further away from the equator, the more seasonal variations are experienced. As a rule of thumb a CSP plant should only be build within +/- 40 ° latitude. This is also known as the solar belt, which is shown in figure 1.3.

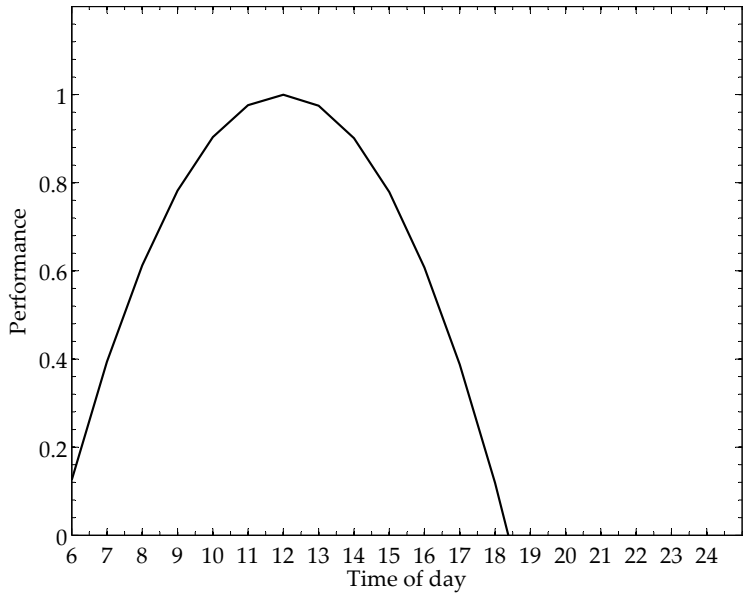

Figure 1.2: *Power productionof a CSP plant during a day. To illustrate an example, a midsummer day in Aalborg Denmark is shown. The data are obtained from a program developed by Mr. Palle Wendelboe (Aalborg CSP).*

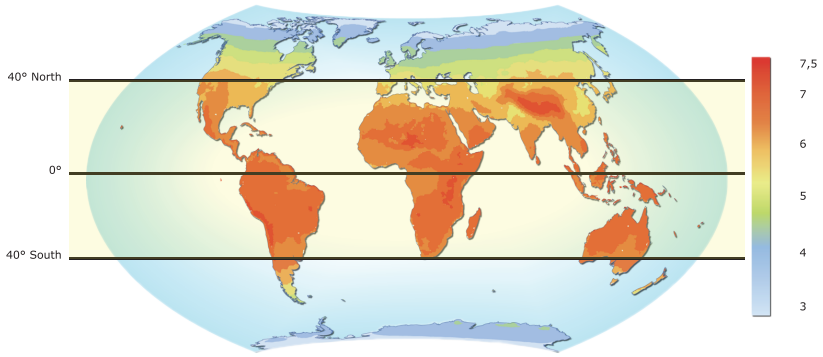

Figure 1.3: *Illustration of feasible locations for CSP plants. The figure is based on average annual ground solar energy (1983-2005) - Clear sky insolation incident horizontal surface [kWh/m^2/day].*

Prediction of daily output of a CSP plant is straight forward. As long as the plant is

running without any technical difficulties, the output can be estimated according to location, time of year, and weather conditions. As the plant is dependent on sunlight, power production can only take place during daytime. When comparing figure 1.4a and 1.4b it is clearly seen that the price follows the electricity demand. Furthermore, as observed from figure 1.4a, daytime hours are connected to the highest electricity prices and thereby also the largest profit. This is very different from wind power, where the wind is the governing factor for power production. Of course this can be both night and day. Electric power is, however, consumed 24 hours a day, which is the predominant problem for most renewable sources of energy; consumption and production does not always coinside.
The variation between production and consumption is a major factor for expanding a CSP plant with a heat storage facility, as this gives the plant the ability to produce electricity independently of the power source. The storage facility can be used for producing electricity when the price is high and storing heat when prices are low. As figure 1.4a shows, there is a large variation in prices during a 24 hour period.

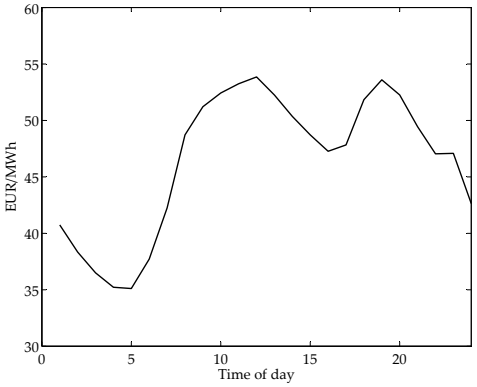

(a) *Electricity prices varies during the day according to demand and production. The curve shows average price for Denmark in 2010.*

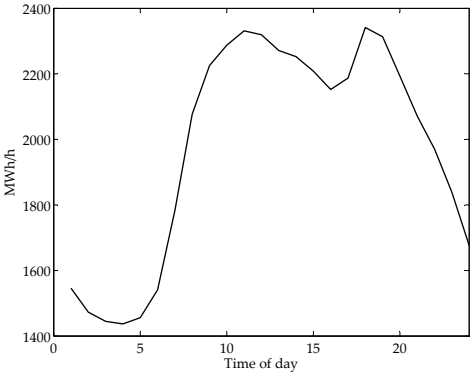

(b) *Daily average electricity production in Denmark 2010.*

Figure 1.4: *Example of daily electricity price and production fluctuations for the Danish electricity grid in 2010. Note the Y-axis starting point (Energinet.dk, 2011).*

When expanding a CSP plant with heat storage, the production pattern completely changes. Figure 1.5 shows an example of the power production output, when a heat storage is included in the system.Here the peak of the normal production without storage is eliminated, and the heat is used for charging the heat storage. As the production declines in the afternoon, the heat storage discharges and the power production can continue for a longer period of time.
Regarding design criteria for a steam cycle, the mass flow rate is governing quantity. The mass flow is a determining factor for a lot of components such as pipes, steam turbine, condenser, pumps etc. Moreover, the price for all these components increase with the mass flow. As it is shown in figure 1.2 and 1.5, production without storage gives a large variation in production, which also means that mass flow varies. This means that all components most of the time are not fully utilised according to their

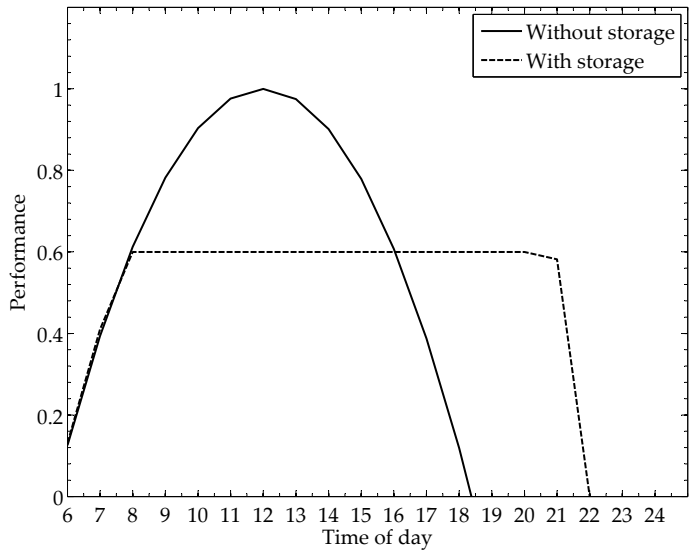

Figure 1.5: *When heat storage is used in a CSP plant, power production is evened out.*

capability.

When using heat storage, the steam cycle can be designed for at specific mass flow, which is then the maximum load condition. This way, it is possible to fully utilise the components of the steam cycle according to their capability. As an example, this can be shown with the isentropic efficiency curve for a steam turbine, which is presented in figure 1.6. From this, it is clear that the steam turbine has a point of maximum efficiency. With heat storage the production can be matched to this mass flow, which makes the steam turbine as efficient as possible.

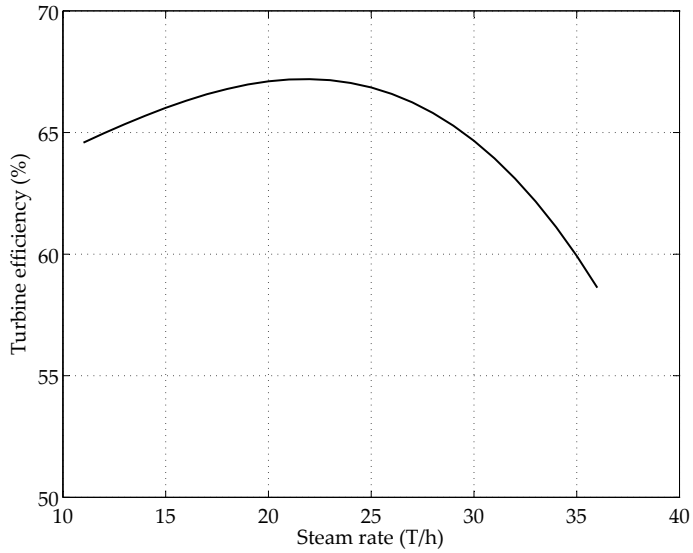

Figure 1.6: *Example of isentropic efficiency curve for a steam turbine as a function of mass flow rate in T/h (Bloch, 1995).*

1.2 State-of-the-Art

This section provides an overview of the latest progress and trends in the field of latent heat storage within solar power. In addition, a review of the improvements within concentrating solar collectors is placed in appendix A.
The most prominent players on the scene are research institutes from Germany, Spain, and the US, where Spain have been the preferred host for the carrying out of important experiments with both solar collectors and storage prototypes. Some of the research institutions showing special interest and commitment within this area are: *Deutsches Zentrum für Luft- und Raumfahrt* (DLR); National Renewable Energy Laboratory (NREL); Sandia National Laboratories Albuquerque; and *Centro de Investigaciones Energéticas, Medioambientales y Tecnológicas* (CIEMAT). From figure A.4b in appendix A, it is seen that the US and Spain currently are far ahead all other nations in terms of MW_e installed CSP capacity.

1.2.1 Latent Heat Storage for Solar Energy

The most significant project regarding thermal energy storage from direct steam solar power plants on European grounds is arguably the DISTOR collaboration. Where the molten salt-based technology of thermal energy storage has been used for years, there was only limited knowledge regarding the potential for PCM-based latent energy storage in combination with a DSG solar power plant. The aim of the project is to develop latent heat storage operating within the temperature range 220-330 °C which corresponds to DSG steam pressures of 30-100 bar (DLR, 2008). Mainly due to their low cost, nitrate salts have been the preferred PCM used in the study, but these materials are associated with poor thermal conductivity. For a latent heat storage to be economically feasible, new storage designs compensating for the problem of thermal conductivity were investigated. To compare different concepts as they progressed, the DISTOR project decided on a research strategy running on three parallel tracks. Of all the possible ways to solve the problem, the following three concepts were selected for further investigation in the project (Steinmann and Tamme, 2008):

- Extended heat transfer area
  - Finned surfaces
  - Capsules
- Composite material with increased thermal conductivity
  - Infiltration
  - Compounding
- Intermediate heat transfer medium (liquid/gaseous)

Furthermore, the project included testing of concepts both in laboratory experiments in the 5-10 kW_{th} scale and on-site testing by connecting prototypes with a capacity of 100 kW_{th} to the DISS facility in Almeria, Spain. Experiments were all carried out

with an eutectic KNO_3-$NaNO_3$ mixture (also denoted *draw salt* in the literature). The following is a presentation of the status of the project which has been documented so far. Up to this point, laboratory experiments have been completed for finned surfaces and capsules, but both laboratory and industrial scale tests of composite compounds and cold compressed composites have been carried out (Steinmann and Tamme, 2008) (Pincemin et al., 2008).

Extended Heat Transfer Area

Two different concepts are pursued in order to increase the heat transfer surface: finned tube/sandwich design and encapsulation. An important conclusion from the finned tube concept study was that expanded graphite by far proved to be the most cost-effective fin material. This is due to a thermal conductivity of about three times that of steel ($\sim 50\ ^{W}/_{m \cdot K}$) and a lower price on the volume specific basis. Moreover, graphite has a good resistivity against corrosion when exposed to nitrate salts. The more specific results from the DISTOR project regarding the use of fins are reserved for section 9.1.
Expanded graphite fins and PCM arranged in a sandwich construction have been studied under real working conditions in the work by Bayón et al. (2010), where a 100 kW_{th} latent heat storage prototype was connected to the DSG-based DISS facility in Almeria, Spain. The PCM used here was an eutectic KNO_3-$NaNO_3$ composition. One of the main results of these experiments was that the storage unit showed a significantly lower thermal power output than expected from the design. This was due to operating conditions being different from the design conditions, and due to poor design of the prototype. Large thermal losses occurred through the top of the prototype because of insufficient insulation. Moreover, almost half of the total PCM mass did not experience any phase change due to a combination of poor conductivity of the PCM and poor design of the heating surface (Bayón et al., 2010).
Another way to reduce the distance across which heat is transported into the PCM is by encapsulating it with a highly conductive material. However, the volumetric change the of PCM during phase change induces a problem of varying pressure inside the capsules, which caused two different capsule designs to be studied: A stiff wall capsule containing the PCM and a gas; and a capsule made of a flexible material exclusively containing the PCM. As for the flexible capsules, there are no inexpensive materials with satisfactory durability in terms of corrosion for operating temperatures >200 °C. Steel could be used, but this required wall thicknesses >1 mm to withstand corrosion, which proved not be to a cost-effective design if the distance for heat transport were to be reduced significantly. The stiff-walled capsules showed a different potential. Due to manufacturing concerns, a cylindrical design were chosen for the capsules, which were filled a prescribed level with PCM and subsequently the two halves were welded together. Afterwards the sealed capsules are arranged in parallel and in placed inside a vessel. Laboratory experiments were carried out with capsules of 0.4 m in length and diameters of 0.15-0.25 m as shown in figure 1.7a. The initial size of the gas volume were found to have great influence on the capsule pressure as a consequence of varying temperature. If figure 1.7b is considered, the problem is clearly seen at temperatures above the eutectic KNO_3-$NaNO_3$ phase

change temperature if the initial gas volume is reduced below 20 %. Consequently, in order to avoid long-term load issues because of the cyclic nature of the storage charge/discharge operation, the PCM volume should not exceed 80 % of the total capsule volume (Steinmann and Tamme, 2008).

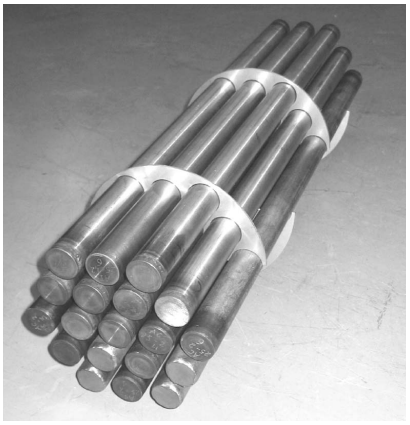

(a) *Sealed stiff-walled capsules filled with PCM and some minor fraction of gas. This prototype was used for laboratory scale tests.*

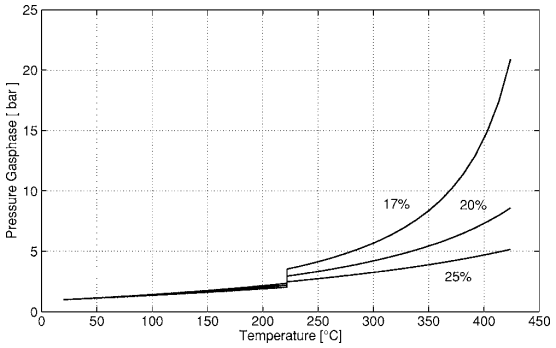

(b) *Effect of initial gas volume on the internal pressure of a capsule due to temperature changes.*

Figure 1.7: *Stiff-walled capsules filled with KNO_3-$NaNO_3$ and gas ready for testing, and a plot of the effect of initial gas volume in the capsules. Taken from Steinmann and Tamme (2008).*

Composite Materials

Pincemin et al. (2008) studied the effects of different manufacturing methods and forms of the graphite material used for composite materials with increased thermal conductivity in the DISTOR project. Graphite in the form of natural graphite flakes (NGF), expanded natural graphite (ENG), and ground expanded graphite powder (GEG) were considered in the investigation. Other than compounding and infiltration, Pincemin et al. (2008) also studied a cold compression manufacturing technique. The PCM used here was an eutectic KNO_3-$NaNO_3$ mixture.
Compounding involves heating the PCM above its melting temperature before mixing with graphite. The temperature is raised to a level where the PCM viscosity and density are particularly suitable for a homogeneous mixing of the two species. This method was pursued further with NGF and GEG while experiments with ENG was discontinued because of poor mixing capability with molten salt due to its low density. The compounding method resulted in a highly homogenous product with isotropic properties and increased thermal conductivity. Furthermore, compounded composites showed a stable behaviour during thermal cycling of the material (Pincemin et al., 2008).

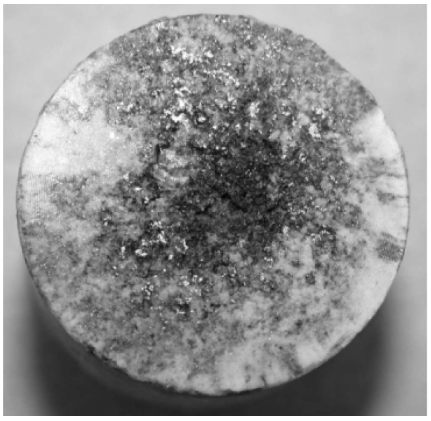

(a) *Graphite matrix infiltrated with PCM. The problem of radial heterogenous distribution of material is clearly seen*

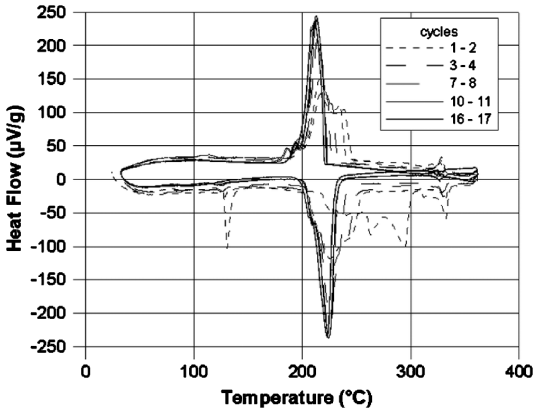

(b) *Cyclic behaviour of cold compressed compound (KNO_3-$NaNO_3$ eutectic mix with 20 mass % graphite).*

Figure 1.8: *Graphite matrix infiltrated with PCM and cyclic behaviour of a cold compressed compound. Taken from Pincemin et al. (2008).*

(a) *Composite material heat storage unit of PCM and graphite powder. The materials are compressed to form a composite matrix.*

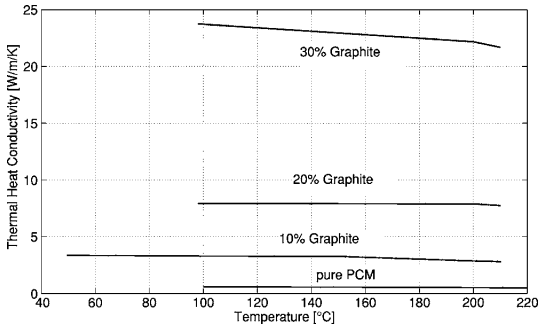

(b) *Effect of graphite powder content on the thermal conductivity of the composite material.*

Figure 1.9: *Composite material heat storage unit and proved effect of graphite content in the composite. Quantities are presented as mass fraction. Taken from Steinmann and Tamme (2008).*

The infiltration approach, where a porous ENG matrix is filled with molten PCM, showed great difficulties regarding complete infiltration of the two components. In spite of testing an ENG matrix at atmospheric pressure, at subatmospheric pressure, at different temperatures, and with different matrix porosities, this proved not to be a useful manufacturing technique. Figure 1.8a shows one of the problems encountered, namely strong radial heterogeneous distribution of the species (Pincemin et al., 2008). Finally, the method of cold compressing should be mentioned. Cold compression is classified here as a form of compounding technique as the species are mixed together rather than one of them infiltrating the other. It involves compression of premixed

PCM and ENG or GEG in powder form in a mold. The shape of the product is solely adopted from shape of the mold and can easily be machined afterwards *e.g.* by drilling holes for steam pipes as presented in figure 1.9a. The great advantage of this process lies in its simplicity, as it is carried out at room temperature, which removes the significant energy needs required to melt the PCM and reduces corrosion of the equipment. In terms of thermal cycling, the cold compressed compound showed a steady behaviour after five cycles, which is showed in figure 1.8b. Experiments showed that this approach could raise the effective thermal conductivity significantly, which figure 1.9b clearly shows. However, because of rearrangement of the graphite layers during the compression process, the material holds anisotropic properties as the thermal conductivity is larger in the radial direction than the axial direction of compression. Furthermore, an optimum graphite content exists due to expanded graphite having a cost roughly twenty times that of PCM on a mass specific basis and because increasing graphite content means decreasing PCM content and thus storage capacity[1] (Steinmann and Tamme, 2008) (Pincemin et al., 2008).
In general, the composites does not experience any weight loss at temperature up to 350 °C, but some tendency of salt leakage due to impurities and remaining mechanical stresses was encountered during thermal cycling, which will be studied further in the ongoing research of the DISTOR project (Pincemin et al., 2008).

1.2.2 Future Projects

The CSP technology is certainly expected to assume a prominent role in future electricity production. In Europe, the focus is largely headed towards developing future CSP plants around the Mediterranean, in Northern Africa, and the Middle East. The potential of the technology has been analysed for instance in reports by DLR: MED-CSP, AQUA-CSP and TRANS-CSP. The MED-CSP study from 2005 analysed the potential for CSP in the countries around the Mediterranean and the Arabian Peninsula. Figure 1.10 illustrates the electricity generation for all these countries as predicted by demand models and expected introduction of renewable energy sources. The magnitude of the CSP section is mostly due to expected storage options of this technology combined with the high energy intensity of the insolation of this region DLR (2005). AQUA-CSP of 2007 explored how the predicted growth in freshwater needs could be met by desalinating seawater via CSP plants DLR (2007). Finally, TRANS-CSP of 2006 studied the potential for renewable electricity production in Europe and how Europe could benefit from importing power from Northern African CSP plants (DLR, 2006).

Probably the most prominent future large scale CSP project is the DESERTEC project, which to some extend builds on knowledge from the MED-CSP, AQUA-CSP and TRANS-CSP reports. It involves electricity production via CSP plants for European, North African, and Middle Eastern countries by installing numerous CSP plants in North Africa. Trans-Mediterranean cables will transfer CSP-produced electricity to the European customers. Calculations by DLR showed that as much as

[1] For instance, the effective latent heat of fusion is reduced from 100 $^{kJ}/_{kg}$ of pure PCM to 70 $^{kJ}/_{kg}$ with 20 mass % graphite. The phase change temperature of PCM was unaffected by the presence of graphite (Pincemin et al., 2008).

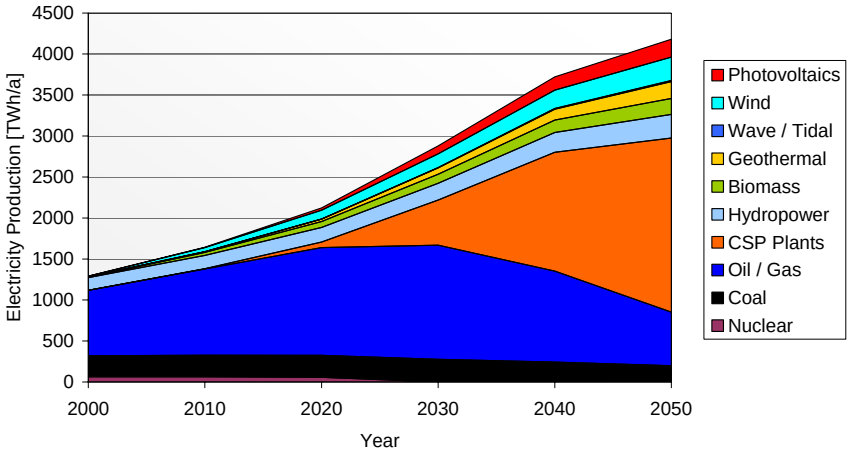

Figure 1.10: *Annual electricity production in countries surrounding the Mediterranean and countries of the Arabian Peninsula considered in the scenario of the MED-CSP study. From DLR (2005).*

15 % of the European electricity needs by 2050 could be provided by CSP plants. In 2009, twelve participants within the technological and financial aspects of the project agreed on launching a three year period of detailed planning of the project (DLR, 2009).

Countries which hold a membership of the EU could have a special interest in the DESERTEC project, as they, by a directive from 2009, are subjected to meet a given level of renewable energy by 2020. However, the requirements of the directive are based on power consumption, which allows member countries to fulfill their obligation through importing renewable energy (Baker et al., 2010). Though it is questionable how large a power import can be achieved from North Africa and the Middle East already by 2020[2], the directive might serve as a basis for future agreements regarding implementation of renewable energy sources in the EU. Moreover, Baker et al. (2010) points out that North African countries does not have the same motivation for replacing fossil-based energy production with renewable sources of energy. However, North Africa and the Middle East must deal with future predictions of insufficient freshwater resources, which makes CSP desalinating plants an attractive option. In conclusion, for all who has an interest in CSP technology or low CO_2 emission electricity production in general, the future development of the DESERTEC project will be extremely exciting to watch. The last sentence should also be considered in the light of the political instability that has swept across the North African and Middle Eastern region from the early start of 2011 and up to the submission date of this report.

A final comment on the planned DESERTEC project, is that the authors of this report do not question the correctness of the DLR reports in any way, but one should keep in mind that as one of the world leading centres of knowledge and experience within this particular field of engineering, DLR does have an interest in a flourishing CSP industry as the need for their services most likely will increase significantly.

If CSP plants currently under construction worldwide are considered, then Spain

[2] In terms of CSP produced power.

was clearly in the lead by 2010. This is due to the installation of 1540 MW_e distributed on 33 new CSP plants where all but one use the parabolic trough design. The follower on this list is the US with 75 MW_e under construction reported in 2010. However, in terms of planned CSP projects, the US is by far the largest user of CSP technology with a striking total capacity of 10442.8 MW_e. Here, the nation with the second largest planned CSP capacity is Australia with 817 MW_e. The total planned CSP capacity sums up to 14 GW_e (Baker et al., 2010).

Chapter

2

Project Background

The investigation has its origin as an idea for product development from the engineering company Aalborg CSP. The company's main area of business is steam generators for concentrated solar power plants, and at the moment many of their customers are placed in the Mediterranean region of Europe. For some time, Aalborg CSP have wished to include a simple storage facility in their product range, which provided the motivation for doing this study of PCM-based heat storage.

2.1 Heat Storage Configurations for CSP

As already explained, heat storage in CSP applications have an advantage with respect to dispatchability in power production, *i.e* ability to produce power when needed. Most CSP plants with heat storage are using either steam accumulators or two-tank molten salt. Developers are currently working on phase changing heat storage along with other technologies. Table 2.1 shows som of the thermal energy storage (TES) technologies used at present, along with examples of near-future technologies. Other storage technologies are also being developed but these technologies are not to be implemented in the near future (Skumanich, 2010).

	TES type
Present technology	Steam accumulator
	Two-tank molten salt
Near future technology	Phase change
	Improved molten salt
	Nanoscale molten salt
	Solid materials storage

Table 2.1: *Technologies used at present time and technologies emerging.*

2.1.1 Steam Accumulators

Fossil fuel fired plants have been using steam accumulators for decades. This makes it a very well known technology. When water is used as HTF, intermediate HTF and a separate heat exchanger is not necessary. Due to this, steam accumulators are a very simple technology.

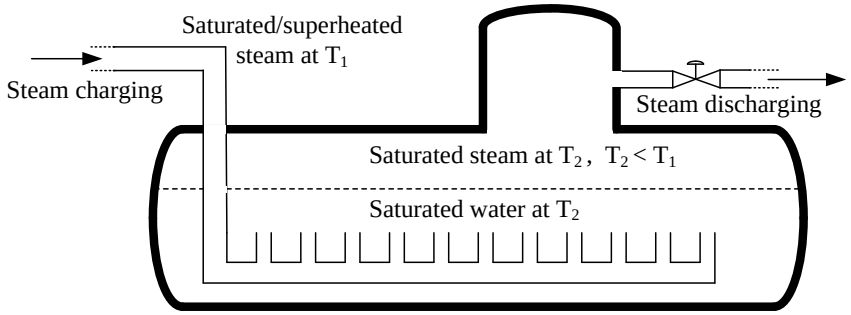

Figure 2.1: *Illustration of steam accumulator.*

The steam accumulator is functioning by heating water to saturation temperature by the HTF (typically water/steam). Further increase in heating increases both pressure and temperature. This can continue until storage pressure reaches HTF pressure. Until then, steam fed into the steam accumulator heats the water and condenses at saturation temperature.
When the system is discharged, steam is let out of the steam accumulator. When there is no compensation for mass lost, pressure is reduced inside the tank. This causes some of the water to evaporate. This process continues until storage steam is no longer needed, or until pressure and temperature has dropped to a level where it is no longer usable. Disadvantages by the system is its low capacity and the fact that the accumulator must be pressurised.
One of the benefits of a steam accumulator, besides being a well known and simple technology, is that it has a very fast reaction time, which makes it suitable for CSP systems, as it can easily and fast supply steam when a single cloud covers the solar panels. This is, of course, only as long as the accumulator is charged. A steam accumulator cannot supply superheated steam. If superheated steam is required, an additional type of storage must by added (Medrano et al., 2009).

2.1.2 Two tank molten salt

Two tank molten salt storage systems is a very different technology compared to steam accumulators. Two tank systems use molten salt as storage material where the salt is circulated through a heat exchanger during both charging and discharging. During this procedure the molten salt is pumped from a tank storing hot salt to a tank storing cold molten salt. Figure 2.2a illustrates the procedure during storage charging and figure 2.2b during discharge.
Temperatures of hot and cold salt is determined by the plant the storage system is inserted in to. Typically the cold salt is approximately 290°C and the hot salt can be from 390-550°C approximately. Salt used in two tank molten salt storage systems is often an eutectic mixture of KNO_3-$NaNO_3$ because this salt is cheap and has a freezing temperature well above minimum inventory temperature.
The tanks in the system are similar to commercial oil storage tanks, constructed from carbon steel with self-supporting roofs. Walls and roof are typically insulated with mineral wool batts and calcium silicate blocks.
To ensure high efficiency of the Rankine cycle the heat exchanger must be designed

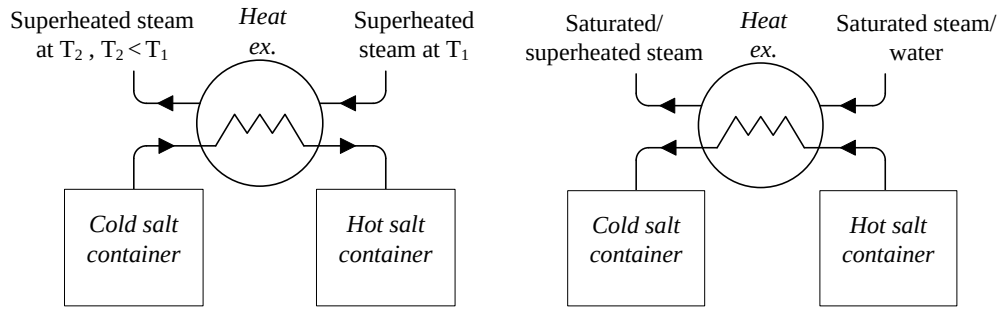

(a) *Two tank molten salt system in charge mode.*

(b) *Two tank molten salt system in discharge mode.*

Figure 2.2: *Illustration of two tank molten storage at two different states.*

with small approach temperatures in the range of 3-10 K. The heat exchanger must withstand a pressure difference from one side to the other of around 15 bar when oil is used as HTF. The pressure of the HTF can be around 20 bar, and the salt pressure is around 5 bar. If water/steam is used as HTF, the pressure difference is much larger. In either case, the best suited heat exchanger is a shell-and-tube, with the HTF on the tube side and salt on the shell side. A disadvantage to the two tank system, is the necessity to always keep a molten phase of the salt. This would require backup heater systems and a significant controller system to monitor the state of the salt (Medrano et al., 2009).

2.1.3 Phase Change

A PCM based storage is based on the latent heat in a phase changing material that undergoes phase transition from solid to liquid or liquid to solid. Within a narrow temperature interval, the storage is capable of storing large amounts of energy.

A number of different materials qualifies as a PCM among these are salt and low temperature melting metals. Metals have a high thermal conductivity in contrast to salt, but salt is typically much cheaper. Low melting temperature metals like lead is also toxic, which would increase safety measures around the storage. A way to overcome low conductivity is by adding fins to the heat pipe. The fins increase the heat transfer area, allowing more material to melt or solidify, depending on the process. (Laing et al., 2009).
Figures 2.3a and 2.3b are illustrations of the new PCM storage design concept as proposed by Aalborg CSP. As it is seen from the figure, the salt remains stantionary in the storage tank and the HTF is circulated through a heating surface possible consisting of pipes with a finned surface. When water/steam is used as HTF, the storage acts as a DSG. This saves an external heat exchanger between a HTF and water/steam.

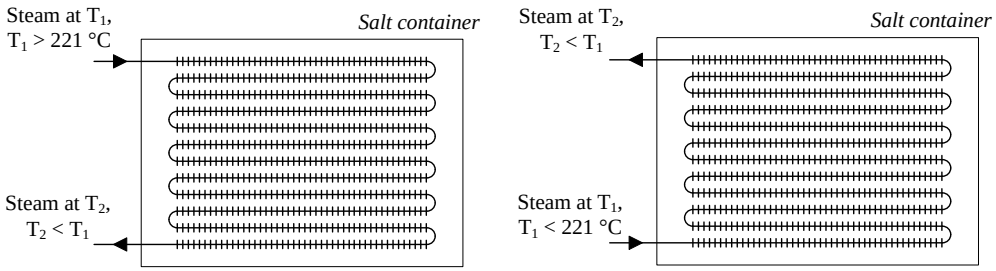

(a) *PCM storage in charge mode.* **(b)** *PCM storage in discharge mode.*

Figure 2.3: *Illustration of proposed PCM subjected to further investigation in this report. Here schematics are shown for charge and discharge stages.*

2.1.4 Capacity of Storage

As is presented in section 2.2, the storage designed for Aalborg CSP is supposed to work in temperature range 180-275 °C which is equivalent to saturation temperature of 10-60 bar. To compare the capacity of the three storage systems, they have been evaluated in these temperatures.
Comparing the capacity of the different technologies can be vary considerably, as especially two tank storage can work under much higher temperatures. Therefore two tank systems is shown with a temperature range of 180-275 °C. Energy content is calculated using specific heat (c_p)at the two given temperatures. The difference of the energy content between these values is the capacity in the storage.

	Unit	Two tank system	PCM (latent only)	PCM (latent + sensible)
C_p @ 180°C	$^{kJ}/_{kg\ K}$	1.474	-	1.474
C_p @ 275°C	$^{kJ}/_{kg\ K}$	1.490	-	1.490
Latent heat	$^{kJ}/_{kg}$	-	100	100
Stored heat	kJ	144.43	100	244.43

Table 2.2: *The energy stored in each system is calculated by the specific heat capacity at maximum and minimum temperature. If latent heat is utilised this is added to the total energy. Stored energy is based on one kg of storage material.*

As table 2.2 shows, two tank systems have larger capacity than pure PCM storage. It is, however, unlikely that the PCM storage has a homogeneous temperature profile through the storage material, which is shown in section 6.5. Some of the material will be heated to somewhere between charge temperature and PCM melting temperature, and some of the material is cooled to some point between discharge temperature and PCM melting temperature.Consequently the real storage capacity is somewhere in the range of the capacity of PCM storage for latent heat only and latent plus sensible heat. This will depend on the time used for charging and discharging. Comparing this to steam accumulators is quite difficult, as steam accumulators are a completely different technology.

With table 2.2 in mind, it becomes clear that PCM storage utilising both latent and sensible heat are very interesting due to their large storage capacity. The problem with PCM storage compared to two tank systems is that in order to make use of the latent heat, the temperature is relatively low when working with steam cycles. However, when the steam cycle is designed for this temperature range, the storage contains a larger capacity which can be utilised.

2.2 Requirement Specification

The studies carried out in this report revolves around a desirable solution specifically for Aalborg CSP. Therefore the purpose of this section is to give an overview of the requirements Aalborg CSP have in order to implement heat storage in to their CSP designs.
Aalborg CSP is covering a series of different designs with steam generating systems. Both in the way of constructed facilities, but also in future products. Aalborg CSP has already delivered steam generator systems for parabolic trough and central receiver systems in Spain. The parabolic trough solutions are based on a thermal oil as HTF, which the troughs heat up from 302°C to 395°C. The oil is then used for preheating, evaporating, superheating and reheating steam to a temperature of 390°C at 100 bar. The central receiver system produces dry saturated steam at 40 bar and a temperature of 250°C.
In the future, Aalborg CSP is focusing on small scale CSP plants, parabolic trough, and central receiver systems, which can be erected near factories in need of process steam to be used in the production. The pressure of this steam is often around 10 bar where dry saturated steam is 180°C. Pressure in these small scale CSP plants can of course be much higher, but the concept of these plants is to keep it as simple as possible. Therefore pressure is kept at a low level if possible. A small amount of work is needed to increase the pressure, but with the increased pressure a steam backpressure turbine can be driven. The output pressure is then adapted to process steam requirements. If there is no need for process steam and the requirement is purely electrical a condensing turbine can be inserted. The higher the pressure, the more work can be delivered by the turbine. Due to the requirements of the construction, pressure should not exceed 60 bar. The requirements can then be summed up to be as follows:

	minimum	**maximum**
Pressure	10	60
Temperature, saturated steam	180	275

Table 2.3: *The table presents the minimum and maximum pressure and temperatures the power plants work under. The data is to be used for specifying design of the heat storage.*

With these requirements the upper and lower limits for the PCM for the heat storage is set. The steam must have a temperature which enables solid PCM to change phase in to a liquid and the liquid PCM must have a sufficiently high temperature

to evaporate water at the specified pressure.

2.3 Initial Problem

At this point, the schematics of the initial stage of the project have been laid out in terms of motivation and an idea for a new heat surface design. The link from the latter to the following sections is expressed through the *initial problem*, which originally was formulated by Aalborg CSP and triggered the investigation carried out in this report:

How should a heat storage based on stationary PCM be constructed for it to work in a satisfactory way?

2.4 Project Outline

Covering the entire scope of the problem stated in the above question would require a quite extensive study and include thorough treatment of a number of subjects. Figure 2.4 is a graphical representation of the suggested tasks at hand in order to carry out a complete study of the given problem. The tasks are first presented in an organized manner by grouping of related subjects, and subsequently providing more elaborate descriptions in the following.

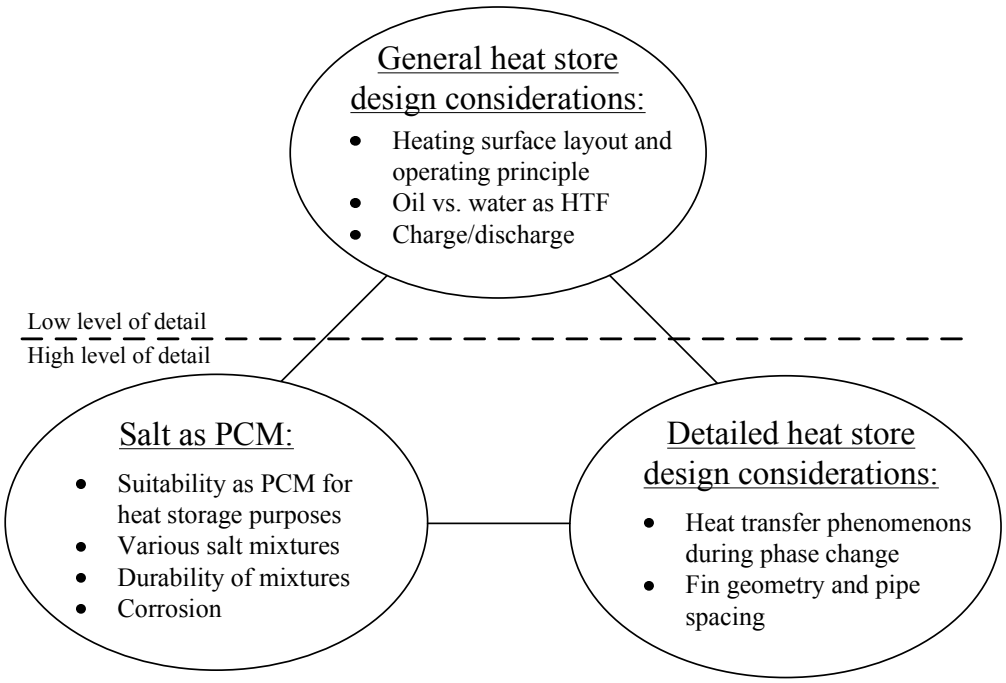

Figure 2.4: *Suggestion for main study areas of the heat storage project from Aalborg CSP.*

2.4.1 General Design Considerations

In short, this area would involve all tasks regarding the general design of the store and the heating surface (HS) within it.

Working Principle Considerations regarding whether the system could be designed to use for example natural convection to transport the HTF around.

Heating Surface A study of the optimal configuration of the HS with respect to the number and orientation of pipes.

Oil or water as HTF As a heat storage would be useful in connection with both parabolic trough, Fresnel and central receiver applications, an analysis of the consequences of using various heat transfer fluids could be relevant in this connection.

Charge/discharge The rate at which heat can be absorbed or drawn from the store is an important parameter in the design process of the solar power plant.

2.4.2 Detailed Design Considerations

Preceding studies carried out on a more detailed level might be necessary before it is possible to assess the general aspects of the heat store design. This could involve the following topics.

Phase Change Process A detailed investigation of the thermal properties of the PCM during the phase change process in order to fully understand the heat transfer phenomena occurring in this situation. For instance when the store switches from change to discharge mode, the PCM, which is now cooled by the HTF running in the pipes, will start to deposit as a solid on the HS. With continuing extraction of the stored thermal energy, the PCM will clog up the space between the fins, and consequently heat will need to be conducted through a solid layer of PCM with increasing thickness.

Optimal Geometry A look into the effects of pipe and fin interspacing and fin geometry on a detailed level. This could involve a study of which type of fin would ensure the best heat transfer, or how to make best use of the PCM while keeping the number of pipes in the HS on a minimum, which which is of great interest from an economic point of view.

2.4.3 Salt as PCM

This part of the study would include aspects regarding salts and their properties when used as a PCM.

Suitability A study of advantageous properties of various salts, possibly combined with other substances, when intended for PCM in a TES.

Mixtures An investigation focusing on the effects of altering the mixing proportions for various salts and the number species represented in the mixture.

Durability Testing for or collecting knowledge about how well a salt mixture maintains its properties after extended use. Moreover, it could be relevant to determine to what degree (if any) separation of the two salt species occurs.

Corrosion As this property of salt is a significant concern for the storage contractor, an estimate of the corrosion aggressiveness at the given operation temperatures and guidelines for possible precautions could be useful.

Chapter

3

Problem Statement

In this section the foundation of the work done in this report is presented. The *problem statement* frames the problem chosen for further exploration, which is followed by a discussion of the methods and delimitation chosen for this study.

3.1 Problem Definition

The last section in the preceding chapter described some possible subjects that would be relevant to include in the study of latent heat storage application. However, it is beyond the scope of this report to investigate them all, and therefore priorities must be made in this regard. This is done by evaluating the potential value and usefulness of the results from studying the topics in terms of contributing to answering the initial problem.
It is estimated that some of the topics concerning the more general design aspects of the heat store will ultimately require detailed understanding of the actual heat transfer and phase change processes involved. Expressed in a different way, if the detailed technical aspects are mastered, it might be easier to make reasonable propositions with respect to the general design concerns. By using this approach, some of the related subjects will inevitably be touched upon and thereby automatically be included in the study.
As described in section 1.2 a number of technologies are currently being developed for increasing heat transfer between the HTF and PCM. Focus in this report will be on understanding and evaluation of finned heating surfaces. This discussion leads to the formulation of the problem chosen for further exploration which for this report reads:

How should the heating surface in a latent heat storage be designed for most efficient utilization of a nitrate-salt based PCM?

3.2 Methods and Delimitation

The following parts of this report will pursue the general strategy of using numerical solutions methods and Computational Fluid Dynamics (CFD) simulations in order to arrive at an answer to the problem. The investigation will start off using simplified approaches to the problem, and as the work unfolds more complex ways of

formulating the problem will be introduced gradually.
It is estimated as being beyond the scope of the report to include an experimental investigation of the problem, and therefore this work will remain as a theoretical study. However, knowledge attained from experimental work carried out by other authors through prototype testing etc. is acknowledged in sections 1.2 and 9.1. The choice of heat transfer fluid affects the storage in different ways both in performance and pratical use. It is, however, chosen for this report to focus on water and steam as HTF. In section 5.4 difficulties with the CFD modelling is described. Due to these difficulties only discharge mode is modelled in 2D and 3D CFD.
First, a quasi-1D cross-sectional representation of a plain steel pipe submerged in PCM is considered. Here, the heat transfer mode of convection is neglected; and the problem is treated as a transient heat conduction problem. This is to provide some preliminary results of the charge/discharge rates of a particular PCM. Next, a 2D geometry in terms of a finned pipe is studied to reveal the effect of geometry irregularities on the melting/solidification of PCM. Hereafter follows the introduction of convection effects of the phase change process. Finally, limited number of 3D investigations are carried out on different heating surface designs with varying fin and pipe interspacing.

Part II

Quasi-1D Study

Chapter

4

Material Properties

An eutectic mixture of KNO_3-$NaNO_3$ nitrate salt is used as PCM in this work, and in this chapter it is shown why this material is well suited for the purpose. Generally, a PCM for latent heat storage applications should have as many as possible of the following desirable characteristics often encountered in the literature: *"low freezing point, high thermal stability, low corrosivity in standard materials, good heat transfer and thermal properties, and low cost"* (Price et al., 2002, 119) and *"The storage material used should be non-combustible, nontoxic, cheap and available. The lifetime must be sufficient even at higher temperatures"* (Tamme et al., 2004, 795).

4.1 Thermophysical Material Properties

In order to secure consistency and comparable results, a set of material data intended for use in computations throughout this work is established in this section.

4.1.1 Steel Properties

The steel type used for the pipes and fins of the heating surface is assumed to be St.35.8. Requirements for this are covered in the European EN10216-2 or German DIN17175-79 standards. Thermophysical properties of the heating surface steel are presented in table 4.1 and are taken from Witte (1976) and a datasheet from the Danish district heating pipe manufacturer LOGSTOR (2011). Furthermore, the chemical alloy elements of steel St.35.8 are given in table 4.2.

Property	**Symbol**	**Value, solid**	**Unit**
Density	ρ	7850	$\frac{kg}{m^3}$
Thermal conductivity	k	54	$\frac{W}{m \cdot K}$
Specific heat	c_p	0.43	$\frac{kJ}{kg \cdot K}$

Table 4.1: *Thermal properties of steel type St.35.8. Taken from Witte (1976) and LOGSTOR (2011).*

Element	Value	Unit
C	≤ 0.17	mass %
Si	≤ 0.35	mass %
Mn	≥ 0.40	mass %
P	≤ 0.05	mass %
S	≤ 0.05	mass %

Table 4.2: *Chemical composition of alloy elements in steel type St.35.8. Taken from Witte (1976).*

4.1.2 Properties of Expanded Graphite

As an alternative to metals, expanded graphite is considered as fin material mainly due to its excellent abilities as a heat conductor. This is further elaborated in section 9.1. Thermal properties are presented in table 4.3.

Property	Symbol	Value, solid	Unit
Density	ρ	1000	$\frac{kg}{m^3}$
Thermal conductivity	k	150	$\frac{W}{m \cdot K}$
Specific heat	c_p	710	$\frac{kJ}{kg \cdot K}$

Table 4.3: *Thermal properties of expanded graphite. Taken from and Bayón et al. (2010).*

4.1.3 PCM Properties

The interest for using salts in engineering applications is not a contemporary phenomenon. Some of the earliest scientific work on the subject surfaced more than 40 years ago with Bloom et al. of 1965 and A. Kofler of 1955 being some of the pioneers of determine thermophysical properties of nitrate salt compositions. However, this literature is not easily accessible possibly because of its age, but the findings are included in later work by other authors *e.g.* Omotani et al. (1982) and Tufeu et al. (1985) [1]. Figure 4.1 shows how the thermal conductivity of the KNO_3-$NaNO_3$ system varies with composition, and it illustrates well the discrepancy encountered in the early literature on this topic. While Bloom et al. reported a parabolic behavior, the work of McDonald and Davis (1970) suggested a almost linear relationship. A claim which was later supported by Omotani et al. (1982) and Tufeu et al. (1985). Inconsistencies are also obvious in regard of the phase change temperature, and a good example on this is presented in Zhang et al. (2003) where a review of the literature shows phase change temperatures ranging from 220 to 227 ° C for the same salt composition.
As some disagreement seems to exist between various data sources, an assessment

[1] Which is the reason for these particular pieces of literature not appearing in the list of references of this work.

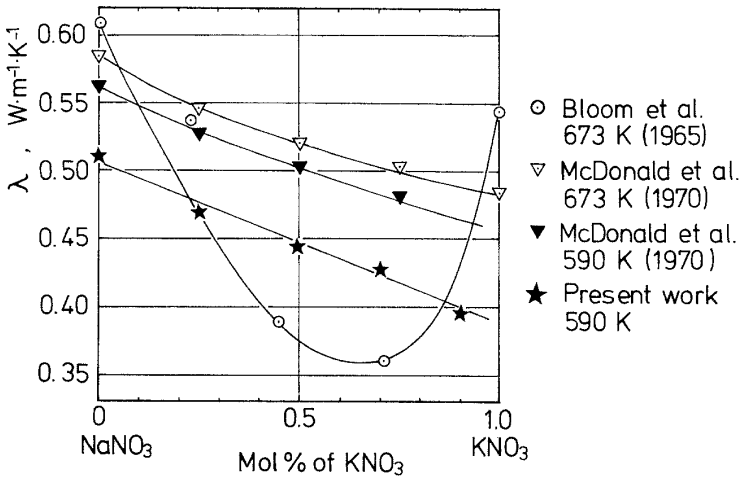

Figure 4.1: *Composition dependence of the thermal conductivity of KNO_3-$NaNO_3$ system as given in Omotani et al. (1982).*

must be made with regard to selecting the set of data that constitutes the most reliable representation of the salt mixture. However, first it must be clarified by which criteria data should be selected in order for them to be "reliable". Table 4.4 holds the data found on the salt composition through the literature review done in connection with this work. From this, we see that discrepancy is present to some extent though without being dramatic when comparing absolute values. The largest relative difference exists between smallest and the largest value of thermal conductivity, is of 34 %. The criteria for data selection is generally based on the principle that the most recent material is also the most reliable. This choice is made because of the disagreements found in the very early literature, and the belief that advances have been made through the years in terms of evaluating material properties experimentally.

4.1.4 Applied Properties of Quasi-1D Approach

In the following the data selected for use in the remaining part of this report is presented, and two different approached are used for this. For the quasi-1D approach, constant property values are used while temperature dependent property functions are applied in the 2D study. This decision is in line with the quasi-1D being a first and somewhat rough study of the nature of the problem with the 2D study being a more complex and exact formulation.
Ideally, all analysis involving a temperature range and thereby some amount of sensible heat should use formulas which describes the property variation across the given temperature interval. However, application constant values can be justified if large errors can be avoided. For instance, if the temperature interval specified in section 2.2 and the density and specific heat property functions specified for 2D in section 4.1.5 are considered, the largest differences encountered in the liquid phase are 34.4 $^{kg}/_{m^3}$ and 16.3 $^{J}/_{kgK}$, respectively. This corresponds to relative errors of 1.76 % and 1.1 %, which is acceptable for this first treatment of the problem. Assessments of varying properties in the solid phase are skipped as the temperature span from the

Property	Symbol	Reference	Value, solid	Value, liquid	Unit	Note
Density	ρ	(Mehling and Cabeza, 2008)	2050	1950	$\frac{kg}{m^3}$	
		(Bayón et al., 2010)	2040	1950		
		(Silverman and Engel, 1977)		1921		
Thermal conductivity	k	(Kamimoto et al., 1980)		0.7	$\frac{W}{m \cdot K}$	measured
		(Silverman and Engel, 1977)		0.57		
		(Bayón et al., 2010)	0.5	0.5		
		(Tufeu et al., 1985)		0.46		measured
		(Omotani et al., 1982)		0.462		measured
Specific heat	c_p	(Bayón et al., 2010)	1.42	1.5	$\frac{kJ}{kg \cdot K}$	
Latent heat of fusion	h_{sl}	(Bayón et al., 2010)	100		$\frac{kJ}{kg}$	
		(Mehling and Cabeza, 2008)	100			
Dynamic viscosity	μ	(Silverman and Engel, 1977)		$4.3 \cdot 10^{-3}$	Pa · s	@ 260 °C
Thermal diffusivity	α	(Tufeu et al., 1985)	$1.57 \cdot 10^{-7}$		$\frac{m^2}{s}$	computed
Phase change temperature	T_{pc}	(Omotani et al., 1982)	224.35		°C	measured
		(Tufeu et al., 1985)	222			
		(Mehling and Cabeza, 2008)	222			
		(Kamimoto et al., 1980)	222			
		(Bayón et al., 2010)	221			
		(Zhang et al., 2003)	221			measured
		(Silverman and Engel, 1977)	220			

Table 4.4: *Thermal properties of potassium and sodium nitrate salt mixtures found in the literature. Please note this table is compiled by the authors.*

phase change temperature to the discharge temperature of 180 °C only is ∼40 °C, hence the property changes are assumed to be neglectable when considering a solid medium.

For an overview of the quasi-1D properties, selected data is presented in table 4.5. Thermophysical properties of the heating surface steel are taken to be those presented above in table 4.1. In line with the decision of generally using data from contemporary literature, the phase change temperature is chosen to be that reported by Zhang et al. (2003) where a differential scanning calorimetry (DSC) method was used in their experimental study of phase equilibria of the KNO_3-$NaNO_3$ system. The DSC method does produce more accurate results according to Mehling and Cabeza (2008). Earlier investigations such as McDonald and Davis (1970), Tufeu et al. (1985), Kamimoto et al. (1980), and Omotani et al. (1982) used more pragmatic approaches in the experimental setup. The values for thermal conductivity are needed both for the liquid and solid phase of the salt mixture. Because of this, these properties are gathered from Bayón et al. (2010) where both are present , and in order to use consistent data remaining properties are adopted from this reference. Note that Bayón et al. (2010) agrees with Zhang et al. (2003) on the phase change temperature. Thermal diffusivity and dynamic viscosity does not appear in Bayón et al. (2010) and are therefore taken from Tufeu et al. (1985) and Silverman and Engel (1977), respectively.

Property	Symbol	Reference	Value, solid	Value, liquid	Unit
Density	ρ	(Bayón et al., 2010)	2050	1950	$\frac{kg}{m^3}$
Thermal conductivity	k	(Bayón et al., 2010)	0.5	0.5	$\frac{kJ}{m \cdot K}$
Specific heat	c_p	(Bayón et al., 2010)	1.42	1.5	$\frac{kJ}{kg \cdot K}$
Latent Heat of fusion	h_{sl}	(Bayón et al., 2010)	100		$\frac{kJ}{kg}$
Dynamic viscosity	μ	(Silverman and Engel, 1977)		$4.3 \cdot 10^{-3}$	Pa · s
Thermal diffusivity	α	(Tufeu et al., 1985)	$1.57 \cdot 10^{-7}$		$\frac{m^2}{s}$
Phase change temperature	T_{pc}	(Bayón et al., 2010)	221		°C

Table 4.5: *Thermal properties of the potassium and sodium nitrate salt composition used in the analysis of the phase change process.*

4.1.5 Applied Properties of 2D Approach

Even though errors of using constant property values may be small, the 2D study is attempted to be as close to real physical conditions as possible. For example, if any effects of natural convection are to be detected in the heating surface, it is necessary to express the PCM density change due to varying temperature. Because of this, temperature dependent functions of the thermophysical salt properties are applied here.

The only temperature dependent set of thermophysical data accessible to the authors is presented in Pacheco et al. (1995) and is compiled from various sources. The majority of the data is determined for solar salt *i.e.* a 60/40 mass % $NaNO_3$-KNO_3 mixture, but some data is based on the eutectic mixture. Nonetheless, Pacheco et al. (1995) use these data themselves as being valid for solar salt and furthermore they *"have assumed the difference is not significant"* (Pacheco et al., 1995, 97) regarding the variance in salt composition. In this report, the same will be assumed meaning that these solar salt properties are applied in lack of any better data being available at the present time.

The data from Pacheco et al. (1995) is given in the temperature range of 270 to 600 °C with intervals of 10 °C, which is plotted in figures 4.2a to 4.2f. Original data are showed with a marker, while the curve fits presented in equations 4.2 to 4.7 are represented with a solid line. In this report, properties are needed from the phase change temperature to 275 °C, and for density, specific heat, thermal conductivity, and thermal diffusivity which shows a highly linear behaviour, application of the linear curve fits at these extrapolated temperature seem fair. The dynamic viscosity and Prandtl number on the other hand could induce some amount of error as their curves steepens at lower temperatures. Curve fits are done by the use of MS Excel trendline function.

$$T = [270, 280, 290, \ldots, 580, 590, 600] \qquad (^{\circ}C) \tag{4.1}$$

$$\rho = -0.636\,T + 2090 \tag{4.2}$$

$$c_p = 0.171\,T + 1443 \tag{4.3}$$

$$k = 1.90 \cdot 10^{-4}\,T + 0.442 \tag{4.4}$$

$$\mu = -1.474435 \cdot 10^{-10}\,T^3 + 2.281200 \cdot 10^{-7}\,T^2 - 1.199868 \cdot 10^{-4}\,T + 0.022708 \tag{4.5}$$

$$\alpha = 1.1353 \cdot 10^{-10}\,T + 1.4154 \cdot 10^{-7} \tag{4.6}$$

$$Pr = -4.537247 \cdot 10^{-7}\,T^3 + 7.025966 \cdot 10^{-4}\,T^2 - 0.369945\,T + 69.781238 \tag{4.7}$$

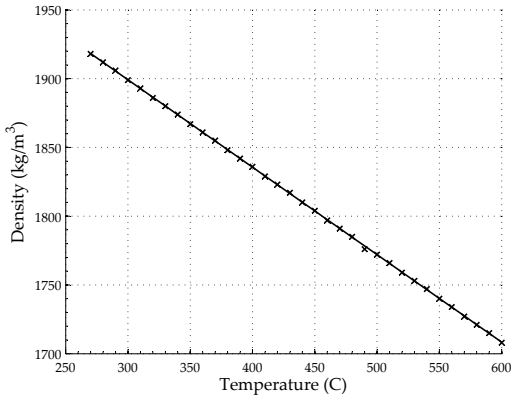

(a) *Molten salt density vs. temperature.*

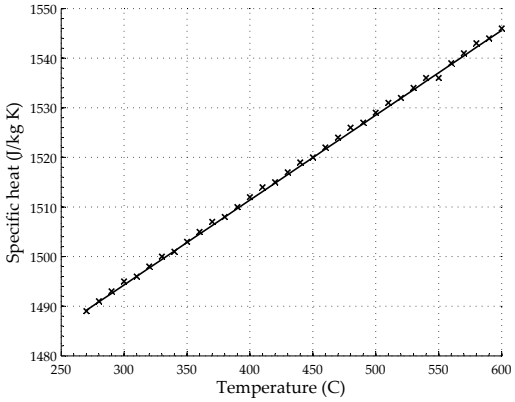

(b) *Specific heat vs. temperature.*

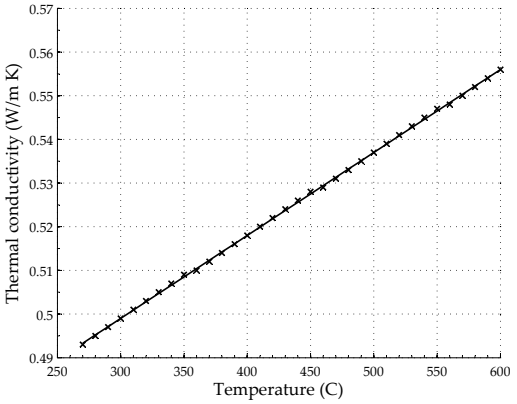

(c) *Thermal conductivity vs. temperature.*

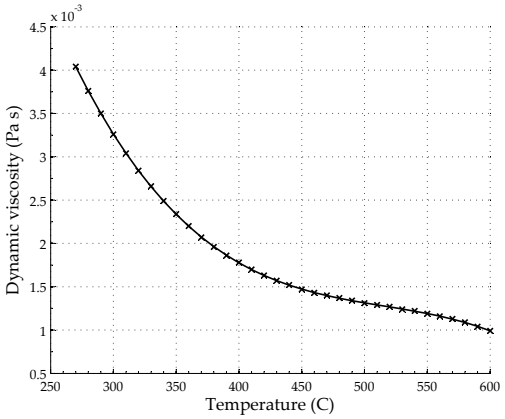

(d) *Dynamic viscosity vs. temperature.*

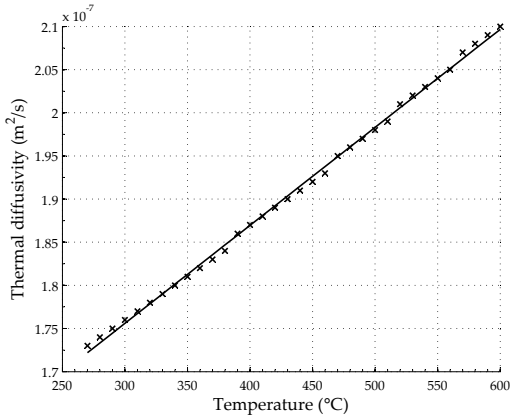

(e) *Thermal diffusivity vs. temperature.*

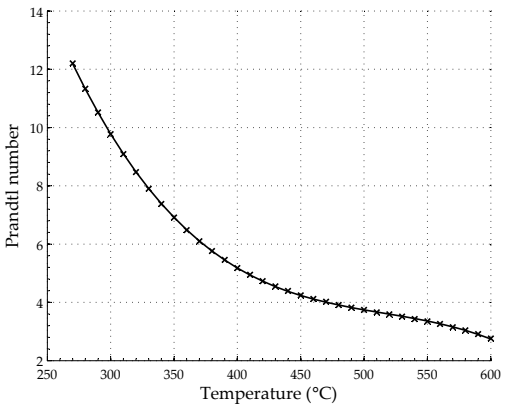

(f) *Prandtl number vs. temperature.*

Figure 4.2: *Thermophysical properties of molten salt $NaNO_3$-KNO_3 60/40 mass % in the temperature range 270 to 600 °C Pacheco et al. (1995). Original data are marked, while the curve fits in equations 4.2 to 4.5 are represented with a solid line.*

4.2 Microstructures

Insight regarding the actual behaviour of the KNO_3-$NaNO_3$ system is needed in the analysis of the solidification issue. This section is an attempt to cover this matter by addressing the changes the PCM undergoes on the microscopic level when it changes phase. Without going too much into detail in terms of the general theory of solidification and melting, this section will briefly touch upon some essential concepts regarding the solidification process of a binary system.
While the melting of the material is assumed to be fairly straightforward, there are a few different possible outcomes of the solidification process in terms of the structure of the resulting solid, which depends on the given parameters. Figure 4.3 shows a classical phase diagram of a binary system with the two species; α and β placed at each end of the horizontal axis representing their concentration in a mixture. Adopting the applied terminology from the literature, these species will be referred to as an α-phase and a β-phase. Starting from the top of figure 4.3 and moving downwards, both phases are completely liquified ("L") at high temperature. As the temperature of the melt decreases, one of the phases (for instance α) will start to solidify to a lattice structure with some amount of the opposite phase (β) present in it as well. This is still accompanied by a fraction of the melted mixture, and this two-phase zone is denoted "α+L" and "β+L". The boundary for crystallisation of one of the phases is called the liquidus and the region where this two-phase coexistence occurs is sometimes referred to as the mushy zone. The two-phase composition reduces to a single solid phase, when the temperature drops below the solidus line where the remaining liquid phase will solidify as well. This is shown in figure 4.3 with the pure solid α-phase on the left ("α") and the β-phase on the right ("β") with the in between being a solid mixture of the two. A unique situation arises at the lowest point on the liquidus line where it reaches the solidus line. At this point the solid α and β-phases are in an equilibrium *i.e.* the two solid phases and the liquid melt can coexist ("E"). This composition at this point is termed eutectic and has no mushy zone; here both phases solidify out of the liquid melt at the same temperature. The eutectic composition constitutes the concentration of α and β-phases with the lowest freezing point (Mehling and Cabeza, 2008) (Papon et al., 1999).
A phase diagram of the KNO_3-$NaNO_3$ system is provided in figure 4.4.
A solidification process starts when the temperature of the melted liquid phase is lowered to some level below the phase change temperature. The amount of subcooling required to trigger the crystallisation of the material varies with the constituents of the system, but for salts it is very low; only a few degrees at the most (Mehling and Cabeza, 2008). Due to atomic or molecular diffusion, small solid particles also called nuclei will start to form at some favourable location in the fluid *e.g.* at impurities, at cracks in the walls of the container, or as in our case; at a colder solid surface immersed in the liquid phase. As heat is removed from the system, more of the liquid phase solidify on the surface of the nuclei and they grow in size. When the early stage of crystallisation is initiated by the presence of foreign objects rather than by the PCM itself, the solidification process is referred to as a *heterogenous nucleation* (Mehling and Cabeza, 2008) (Kreith et al., 1999) (Vogel et al., 2001).

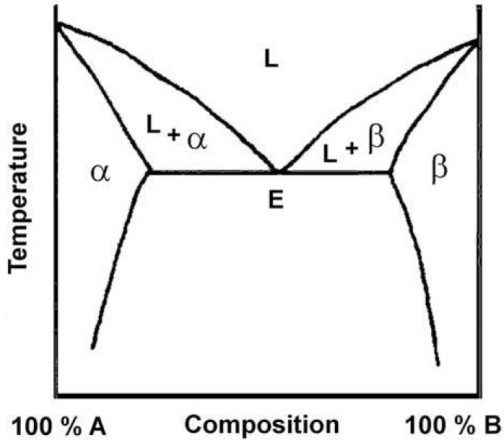

Figure 4.3: *The classical binary phase diagram. From Kerridge et al. (2009).*

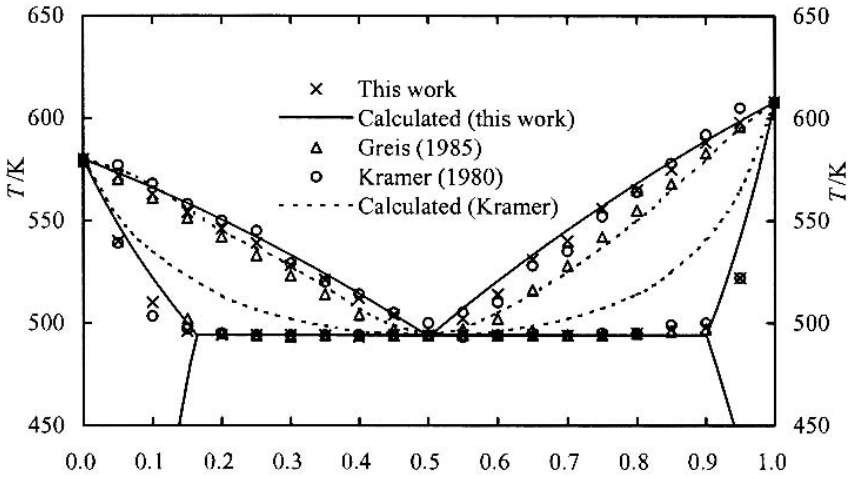

Figure 4.4: *A phase diagram of the KNO_3-$NaNO_3$ system as presented in Zhang et al. (2003).*

4.2.1 Off-Eutectic Salt Composition

During solidification of a binary mixture with an off-eutectic composition of the α and β-phases, the phenomenon called *dendrite growth* can happen, which is caused by two effects.

Consider a situation where the solidification progresses as front moving in some direction into the liquid melt. If an α-phase particle diffuses towards the solidification front and deposits on this, creating a small protrusion on the otherwise smooth face of the front. Furthermore, this causes a local deficit of α-phase in close proximity of this location. For the solidification to progress, the solid α-phase is urged to form a shape which reaches further into the liquid melt where the α-phase concentration is greater. The result is tree-like structures called *dendrites* which grow from the solid front into the melt.

Another source of dendrite growth is related to the thermal aspects of the process. During solidification of the α-phase nucleus, it will release its latent heat, which raises the local temperature. Consequently, the α-phase is encouraged to form a

structure suitable for diffusion of heat away from the solid surface, hence the growth of dendrites (Papon et al., 1999). This way, dendrite growth increases with cooling rate (Vogel et al., 2001).

4.2.2 Eutectic Salt Composition

If the ratio of the salt components of the binary system constitute an eutectic composition, and the temperature of the melt is lowered beyond the liquidus/solidus line while maintaining a steady concentration of α and β-phases, there are two possible structures the resulting solid α+β mixture can take: lamellar or conglomerate (Kerridge et al., 2009) (Berg and Kerridge, 2002). For some time, the lamellar structure was assumed to be created due to same effects know from metallic systems, namely diffusion of the phases across a limited distance. A lamellar structure is initiated by the creation of a nucleus of a given phase, which causes a higher concentration of the opposite phase in near vicinity of the nucleus. This results in nucleation of the opposite phase around the nucleus, which then again causes a higher concentration of the first phase around the recently nucleated opposite phase and so on. In this fashion, an organized structure of the phases growing side by side of each other as shown in figure 4.5. However, the molecular diffusion can only happen across some distance limited by the rate of solidification (*i.e.* the cooling rate), which means that the higher the solidification rate the thinner or finer layers of the phases will appear in the solid structure (Kerridge et al., 2009) (Vogel et al., 2001).
A conglomerate structure still offers an even distribution of the α and β-phases throughout the solid mixture, but apparently in a less organized manner. In this case, alternating α and β-phases appear in roughly spherical shaped geometries in a random arrangement.
Kerridge et al. (2009) lists a number of binary and ternary eutectic salt compositions, from which it is obvious that mixtures with high melting points tend to form a lamellar structure while low melting point compositions (including the KNO_3-$NaNO_3$ system) take on a conglomerate structure in their solid phase. However, this is believed to be a consequence of the temperature difference between the eutectic melting point and the ambient temperature in which it solidifies, more than a result of the level of the melting point itself. In connection with high melting point compositions, an ambient temperature of the solidification process much lower than the eutectic melting point is often used, which fosters a lamellar structure because ions can move across greater distances in the solid phase and hereby create more stable structures (Kerridge et al., 2009).

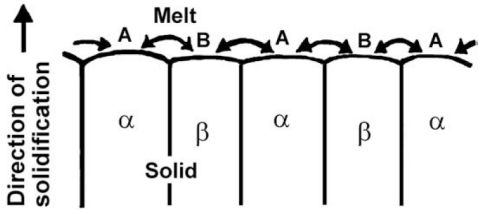

Figure 4.5: *Forming of a lamellar microstructure during nucleation due to molecular diffusion of the two phases α and β. Taken from Kerridge et al. (2009).*

From the short review above of microstructures and solidification processes, a few arguments for the choice of a suitable PCM for the thermal energy storage design can be accumulated. First, an eutectic composition has the advantage of both phases solidifying out of the liquid melt simultaneously without any mushy zone. This also prevents phase separation in the mixture, meaning sharply defined concentration differences due to density change of the solid phase, which in most cases is in decreasing direction and causing it to sink to the bottom of the container. Second, lamellar and conglomerate are both relatively evenly distributing of α and β-phases throughout a solid composition. Furthermore, as mathematical modelling of dendrite growth is very difficult (Kreith et al., 1999), refraining from considering off-eutectic compositions greatly simplify the analyse of the solidification problem.
In conclusion, a KNO_3-$NaNO_3$ eutectic mixture shows a well-defined behaviour and appear as having a fairly regular and homogenous distribution of its constituents. In the reminder of this work, the PCM is assumed to have isotropic properties.

4.3 PCM Stability

From an operational point of view, it is important to identify the limitations of the PCM when incorporated in applications. For example, as mentioned in section 1.2 thermal oil used as HTF on solar power applications has a maximum operating temperature of 375 °C above which it decomposes. In the following, a review of the stability of the eutectic PCM mixture at elevated temperatures will be given.
$NaNO_3$ and KNO_3 can decompose through several reactions, however, often these nitrate salts will be converted to their nitrite components ($NaNO_2$ and KNO_2) with a residual oxygen component. Nitrites may again be decomposed to gaseous substances such as oxide, oxygen, nitrogen, nitric oxide and nitrogen dioxide ($(Na,K)_2O$, O_2 N_2, NO, NO_2). Measurement of the rate of decomposition of nitrates may therefore be done, for example, by evaluating the weight loss, nitrate content in the composition, or formation of one of the gases just mentioned (Kramer et al., 1982).
The stability of nitrate and nitrate salts ($NaNO_3$, KNO_3, $NaNO_3$-KNO_3 (eutectic), $NaNO_2$, KNO_2) in the temperature range 77-717 °C have, for instance, been studied by Kramer et al. (1982) via a DSC apparatus. In short, the differential scanning calorimetry technique involves measurement of the heat flow to/from a test specimen as a function of temperature or time by comparing the heat flux of the test sample with that of a reference specimen exposed to the same thermal conditions. Kramer et al. (1982) found that endothermic reactions took place above the melting temperature of all compositions considered with the eutectic mix of $NaNO_3$-KNO_3 being the only exception. These endothermic reactions are indications of decomposing reactions taking place at the given temperature. In the temperature range of the experiments, Kramer et al. (1982) did not find signs of endothermic reactions above the melting temperature and thereby no indications of any decomposition whatsoever.
Temperatures of decomposition for the salts investigated by Kramer et al. (1982) and results of other authors cited in his work is presented in figure 4.6. Here, DTA refers to the experimental method of differential thermal analysis, which is somewhat

similar to that of DSC (Kramer et al., 1982).
Furthermore, solar salt ($NaNO_3$-KNO_3 60/40 mass %) used in the Solar Two project was reported stable up 600 °C. Peng et al. (2010) showed in their experiments that the ternary mixture of $NaNO_3$, KNO_3 and $NaNO_2$ (7/53/40 mass %) experienced a weight loss after 30 hours at 500 °C of 1.48 %, however, this was increased to 19.12 % at 550 °C during the same length of time. In addition, the latter authors showed highly stable behaviour of the PCM when cycled thermally from 560 to 80 °C in 14 cycles during about 7750 hours of testing. Plots of these experiments by Peng et al. (2010) can be found in appendix B.

Salt	Decomposition temperature [a]	Technique	Ref.
$NaNO_3$	840 ± 10 K	DSC	This work
$NaNO_3$	793 K	DTA	20
$NaNO_3$-Al_2O_3	1006 K	DTA [b]	18
$NaNO_3$-MgO	1029 K	DTA [b]	18
KNO_3	820 ± 20 K	DSC	This work
KNO_3	901 K	DTA	20
KNO_3-Al_2O_3	958 K	DTA [b]	18
KNO_3-MgO	1027 K	DTA [b]	18
(Na,K)NO_3	>990 K	DSC	This work
$NaNO_2$	800 ± 10 K	DSC	This work
KNO_2	800 ± 10 K	DSC	This work

[a] Temperature at which decomposition endotherm began.
[b] Salt was mixed with oxide powder.

Figure 4.6: *DSC and DTA experiments with of sodium and potassium nitrates and nitrites. Taken from Kramer et al. (1982).*

4.4 Corrosion

The latent heat storage will in reality be constructed, at least to some extent, of carbon steel (steam pipes), steel or expanded graphite (fins), and KNO_3-$NaNO_3$ nitrate salt (PCM). Corrosion issue between these elements would be a problem to the construction as such, and additional measures *e.g.* special surface coating or alternative PCMs might be needed to be considered. However, this is most likely connected to an increased total cost of the storage system, and therefore potential corrosion issues should be investigated and acknowledged.

4.4.1 Carbon Steel

Corrosion studies concerning molten nitrate salts with different levels of impurities and both stainless and carbon steel have been carried out by Goods and Bradshaw (2004). For now, only carbon steel will be considered as the steel type intended for manufacturing of the steam pipes, as mentioned in section 4.1.1, is a carbon steel. The corrosion effects of impurities such as dissolved chloride, which in some cases can promote corrosion in high temperature environments, are interesting because low grade low price nitrate salts often are connected with higher amounts of impurities.

If a latent heat storage is designed with a large capacity, inevitably this is associated with large amounts of PCM, which makes the cheaper low grade salts interesting from an economic point of view. As an additional comment to the just mentioned, Kenisarin (2010) states that the prices of *technical grade* $NaNO_3$ and KNO_3 are 0.41 and 0.62 $^{USD}/_{kg}$, which is lower than many other salts considered as PCMs. In comparison, the price on a ternary salt mixture called Hitec[2] is 1.92 $^{USD}/_{kg}$ (Kenisarin, 2010).
Experiments were carried out with 60/40 mass % $NaNO_3$-KNO_3 (often referred to as *solar salt* in the literature) compositions with varying chloride content. Carbon steel specimens of ASTM A36[3] were cut into small rectangular shapes and immersed into the molten nitrate salt held at 316 °C for several hours. The corrosion rate was evaluated through descaled weight loss measurements of the steel specimens. Results are presented in figure 4.7a and 4.7b. The numbers #1 through #7 denotes increasing chloride concentration in the salt composition starting with #1 being the lowest.

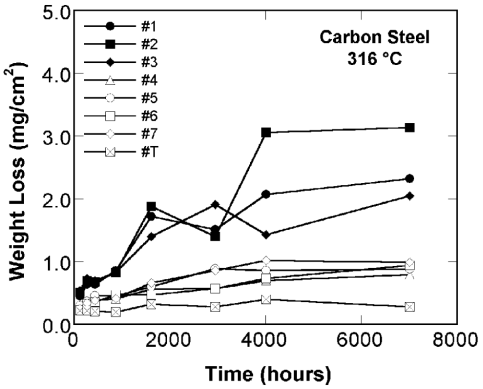

(a) *Descaled weight loss measurements for carbon steel specimens.*

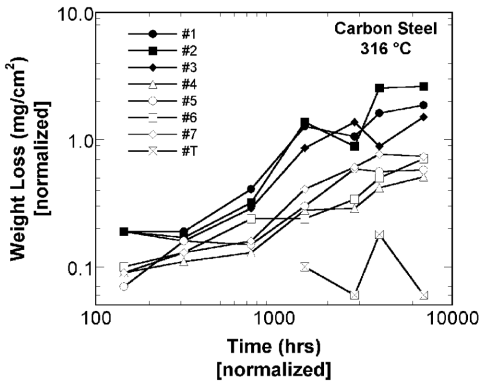

(b) *Normalised data from 4.7a presented with logarithmic axes in order to exclude short-term effects.*

Figure 4.7: *Experimental results of corrosion rates in terms of descaled carbon steel weight loss. Please note that #1 denotes a low-chloride salt composition and #7 denotes a highly impure salt composition with a high chloride concentration. Taken from Goods and Bradshaw (2004).*

Clearly, the data is somewhat scattered for the relatively pure salts #1-#3. It is concluded that at the given test temperature, high chloride content cannot explicitly be linked to increased corrosion. This is to some extent a surprising result because earlier findings in the 1980s pointed towards a clear connection between aggravated corrosion and chloride content. However, these older findings were based on temperatures ≥400 °C, which might explain this discrepancy (Goods and Bradshaw, 2004). Also, because of elevated testing temperature these older works are considered irrelevant for the application in focus in this text and will not be presented here.

[2]With the following composition: $NaNO_2$ 40; $NaNO_3$ 7; KNO_3 53 (all in mass %)

[3]With the composition: C 0.29; Mn 0.85-1.2; Si 0.15-0.3; Cu 0.2 (all in mass %). When comparing to the chemical composition of St.35.8 in table 4.2, A36 contains, apart from copper, the same alloy elements but in different concentrations.

Moreover, Goods and Bradshaw (2004) claim these results correspond to an annual corrosion rate of 1-4 μm. If corrosion is assumed to happen uniformly on the steel geometry (in contrast to pitting), the corrosion rate is considered as being fairly low. Experience from large scale operation have for instance been obtained through the Solar Two project. It is based on a central receiver system with a two-tank molten salt heat storage, which is shown in figure 4.8. The system contains $1.5 \cdot 10^6$ kg of solar salt corresponding to 114 MWh_t capacity with hot/cold tank temperatures of 565/290 °C. Solar salt was reportedly chosen as storage material/HTF due to its low corrosivity in the given temperature range compared to other materials, and the plant was successfully operated for 1.5 years with satisfactory performance of the storage system and without any significant operational issues (Herrmann and Kearney, 2002).
Furthermore, in the laboratory experiments regarding composite storage materials done by Pincemin et al. (2008), KNO_3-$NaNO_3$ nitrate salt was chosen over $ZnCl_2$-KCL chloride salt due to *"corrosion and environmental impact concerns"* (Pincemin et al., 2008, 51).

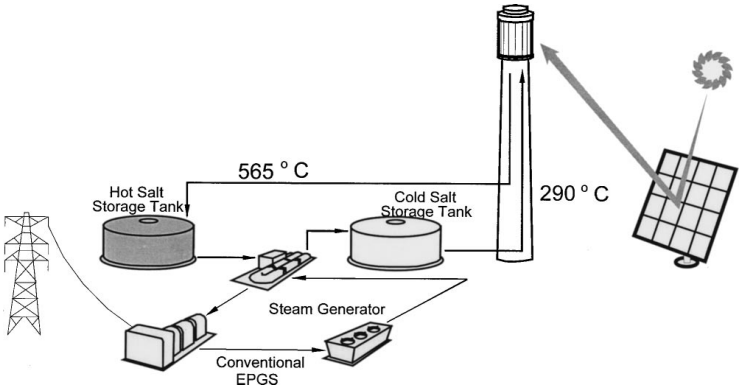

Figure 4.8: *Plant schematics of Solar Two. Taken from Herrmann and Kearney (2002).*

4.5 Summary of Material Properties

To follow up on the favourable properties of a PCM mentioned in the beginning of this chapter, a condensed overview of the findings with respect to PCM material properties is provided. An eutectic mixture of $NaNO_3$-KNO_3 has the advantage of a sharply defined solid-liquid phase transition temperature which was determined to 221 °C. However, some variation regarding data of the thermophysical properties was seen during process of determining these characteristics for the given PCM. In addition, the phase change temperature of the PCM is well suited for the applications consider by Aalborg CSP.
The eutectic property simplifies the analysis of the PCM greatly as no mushy zone occurs and hence the complex nature of dendrite growth can be disregarded. In addition, salts used as PCM generally have a very low degree of subcooling before crystallisation is initiated, and studies of the $NaNO_3$-KNO_3 microstructure when solidified gave indications of a even distribution of species within the material.

Furthermore, studies indicates that the PCM has good stability against thermal cycling without deterioration, and shows no severe sign on corrosion against carbon steel within the temperature range applied in the work done in this report. Reports from plant, which have used this type of nitrate salt as PCM and HTF, were in general positive regarding its operational behaviour. Finally, eutectic mixture $NaNO_3$-KNO_3 is a fairly cheap material compared to other PCMs.
The desired property of good thermal conductivity, however, is not shared by this particular PCM, which appears to be the largest drawback of the material.

Chapter

5

General Modelling Approach

Modelling of the heat storage is done three steps. First, the one dimensional approach serves as a simplified and rough treatment of the melting/solidfication problem, and later in Part III of this report a more detailed study, involving a two dimensional treatment, is conducted. Finally, a three dimensional treatment of the problem is carried out in Part IV. The purpose of this first study is to get an idea of:

- The transport of heat to/from the PCM in charge and discharge modes.
- The pace at which the solid/liqiud interface progresses.
- Possibilities within mathematical modelling techniques of the problem.
- The performance of the ANSYS FLUENT CFD code for this type of problem.

Two different techniques will be used: a CFD analysis and a numerical mathematical programming model. In order to remove any confusion that may arise from the fact that both techniques are indeed based on numerical mathematical methods, the following definitions are made: *CFD analysis* will from this point on refer to a CFD analysis carried out in the appropriate software program ANSYS FLUENT, and *numerical model* will refer to the numerical mathematical model programmed in MathWorks MATLAB.
The use of two different tools for modelling purposes will be compared on the basis of results produced by the two in the final section of this part of the report.

5.1 Quasi-1D Geometry

The geometry chosen represents a cross sectional view of a smooth pipe immersed in PCM as presented in figure 5.1. The term *quasi-1D* is used in connection with this approach as heat transport in one direction only (radially) is considered here. However, it is applied along multiple lines radiating from the pipe, which provides a 2D layout of a problem with a one dimensional formulation. Dimensions of the pipe are taken from a sample of a boiler heating surface and can be found in table 5.1. The PCM body extends to some circular shaped boundary greater than the outer pipe surface since heat is transported in the radial direction. Regarding the size of the body, it should extend far enough to include all temperatures in the given range and the location solid/liqiud interface at all times. The diameter of the PCM body is defined as being four times the external pipe diameter.

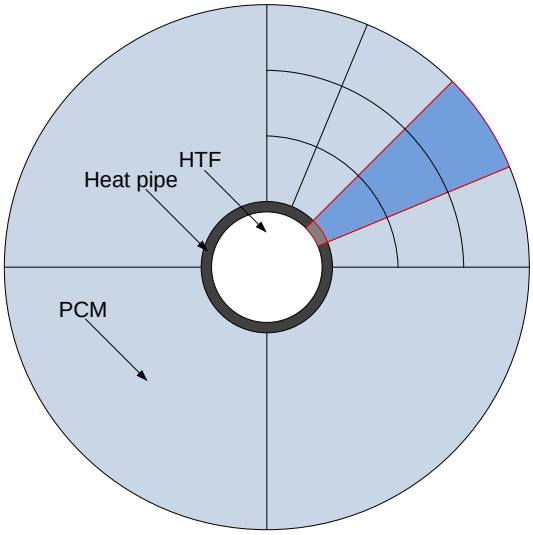

Figure 5.1: *Illustration of the quasi-1D domain. Please notice the emphasised section, which illustrates the one dimensional plane.*

Dimension	Value	Unit
Pipe diameter, inner	32	mm
Pipe diameter, outer	38	mm
PCM diameter, outer	152	mm

Table 5.1: *Dimensions of the quasi-1D modelling domain.*

In figure 5.1, the geometry is divided in to a few smaller sections. This subdivision serves only as a demonstration of the special discretisation included in both modelling approaches. In order to ensure a sufficient number of subdivisions, a grid independency study is performed for both models.

5.2 Boundary Conditions and Assumptions

The PCM is treated as being completely immobile as all natural convection effects are neglected by ignoring any gravitational forces and applying fixed values for liquid PCM density *cf.* the thermophysical property description in section 4.1.4. The inside of the pipe is assumed isothermal corresponding to vaporisation or condensation (*i.e.* very high heat transfer coefficient) of the HTF occurring depending on the mode of operation. The melting/solidfication problem is hereby reduced to a quasi-1D transient heat diffusion problem including solid-liquid phase change.
To form a basis for comparison between the quasi-1D CFD analysis and numerical model, each of them are submitted to the same boundary conditions. Two temperatures are specified, namely the HTF temperature and the PCM temperature. Initially, the PCM temperature is assumed homogeneous throughout the PCM zone. Realistically this is expected to vary according to changing modes of operation. However, a homogeneous temperature assumption is simpler to handle. As the work

expands to 2D and 3D, different PCM property conditions are used, as is already described in section 4.1.3. Boundary conditions, however, remain the same also for 2D and 3D.
Two examples of each mode of operation, charge and discharge, are selected for modelling. The PCM temperature for charge and discharge mode 1 is chosen to be 30 K below and above the PCM melting temperature. These temperatures are chosen in order to study the effect of including some amount of sensible heat additional to the latent heat of fusion. Recall that ideally the temperature range from 180 to 275 °C is available as described in section 2.2, and hence the charge and discharge 1 examples are attempts to exploit the extra storage capacity associated with the broader temperature span. Charge and discharge 2 examples on the other hand, have a larger focus on the latent heat of the storage material. Here, the temperature range is chosen to be -/+ 5 K around the phase change temperature. These boundary conditions of the Dirichlet type (*i.e.* fixed values of a quantity) specified for the problem can be found in table 5.2.
In addition, table 5.3 lists the time intervals where the progress of melting/solidifying are evaluated. The simulation times are chosen to ensure considerable gaps in order to emphasize the progress of the solid/liqiud interface.

Mode	Charge 1	Discharge 1	Discharge 2	Charge 2	
PCM temperature	191	251	226	216	°C
HTF temperature	275	180	216	226	°C

Table 5.2: *Boundary and initial temperatures suggested for the quasi-1D study. Two examples each of the charge and discharge modes are chosen.*

Simulation times					
All cases	3	10	30	60	min.

Table 5.3: *Simulation times at which the progress of melting/solidifying PCM is evaluated.*

5.3 Boundary Condition Simplification

When HTF runs through the storage system, heat is transferred between the HTF and PCM through the pipe. In charge mode, the HTF is hotter that the PCM and in discharge mode the PCM is hotter than the HTF. Heat is transferred according to equation 5.1, where the sign of ΔT determines the direction of heat transfer and thereby if the system is in charge or discharge mode.

$$\dot{Q} = UA\,\Delta T_{lm} \tag{5.1}$$

where U is the overall heat transfer coefficient, A is the heat transfer area and ΔT_{lm} is the logarithmic mean temperature. The transferred heat causes the HTF and

PCM to change temperature. An example of this temperature change is plotted in figure 5.2, regarding which it should be mentioned that it is not a product of a simulation or calculation.

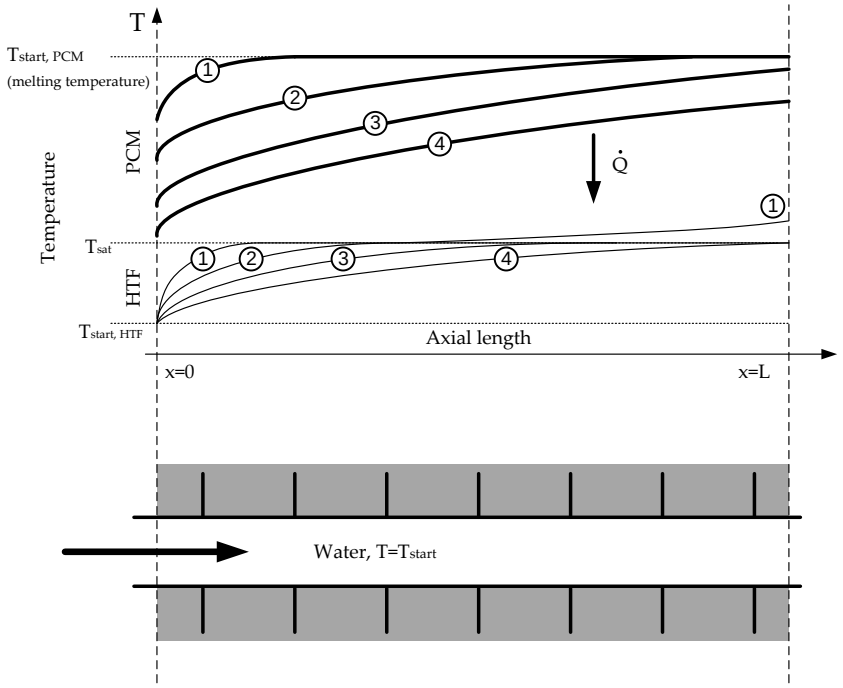

Figure 5.2: *The figure shows how HTF is let in to the pipe, and how the temperature of the HTF is increased as it flows along the x-axis. The numbers in the circles indicate different time scenarios. The higher the number, the longer the time.*

Figure 5.2 is presented as a discharge example. When the HTF flows through the pipe, heat is transferred from the PCM through the pipe in to the HTF. In figure 5.2 this is shown in the curves of case 1. Here it is shown that the PCM temperature is reduced and HTF temperature is increased. As the HTF progress further in the x-direction, the temperature approaches the PCM temperature. This means that less heat is transferred from the PCM to the HTF as a result of a lower ΔT in equation 5.1.
In figure 5.2 four different time scenarios are illustrated. Initially, the HTF starts at a given temperature. This temperature is constant, at the beginning of the pipe. As a function of pipe length, HTF temperature will approximate the PCM temperature. This is valid for both charge and discharge modes. When discharge mode is considered, and PCM is at a higher temperature than the saturation temperature of the HTF, the PCM transfer heat to the HTF above its saturation temperature. This means that the HTF becomes slightly superheated, which is illustrated in case 1 in figure 5.2. When charge mode is considered, a HTF temperature above PCM melting temperature results in a PCM temperature slightly above melting temperature.
Complete charge or discharge of the storage can be considered, when ΔT has reached a given level. Here charge or discharge becomes increasingly pointless, as a low ΔT results in a low heat transfer rate.

5.4 Delimitation - Charge mode modelling in 2D

Because of computational difficulties regarding numerical modelling of the melting aspect of the problem, only the discharge mode will be considered in this report. The authors were unable to construct a fully functional CFD simulation of the charge (*i.e.* melting) process, and they have contacted the developers of the CFD code, ANSYS, for further documentation as guidelines on this particular matter. However, a response has not been received by the scheduled report delivery day, and therefore the matter remains unsolved.
Because of this, charge mode is only considered in connection with the quasi-1D numerical model. Nonetheless, there follows a description of an example of the significance of having natural convection present in a melting process in a cavity. This example shows the tendencies assumed by the authors, as to how natural convection will affect the shape of the cavity of increasing volume, which contains melted PCM. The example presented in Patankar (1980) concerns melting around a vertical pipe immersed in a solidified material, as shown in figure 5.3. It is assumed that a hot fluid is circulated inside the vertical pipe, and that the solid medium is at its solid-liquid phase change temperature at the beginning of the example. This problem was solved by Patankar (1980) by applying a deforming computational grid due to the constantly changing position of the solid-liquid interface. The transient nature of the problem was handled by a workaround where the interface was treated as stationary at each time step, but its position was corrected between time steps to account for the heat transfer at the interface.
Results of the computations initially showed uniform melting along the length of the pipe, giving the solid-liquid interface the shape of a straight vertical line with an offset to the outer pipe surface. This result is primarily due to conduction being the domination cause of heat transfer. As the simulation time increased, heat transfer stagnates due to thermal resistance imposed by the growing fluid layer. However, at

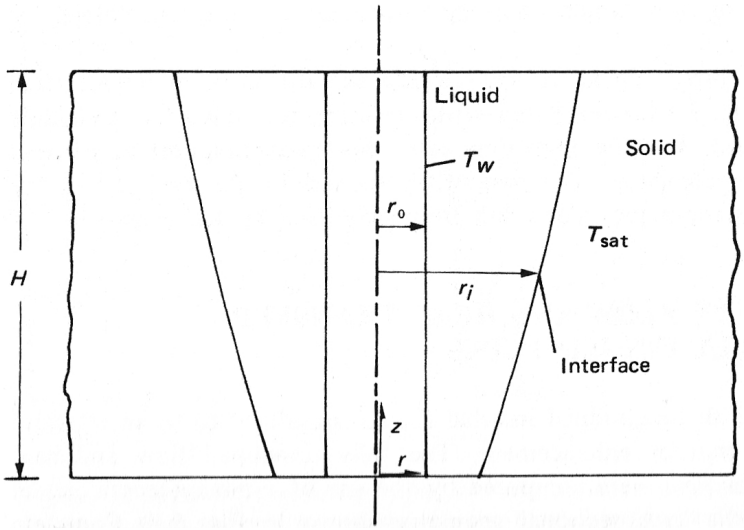

Figure 5.3: *Schematics of the example "melting around a vertical pipe". Taken from Patankar (1980).*

some later point in the simulation, the heat transfer begins to increase once again. This is due to the heat transfer starting to be dominated by a circulating flow in the melt induced by the buoyancy effects of natural convection. The circulating fluid motion causes increased melting along the length of the pipe in the upwards direction. This results in a inclined and slightly curved shape of the interface as showed in figure 5.3. Examples of streamlines of the natural convection flow in the liquid in the cavity are presented in figure C.1 in appendix C.
Supposing the analogy of the example above applies to a vertical pipe, it is the opinion of the authors of this report that conduction will initially dominate the melting process, but later will be replaced by convection dominated flow in the melt. As a consequence, the interface will have a roughly circular shape at small simulation times because of uniform melting of the solid. At larger times, the interface will start to distort and take on some irregular shape due to higher melting rate above the vertical pipe inflicted by buoyancy driven flows. This is, from an engineering point of view at the present time, believed to be the best estimate of the behaviour of the solid-liquid interface in charge mode.

Chapter

6

Quasi-1D CFD Analysis

The numerical modelling tool of CFD is applied in this work due to the difficulties involved in treating a solidification problem analytically when combined with complex geometries as encountered in Part III. CFD is used for a wide range of problems from the world of thermal-fluid sciences in both the academic environment and in many industrial aspects. In this report, however, focus will exclusively be directed towards applying CFD for solidification problems.
Regarding the structure of this chapter, sections 6.1, 6.2 and 6.5 concerns both the quasi-1D, 2D, and 3D approaches. This choice is made in order to reduce repetitions in chapter 10 concerning the 2D and 3D CFD analysis.

6.1 Governing Equations and the Solidification Model

In order to solve a solidification/melting problem ANSYS FLUENT uses a *Solidification and Melting Model* implemented on the basis of the so-called enthalpy-porosity method proposed by Voller and Prakash (1987). The general philosophy of the method is to associate control volumes in which phase change occurs with a porosity based on the liquid fraction of that given volume. It is a general applicable method for both pure substances, which undergoes isothermal phase change, and alloys where solid-liquid phase change occurs across a given temperature range defined by the concentration of the alloy elements (*cf.* the mushy zone analogy explained in section 4.2).
Earlier methods of describing solid-liquid phase change including convection heat transfer have used a deforming computational grid in order to account for the moving phase boundary. However, the enthalpy-porosity approach differs from these by not explicitly tracking this boundary, which allows for a fixed grid implementation in a numerical modelling code. Formerly, especially the treatment of the velocity as the liquid transitions to a solid have posed an issue with the fixed grid techniques. In alternative methods, this has been handled by setting velocities to zero for all control volumes having a latent heat content below some value between zero and the latent heat of the solid-liquid phase change h_{sl}. This means that zero corresponds to a completely solidified cell and a latent heat content equal to h_{sl} would correspond to a fully liquified cell. In another example, a viscosity function have been applied to mimic a phase change phenomenon, where this function has an inversely proportional relationship to latent heat content of a cell. This way, as the latent heat content approaches zero the viscosity of the fluid becomes large and thereby

approaching the properties of a solid material. The enthalpy-porosity method has some parallels to the method last mentioned. However, here viscosity is replaced by applying well-known theory of flow in porous media. The enthalpy-porosity method will be explained in the following, based on the work presented in Voller and Prakash (1987) and descriptions in FLUENT's *Theory Guide*: ANSYS (2009a).
Consider a solidification problem, where a liquid alloy melt placed in a two dimensional compartment in the yz-plane and initially held at some temperature T above its solidifying temperature. From time $t = 0$ and forward, the temperature of one of the walls in the container is lowered to some level below the solidifying temperature initiating growth of a solid layer from the cold surface and outwards into the melt. The alloy composition is not in an eutectic state hence the solidification will not happen instantly and isothermally, but across a range of temperatures; namely the temperature range of the mushy zone *i.e.* from the liquidus temperature T_{liq} to the solidus temperature T_{sol} [1]. The enthalpy H of the alloy is at all times defined as the sum of sensible enthalpy h and latent heat content ΔH

$$H = h + \Delta H \tag{6.1}$$

Due to the temperature span of the mushy zone the latent heat is formulated as a function of temperature:

$$\Delta H = f(T) \tag{6.2}$$

In order to define the above function, the latent heat of the alloy is associated with the present liquid fraction F_s of a given cell. This provides:

$$f(T) = \begin{cases} h_{sl} & T \geq T_{liq} \\ h_{sl}(1 - F_s) & T_{liq} > T \geq T_{sol} \\ 0 & T < T_{sol} \end{cases}$$

At this point, the concept of porosity ϕ is introduced where $\phi = 1$ for a liquid cell, $\phi = 0$ for a solid cell, and $0 < \phi < 1$ in the mushy zone. The porosity is related to the liquid fraction of a control volume by

$$\phi = 1 - F_s \tag{6.3}$$

Actually, the entire domain can be assumed as a porous media, with a porosity of the individual cell between 0 and 1 according to the liquid fraction of that cell. Furthermore, a superficial velocity $\mathbf{u}$ is included in the method

$$\mathbf{u} = \phi\, \mathbf{u_f} \tag{6.4}$$

where $\mathbf{u_f}$ is the real velocity of the fluid. This can be combined to

$$\mathbf{u} = \begin{cases} \mathbf{u_f} & \text{in the liquid phase} \\ \mathbf{u_f}(1 - F_s) & \text{in the mushy zone} \\ 0 & \text{in the solid phase} \end{cases}$$

Finally, by applying assumptions of Newtonian, incompressible, and laminar flow the governing equations can be defined as below.

[1] The terms *solidus* and *liquidus* temperatures are explained in section 4.2

6.1.1 Governing Equations

The Energy Equation

$$\frac{\partial \rho h}{\partial t} + div(\rho) = div(\alpha \nabla h) - S_h = 0 \tag{6.5}$$

where α is the thermal diffusivity.

Conservation of Mass

The two dimensional mass continuity equation:

$$\frac{\partial v}{\partial y} + \frac{\partial w}{\partial z} = 0 \tag{6.6}$$

where v and w are the superficial velocities in the y- and z-directions. Due to the incompressible assumption, the accumulative term $\partial \rho / \partial t$ is dropped, and only the convective term, presented in longhand notation in equation 6.6, remains.

Conservation of Momentum

$$\frac{\partial(\rho v)}{\partial t} + div(\rho \mathbf{u} v) = div(\mu \nabla v) - \frac{\partial(P)}{\partial y} + S_y \tag{6.7}$$

$$\frac{\partial(\rho w)}{\partial t} + div(\rho \mathbf{u} w) = div(\mu \nabla w) - \frac{\partial(P)}{\partial z} + S_z + S_b \tag{6.8}$$

where P is pressure, ρ is density, μ is viscosity, $\mathbf{u}$ is the vector of superficial velocities: $\mathbf{u} = (v\,,\, w)$. The source terms S_y, S_z, and S_b are explained in the following

Source Terms

The source terms of the momentum equations 6.7 and 6.8 are used to account for the behaviour in the mushy zone. In this case, the porous media flow is assumed to be governed by Darcy's Law

$$\mathbf{u} = -\frac{\mathscr{P}}{\mu} \nabla P \tag{6.9}$$

where the permeability $\mathscr{P}$ is a function of the porosity ϕ. When the solid fraction of a cell F_s increases, the porosity decreases along with the superficial velocity. This tendency is modelled by defining the source terms S_y and S_z as

$$S_y = -C\, v \qquad , \qquad S_z = -C\, w \tag{6.10}$$

The variable C will take on the value of zero in the case of $F_s = 0$ but increase to some large value as F_s approaches unity. Consequently, the source terms will only affect the solution under given circumstances. For instance, if there is a situation where a cell is fully liquified, then $\phi = 1$ is equivalent to a completely void porous media, meaning that the superficial velocity $\mathbf{u}$ equals the actual fluid velocity $\mathbf{u_f}$ by equation 6.4. In the mushy zone, C starts to increase and the source term will gradually dominate the remaining terms of the momentum equations depending on

the value of F_s. Finally, when $F_s \approx 1$ the source term will completely dominate all other terms and thereby force the superficial velocity to approach zero. Furthermore, C should be chosen appropriately in order to imitate the behaviour in the mushy zone correctly (Voller and Prakash, 1987). However, this is not the main focus of this discussion, so therefore the reader is referred to Voller and Prakash (1987) if more information about the topic is desired.
In order to account for buoyancy driven natural convection flows occurring in the compartment, an extra source term S_b is added in the momentum equation where the gravitational force applies, which in the present case is the z-direction. This is defined by

$$S_b = \frac{\rho\, g\, \beta(h - h_{ref})}{c_p} \tag{6.11}$$

where h_{ref} is the reference enthalpy. The source term of the energy equation (6.5) is defined as

$$S_h = \frac{\partial\, \rho\, \Delta H}{\partial\, t} + div(\rho\, \mathbf{u}\, \Delta H) \tag{6.12}$$

which is derived from an enthalpy formulation of convection-diffusion phase change. The latter convective term in equation 6.12 becomes zero in the case of an isothermal phase change *i.e.* if an eutectic mixture or a pure material is considered.

6.1.2 Limitations of FLUENT's Solidification Model

FLUENT's Solidification Model has some limitations regarding its use, and the most relevant for this particular problem are included in the following. A complete list of limitations is provided in ANSYS (2009a).
There are two types of solvers available in FLUENT: the pressure-based and the density based solver. The main difference between the two lies in the method of solving for the pressure field. The pressure-based solver expresses the pressure field by means of pressure correction equations which originates from the manipulation of the continuity and momentum equations. The density based solver uses the continuity equation to determine the density field while solving the pressure field through the equation of state ANSYS (2009a). The Solidification Model is only compatible with FLUENT's pressure-based solver.
Furthermore, only the implicit formulation is available for the pressure-based solver. The fully implicit formulation is, as opposed to the explicit formulation, unconditionally stable, meaning that no stability criteria with respect the time step size $\Delta\, t$ has to be met.

6.2 Solver Settings in FLUENT

The solver set-up is largely based on the recommendations provided in ERCOFTACs "Best Practice Guidelines", Casey and Wintergerste (2000), and the documentation accompanying the ANSYS FLUENT CFD code (ANSYS (2009a)).

6.2.1 Temporal Discretisation

Both First Order and Second Order Implicit formulations of time discretisation are available in FLUENT. Casey and Wintergerste (2000) recommends second order accuracy in both space and time for all transient simulations, while ANSYS (2009b) mentions that First Order is adequate for most problems, but Second Order could be applied if higher accuracy is needed.
In this text, the First Order Implicit discretisation is applied for all simulations. This is due to the Second Order formulation yielding a non-physical solution of 1D simulation of discharge 2, as seen later in figure 6.10.

6.2.2 Time Step

CFD simulations are solved as a transient heat and flow problem due to the time dependent nature of the solidification problem, and the progress in time is quantified via the time step Δt. Between each time step, the discretised governing equations are solved iteratively until the preset level of convergence is achieved.
The size of the time step should correspond to the time scale of the given problem in order to pick up time dependent phenomena with adequate resolution. In fact, ANSYS recommends a Δt of at least one magnitude less than the smallest time constant of the problem (ANSYS, 2009a). Moreover, the time step size could be determined from the number of iterations required for each step, where ANSYS regards 5-10 iterations as being the optimum number. If the solver needs fewer iterations than this, it would be more economical, from an overall time consumption point of view, to increase the time step size, and vice versa for a large number of iterations (ANSYS, 2009a).
Furthermore, ANSYS suggests to start transient simulations with a relative small time step in order to achieve better resolution of the rapid changes that often characterise transient problems in their very beginning. Later, the size of Δt could be increased if desired.
Concerning the present system modelled in this report, the focus is not solely directed towards phenomenons occurring in the start-up process of the problem. It is acknowledged that the solidification of nitrate salt in a latent heat storage facility will happen across some larger time scale, in order to produce steam for the turbine for a significant period of time. Therefore, the main focus is dedicated to this aspect rather than the initial behaviour. These considerations also formed the basis for the decision that four simulation times (3, 10, 30, and 60 minutes, see table 5.3) were appropriate for the purpose of the study.
During the CFD simulations, the approach suggested by ANSYS concerning small initial time steps did not contribute to convergence. On the contrary, if the approach was reversed so a large step size was used for the first 4-5 time steps and then reduced to some value, say a magnitude smaller, better convergence was achieved. Finally, only fixed time stepping was used for the simulations, however, adaptive time stepping is available in FLUENT.

6.2.3 Residuals

When referring to *residuals* in this report, there is actually being referred to *scaled* residuals. It is the default setting in FLUENT to scale the residuals when expressing the convergence history. The unscaled residual is given as the numerical error of the solution summarised across all cells. FLUENT scales this residual by a factor representative of the flow in the domain, because scaled residuals are often more meaningful to the problem considered. An example is the momentum equations, where the residual is scaled with respect to the largest absolute value of the first five iterations.

6.2.4 Convergence

Convergence of a timestep is considered obtained when the numerical error of the iterations have decreased to an acceptably low level. In general, the criteria of when an iterative method is said to be converged to a solution can be defined as a fixed number of iterations, an absolute value of the residual, or as an relative change of the residual. In this report, the default absolute convergence criteria proposed by FLUENT are applied, which are presented in table 6.1. However, in the transient version of FLUENT, a maximum number of iterations per time step can be specified. If the convergence criteria are met before the maximum iteration limit is reached, the solution will proceed to the next time step. The maximum limit is usually set to 30-35 iterations, which is normally only reached in case of the few initial large time steps.

Equation	Criteria (absolute)
Mass Continuity	$1 \cdot 10^{-3}$
x-momentum	$1 \cdot 10^{-3}$
y-momentum	$1 \cdot 10^{-3}$
z-momentum	$1 \cdot 10^{-3}$
Energy	$1 \cdot 10^{-6}$

Table 6.1: *Absolute convergence criteria of the computation residual used for all CFD simulations.*

6.2.5 Boundary Types

The types of boundaries of the computational domains considered in the following CFD studies are either of the *wall* or *symmetry* type. The wall boundary condition is used to separate a fluid and solid zone and imposes a no-slip condition by default in terms of the fluid-wall interaction. A number of thermal conditions can be specified for a wall boundary, but in this report the constant temperature condition is used.
The symmetrical boundary condition is used wherever the computational domain can be designed to exploit the symmetric nature of a given problem. This way, a larger area of interest can be reduced to a relatively small domain and hereby decrease the computational load. No inputs are needed specified for the symmetric

boundary condition, which often helps to simplify the numerical representation of a real problem. At symmetric boundaries in FLUENT, all fluxes of quantities are considered to be zero.

6.3 Quasi-1D CFD Simulation Presentation

The quasi-1D grid used in CFD simulation of the phase change process in the storage charge and discharge modes is presented in figure 6.2. It is given the name *grid 100* and has 65 cells in the radial direction and 15104 cells in total. According to the introductory description in chapter 5, the geometry consists of two concentric circles with the space in between being the area of interest. The outer PCM boundary diameter (outer perimeter) is four times the diameter of the outer pipe surface (inner perimeter). Note that the inner perimeter of the pipe is not included in the grid as this is best specified later by settings in FLUENT.
The entire space between the concentric circles is selected as computational domain. It is possible to this without computational time reaching an unacceptable level because of the simplicity of this stationary transient heat conduction problem. However, it is acknowledged that a smaller wedge-shaped section of the domain could be meshed instead as a representative of the entire circular domain. The latter procedure is used later in the more detailed 2D analysis in chapter 10.

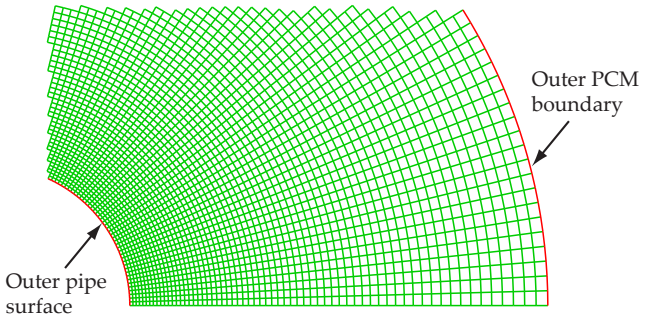

Figure 6.1: *Section close-up of grid 100.*

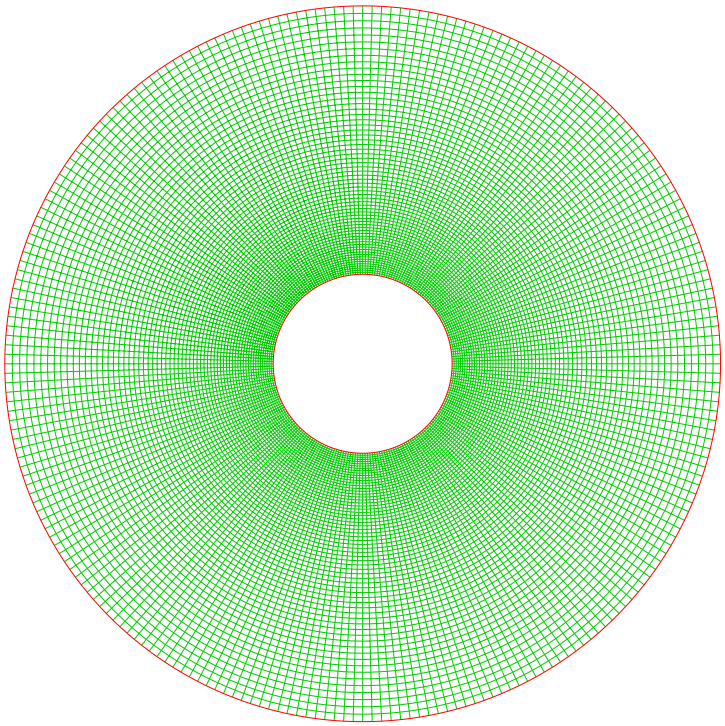

Figure 6.2: *Full view of the grid (denoted* grid 100*) used for the quasi-1D simulation.*

6.4 Grid Independence

Six grids with varying densities are constructed to examine when a solution independent of the grid density can be obtained. The grids share the same general layout so the difference lies solely within resolution of the grid. Detail of the grids are provided in table 6.2. The grids are named according to their total number of cells relative to grid 100, which acts as a point of reference. To provide an example: the total number of cells of grid 22 is 0.22 times that of grid 100, and correspondingly: grid 548 has 5.48 times the number of cells of grid 100.

Index	No. of cells, domain total	No. of cells, radial direction
22	3360	31
61	9212	50
100	15104	65
375	56644	120
548	82844	150
801	121004	180

Table 6.2: *Grid size details of the six grids considered for the grid independency study.*

The effect of grid density is normally evaluated by monitoring some meaningful parameter (a velocity in a flow simulation, for example) as the grid density is altered and maybe comparing the parameter to some experimental data as well. As this

quasi-1D solidification simulation only considers completely motionless fluids (and solids, for that matter), the parameter chosen for this grid independency study is the temperature profile in the PCM at a given time, which is here 10 minutes for all grids. The temperature profile presented is evaluated along a radial line from the outer pipe surface to the outer PCM boundary, as explained in figure 6.3.

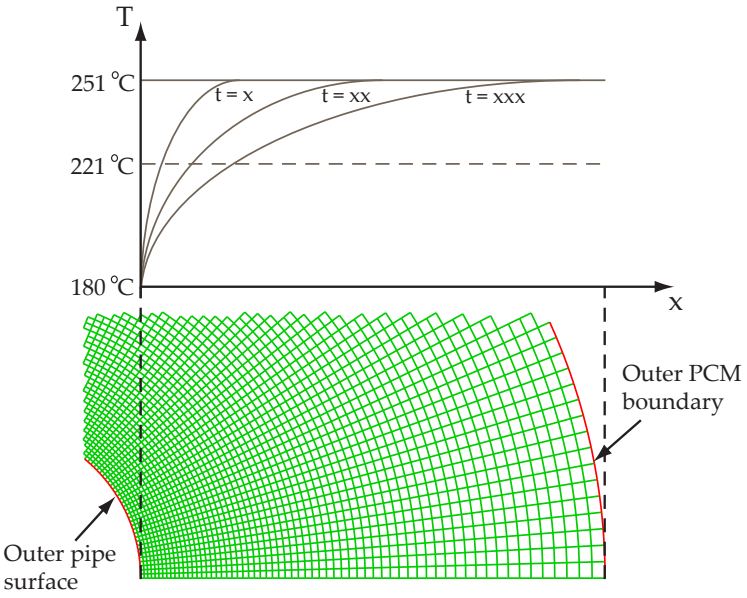

Figure 6.3: *Time dependent temperature profiles of the PCM evaluated along a line in the radial direction. Here shown for an example of discharge mode.*

Temperature profiles in discharge mode for all six grids are presented in figure 6.4. Generally, the profile for all grids coincide, and only minor variation is seen around the phase change temperature. The more dense grids seem to have a smoother profile around the phase change temperature. Therefore, it appears that the solid-liquid interface can be traced with higher resolution, which is also a logical result of higher grid density.
Figure 6.5 shows the computational time[2] for each of the six grids with simulation time of 10 minutes. The simulations were all carried out with identical computational resources, and further details of this and the general practical approach in connecting with the simulations are described in appendix D. Grids 22 to 100 can be computed fairly fast due their coarse structure, which can be seen from figure 6.5. Inevitably, a decrease in grid size will cause an increase in computational time and this is clearly seen for grids 375 to 801, which have significantly higher grid densities and correspondingly requires longer time to solve.

A suitable grid is chosen for the quasi-1D study based on figures 6.4 and 6.5. It is found that the increase in computational time associated with finer grids is not fully justified by the minor increase in precision of the solid-liquid interface. Consequently, the coarser grids appear as being more attractive than the high resolution grids.

[2]In this report, *computational time* means *wall clock time*.

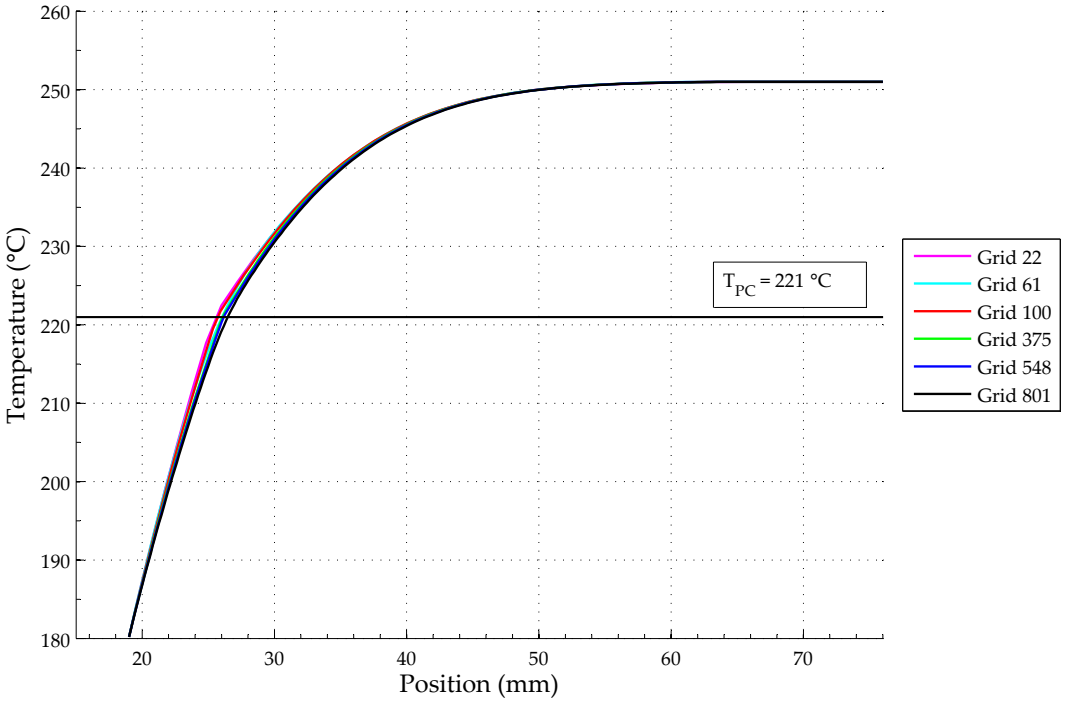

Figure 6.4: *Temperature profiles of the grids reviewed in the grid independency study (discharge mode 1, 10 minutes).*

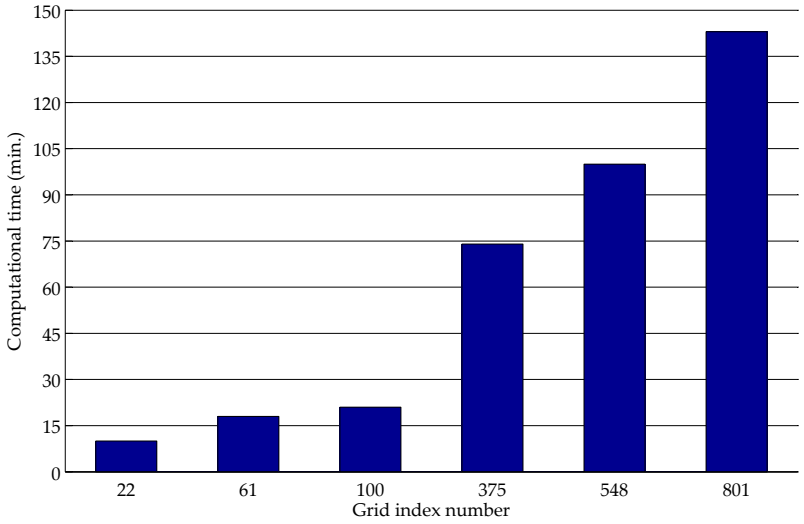

Figure 6.5: *Computational time for the reviewed grids. Note that the sudden jump in computational time from grid 100 to grid 375 is caused by significant increase in the number of cells.*

Because of this, grid 100 is found acceptable and is therefore selected as the preferred grid for quasi-1D simulations.

6.5 Grid Quality

Discretisation, whether spatial or temporal, will induce some error in the CFD simulation. Therefore, in order to reduce these errors it should always be the practice to produce a computational grid that resembles the real geometry as close as possible (Versteeg and Malalasekera, 2007). Furthermore, the grid should be constructed with sufficiently high quality, which in this context deals with design and shape of the grid. Having a high quality grid does not guarantee a correct solution, but it can contribute to a more accurate result (Mandø, 2009). In the worst case, poor quality grids can cause convergence problems.
The grid quality is, in this work, evaluated through three characteristic numbers of the grid cell elements: angular skewness, size change, and aspect ratio. Starting with the first mentioned, the maximum angular skewness is expressed in equation 6.13, with geometrical meaning of the angles involved explained in figure 6.6a.

$$Q_{EAS,max} = max\left[\frac{\theta_{max} - \theta_e}{180 - \theta_e}, \frac{\theta_e - \theta_{min}}{\theta_e}\right] \tag{6.13}$$

In equation 6.13, θ_{max} is the largest angle in a face or cell, θ_{min} is the smallest angle in a face or cell, and θ_e is the angle of a equiangular face or cell. $Q_{EAS} = 0$ applies to perfectly orthogonal cell elements while a Q_{EAS} value of 1 indicates a degenerate element. Casey and Wintergerste (2000) recommends that highly skewed cells should be avoided and more precisely that $\theta_{min} > 40°$ and $\theta_{max} < 140°$, which corresponds to $Q_{EAS} < 0.56$. If this criteria is not fulfilled, it could cause *"a deterioration in the results or lead to numerical instabilities"* (Casey and Wintergerste, 2000, 15). Moreover, it is strongly recommended that elements adjacent to boundaries of the computational domain (*i.e.* walls, inlets, outlets, etc.) are perfectly orthogonal or very close to. Other guidelines prescribe that for high quality 2D grids, Q_{EAS} should be ≈ 0.1 on average (Mandø, 2009).
The size change of cells describes the ratio of expansion in the grid. More specifically, it is a size measure of the cell of interest compared the sizes of neighbouring cells. If figure 6.6b is considered, the largest size change occurs between the cell of interest A_i and the largest neighbouring cell $A_{j=3}$. The maximum size change between two adjacent cells in a grid is presented in equation 6.15. Note that unless a perfectly uniform grid is considered then by definition $Q_{SC} > 0$.

$$Q_{SC,max} = max\left[r_1, r_2, \ldots, r_n\right] \tag{6.14}$$

$$r_i = \frac{\text{Area of element } i}{\text{Area of neighbouring element } j} \tag{6.15}$$

Casey and Wintergerste (2000) notes that the size change ratio should be observed because different CFD codes have individual tolerances towards this aspect of the grid quality. Furthermore, guidelines dictates smooth rates of grid expansion, which is particularly important in regions with large changes (Casey and Wintergerste, 2000). In this text, a maximum cellular size change ratio of <2 in the region of interest, as presented by Mandø (2009), is acknowledged.

Finally, the aspect ratio of grid elements, which is the ratio of the sides of a cell, should be considered. Generally high aspect ratios should be avoided in regions away from boundaries, and according to the guidelines it should not exceed the range 20 to 100 in important regions. Specific tolerances regarding aspect ratios depend on the individual solver used for the problem (Casey and Wintergerste, 2000).
The characteristic numbers of the 2D grid used in the quasi-1D approach are given in table 6.3.

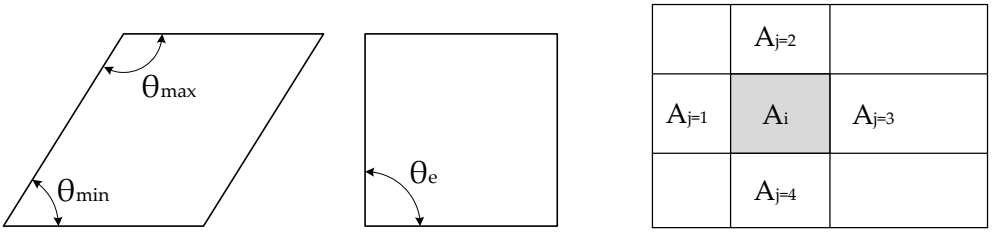

(a) *Angles of a quadrilateral cell element used to evaluate angular cell skewness.*

(b) *Areas of neighbouring quadrilateral cell used to evaluate the size change of cells.*

Figure 6.6: *Angles and areas used for evaluation of angular skewness and size change of cells. Here showed for a 2D grid. Reproduced by the authors from Mandø (2009).*

Index	**No. of cells**	**Angular skewness** Q_{EAS}	**Size change** Q_{SC}	**Aspect ratio** Q_{AR}
22	3360	0.01 - 0.02	0.9 - 1.2	1.2 - 1.3
61	9212	0.01 - 0.02	0.99 - 1.07	1.17 - 1.25
100	15104	0 - 0.1	0.99 - 1.05	1.2 - 1.27
375	56644	0 - 0.1	0.99 - 1.03	1.12 - 1.17
548	82844	0 - 0.1	0.99 - 1.02	1.18 - 1.25
801	121004	0 - 0.1	0.99 - 1.02	1.18 - 1.24

Table 6.3: *Characteristic numbers of the grid quality.*

It is clear from table 6.3 that the present grid meets the recommendation presented above for grid design. However, this is not surprising because of the extremely simple geometry used for the simulation. In conclusion, the grid created for the quasi-1D approach to the solidification problem is, on basis of the above analysis, assumed to be of a high quality and should not contribute to significant inaccuracies in the results.

6.6 Quasi-1D CFD Results

Due to the stationary condition of the PCM, only the energy equation is being solved. Convergence history for the initial time steps are presented in figure 6.7, from which it can be seen that the convergence criteria for the energy equation is rapidly met

with a time step size of 0.1 s. Furthermore, the First Order Upwind scheme was used for discretisation in both time and space.

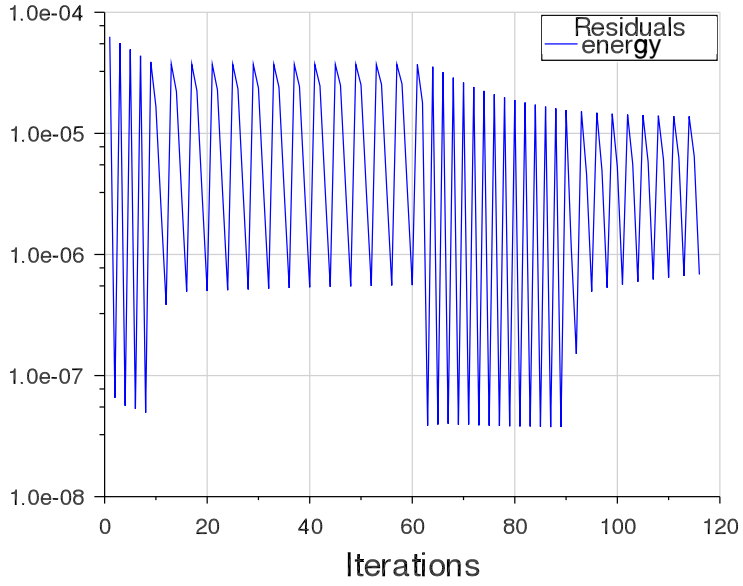

Figure 6.7: *Residuals of the energy equation for the 1D CFD simulation. A fixed time step size of 0.1 s is applied.*

Illustration 6.8 shows the temperature contours of the time-dependent solution. As expected, the temperature distribution in the liquid PCM is uniform around the pipe with variations occurring in the radial direction only. Because of this, each evaluation point in time (3, 10, 30, and 60 minutes) are restricted to a single quadrant in figure 6.8 in order to present the results in a more compact form.
Figure 6.12 shows the progress of the solid-liquid interface over time. In line with the temperature distribution, the PCM solidifies uniformly around the pipe. Moreover, quantified plots of temperature and liquid fraction are presented in figures 6.11 and 6.12.
The decision of using the First Order Upwind scheme for all simulations was motivated by the fact that some non-physical result were encountered when the Second Order Upwind scheme was applied to the discharge 2 problems. An example of this is shown in figure 6.10, which is the liquid fraction contours recorded at 30 minutes

of simulated time. As no natural convection effects can occur in the quasi-1D study due to the lack of gravitational forces, the shape of the interface is expected to be smooth as a result of heat diffusion in a motionless material. because of this, the result is regarded as being an incorrect solution, and the First Order Upwind scheme is the preferred choice for all simulations.

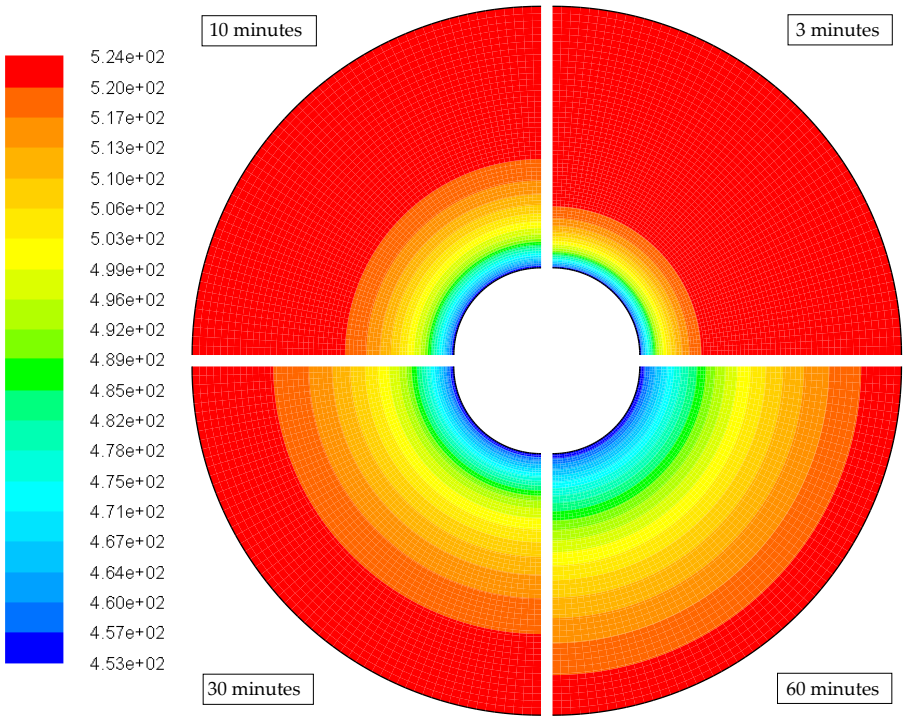

Figure 6.8: *Temperature contours of the four simulation periods; 3, 10, 30 and 60 minutes, depicted in each corner of the figure. Note the temperature scale is presented in K.*

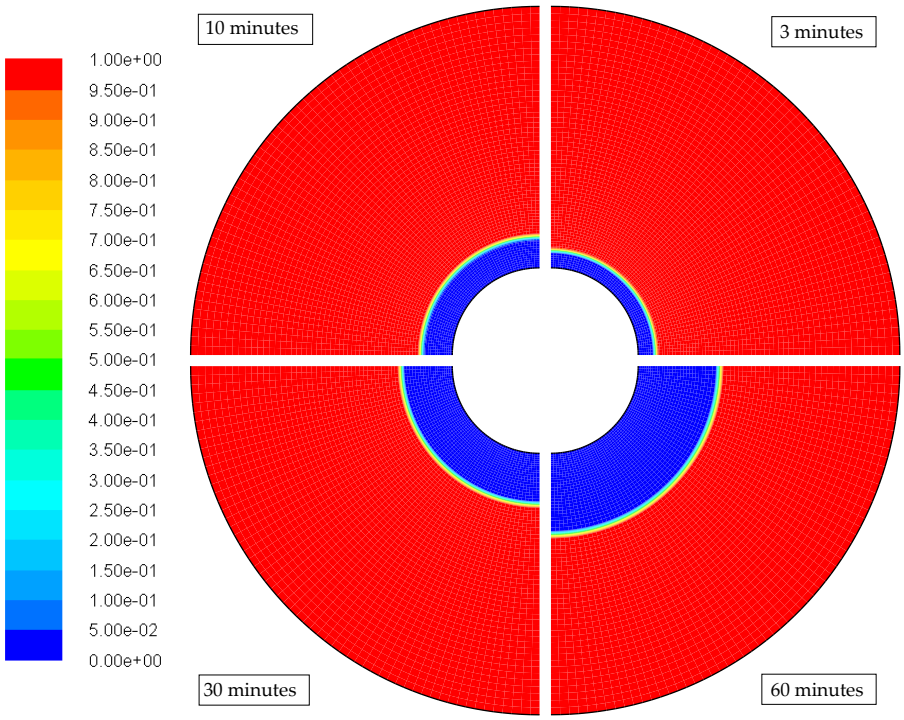

Figure 6.9: *Contours of the solid/liqiud fraction shown for the four simulation periods; 3, 10, 30 and 60 minutes.*

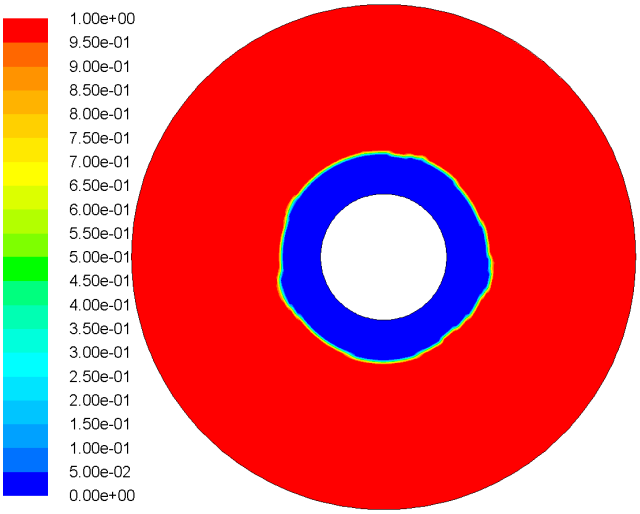

Figure 6.10: *Distorted interface shape experienced with second order schemes. Depicted here for 30 minutes.*

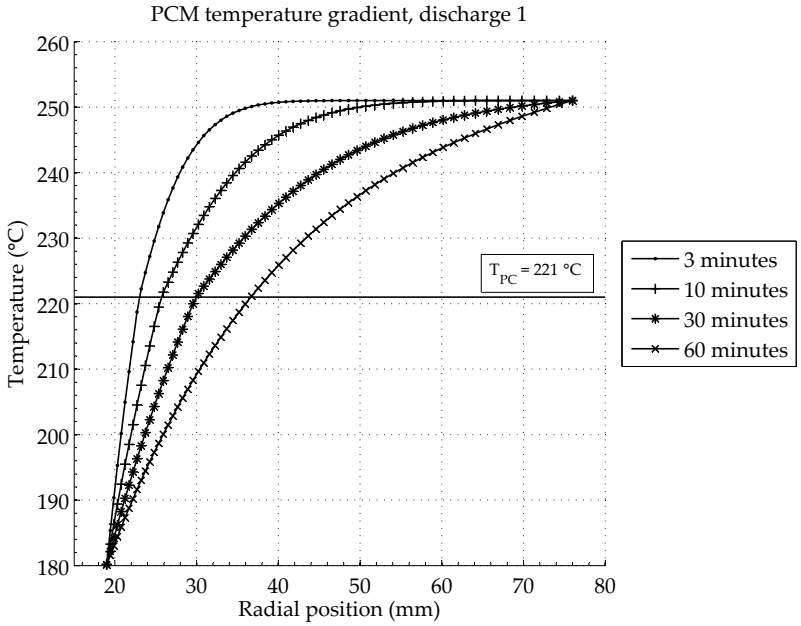

Figure 6.11: *Temperature profile in the radial direction.*

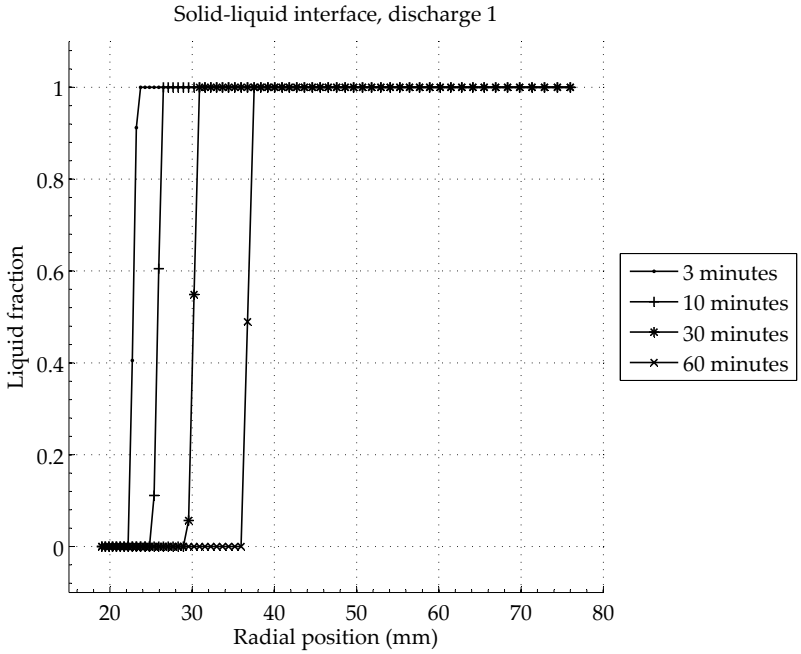

Figure 6.12: *Plot of the liquid fraction vs. time and radial position.*

Chapter

7

Quasi-1D Numerical Model

To model the heat storage using numerical methods, a model was created in MATLAB. The chosen method for the model is the *Resistance-Capitance Formulation* which is described in Mills (1995), as a finite volume formulation. The model was inspired by some similar work (Condra, 2011). This method is well suited for multidimensional unsteady conduction with internal heat generation and variable thermal properties, which makes it suitable for solving heat conduction in a phase changing material.
To evaluate the transferred heat from the HTF through the pipe in to the PCM and vica versa, the amount of heat is calculated as

$$\dot{Q} = UA\Delta T \tag{7.1}$$

where U is the *overall heat transfer coefficient*, A is the area and ΔT is the temperature difference. The amount of heat transfered in the system is highly dependent on U.

7.1 Overall Heat Transfer Coefficient

UA is a coefficient for the combined heat transfer and is given as the inverse of the total thermal resistance through the given media. As the wall in the model is a pipe wall, outer area is a function of pipe diameter, and is thereby variable. To evaluate heat transfer through this variable area, the combination of heat transfer coefficient and area is evaluated.

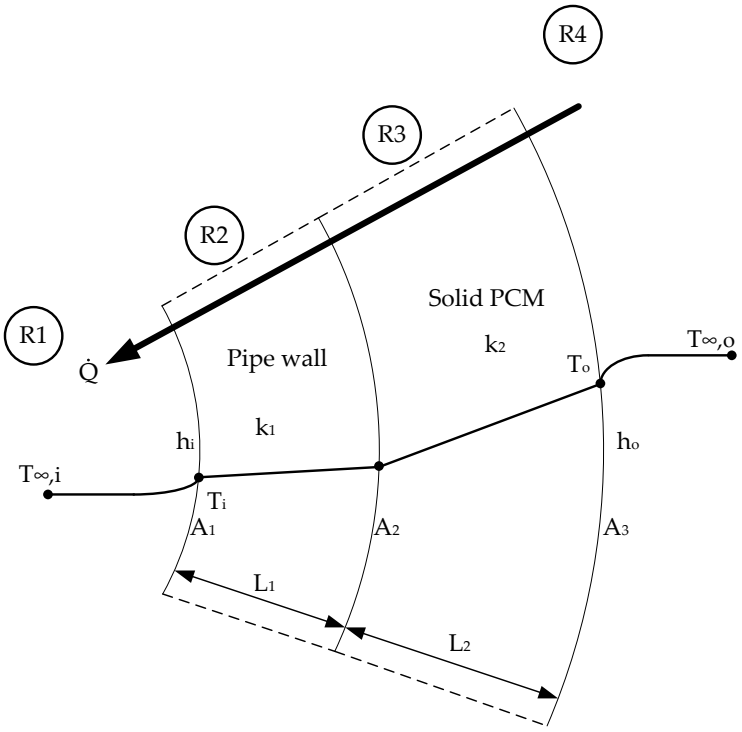

Figure 7.1: *Illustration of the heat transfer through pipe wall and solid PCM.*

As is illustrated in figure 7.1 heat transfer in the heat storage is a matter of four different situations. Each situation is evaluated through a thermal resistance given as

$$R1 = \frac{1}{h_1 A_1} \tag{7.2}$$

$$R2 = \frac{1}{k_1 A_{m1}/L_1} \tag{7.3}$$

$$R3 = \frac{1}{k_2 A_{m2}/L_2} \tag{7.4}$$

$$R4 = \frac{1}{h_2 A_3} \tag{7.5}$$

$$\tag{7.6}$$

The UA value is then given as

$$UA = \frac{1}{R_1} + \frac{1}{R_2} + \frac{1}{R_3} + \frac{1}{R_4} \tag{7.7}$$

As a cylindrical pipe is evaluated, the area is subjected to change in the heat flow direction. This means that R2 and R3 are variable according to the layer thickness L1 and L2. As the pipe wall has a constant thickness, L1 is correspondingly constant, which means that R2 also is constant. L3 is changing as the PCM layer changes during charge and discharge, which means that either inner or outer area changes. The mean area is therefore given as

$$A_m = \frac{A_o - A_i}{\ln\left(\frac{A_o}{A_i}\right)} \tag{7.8}$$

where A_o is the outer area (m^2) of the evaluated shell and A_i is the inner area (m^2) (Condra, 2011). Equation 7.8 is a logarithmic mean area, which is more precise formulation of mean area for this case.
The "A" used in UA is the area which is used to define the heat transfer. "A" could be the inner or outer area of the pipe. With the nature of UA, it is important to evaluate the size of the thermal resistances in question, as the lowest thermal resistance is dominating UA. The thickness of the pipe wall is small and the conductivity of the material is relatively high, which can be seen from table 4.1 and 4.4. The thermal resistance of the pipe wall is therefore neglected.
To increase the heat transferred per volume of the heat exchanger, fins are added to the heat surfaces. Fins can obviously be added on both the inner and outer surface, but as has just been shown, to benefit the most, fins must be added to the side where resistance is highest, thus the PCM side of the heat exchanger.
To evalutate the thermal resistances, the following is an investigation of the heat transfer coefficients on the inner side of the pipe for condensation in charge mode and evaporation in discharge mode.

7.1.1 Internal Heat Transfer Coefficient

Heat transfer to and from the HTF takes place on the inside of the pipe. In charge mode saturated steam is led through the pipe, where it is condensated on the pipe wall, transferring heat through the pipe to the PCM. In discharge mode saturated water is led through the pipe, where it absorbs the heat from the PCM, which causes the water to evaporate. For the evaluation of the heat transfer coefficient only horizontal tubes are considered.

Condensation in horizontal tubes

Correlations for condensation inside horizontal tubes have been very difficult to find. For this reason, and for simplicity, condensation inside horizontal tubes is calculated as condensation on the outer surface of a horizontal tube. According to Mills (1995), latent heat of vaporization, h_{fg}, should be corrected due to subcooling. The corrected latent heat of vaporization is denoted h'_{fg} and is found by

$$h'_{fg} = h_{fg} + \left(0.683 - \frac{0.228}{Pr_l}\right) c_{p,l}(T_{sat} - T_w) \tag{7.9}$$

which is inserted to the equation for heat transfer coefficient for condensation on a horizontal tube:

$$h = 0.728 \left(\frac{(\rho_l - \rho_v)\, g\, h'_{fg}\, k_l^3}{\nu_l\, D\, (T_{sat} - T_w)}\right)^{1/4} \tag{7.10}$$

where ρ is the density for liquid and vapour, g is the gravitational constant, h'_{fg} is the modified latent heat, k_l is the liquid thermal conductivity, ν_l is the kinematic

viscousity for liquid, D is the pipe diameter, T_{sat} is the saturation temperature of the vapour and T_w is the wall temperature.

Evaporation/Boiling

A common value for the heat transfer coefficient in evaporation is 10^4 W/m^2K (Sørensen, 2011). If the heat flux $\dot{q}$ is known, the heat transfer coefficient could be calculated by the Mostinski correlation as shown in equation 7.14.

$$P_r = \frac{P}{Pc} \tag{7.11}$$

$$A = 0.1011 Pc^{0.69} \tag{7.12}$$

$$F = 1.8 P_r^{0.17} + 4 P_r^{1.2} + 10 P_r^{10} \tag{7.13}$$

$$h = A\, \dot{q}^{0.7} F \tag{7.14}$$

where Pc is the critical pressure of the fluid (221.1 bar for water), P is the working pressure, $\dot{q}$ is the heatflux (W/m^2) and and h is the heat transfer coefficient (W/m^2K). However, the heat flux is unknown. In practical applications a heat flux is known from desired output effect, $\dot{Q}$ (W) and heat surface area, A (m^2). As these figures are unknown, a heat flux can not be accurately determined. Instead a heat transfer coefficient of h = 10^4 W/m^2K is used as reference. With this in mind, the Mostinski correlation is used for calculating the required heat flux, in order to get a heat transfer coefficient of 10^4 W/m^2K.

Coefficient presentation

In table 5.2 the temperatures of the different charge and discharge modes are presented. With these temperatures, the heat transfer coefficients are calculated. The results are shown in table 7.1.

	Charge 1	Discharge 1	Charge 2	Discharge 2	Unit
Heat transfer coefficient	6766	10000	12500	10000	W/m^2K
Thermal resistance	$1.47\ 10^{-3}$	$9.95\ 10^{-4}$	$7.96\ 10^{-4}$	$9.95\ 10^{-4}$	K/W
Heat flux	$5.68\ 10^5$	$5.4\ 10^4$	$1.25\ 10^5$	$3.9\ 10^4$	W/m^2

Table 7.1: *Heat transfer coefficient for the different scenarios evalutated for the temperatures presented in table 5.2.*

In table 7.1 thermal resistances are evaluated according to equation 7.2 with an area of 0.1 m^2 equivalent to a pipe internal diameter of 32 mm. Heat flux for discharge 1 and discharge 2 are estimated using the given heat transfer coefficient and the Mostinski correlation.

7.1.2 External Heat Transfer Coefficient

The material outside the tube is PCM. As is already documented in table 4.4 conductivity is low in both solid and liquid phase. In solid phase heat transfer is purely

by conduction, while in liquid phase there is a convection contribution. Convection is, however, not included in this quasi-1D model. This is to be evaluated in the 2D investigation. Hence, both solid and liquid phase is evaluated by conduction.

Conduction Heat Transfer Coefficient

Thermal resistance by conduction is given as equation 7.4 where L_2 is the thickness of the solid layer of PCM. As the thickness of the layer varies with time, it is difficult to calculate a specific thermal resistance R. Instead the thermal resistance is presented in figure 7.2 as a function of layer thickness.

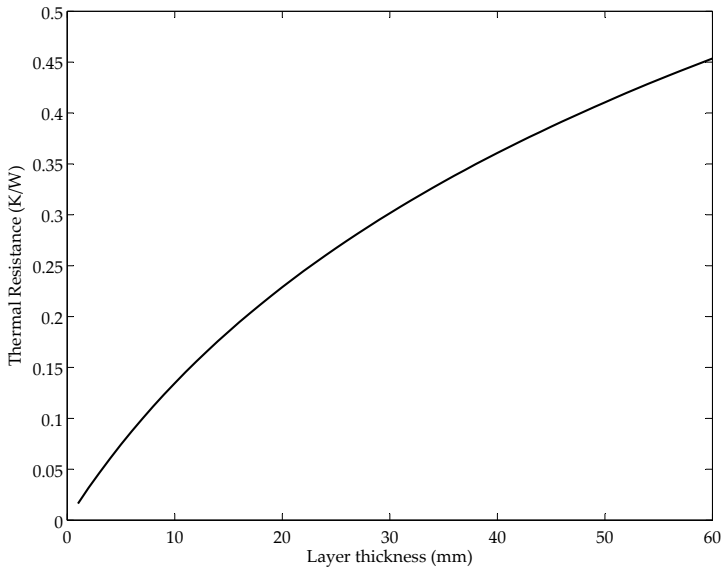

Figure 7.2: *Presentation of thermal resistance in PCM layer as a function of layer thickness. Inner radius is set as equal to the outer radius of the pipe, and is thereby fixed.*

Layer thickness is the difference of inner and outer radius. The figure shows, that thermal resistance increases with layer thickness. It can be seen from figure 7.2 that the thermal resistance starts around 0.016 $^K/_W$ and ends at around 0.45 $^K/_W$.

7.1.3 Summary

Thermal resistances have now been evaluated in order to determine the heat transfer in the system. Via the thermal resistance it can also be evaluated where fins could be added for higher heat transfer. It is in equation 7.7 determined how UA equals the inverse of the total thermal resistance. It is also described how a thermal resistance is determining the size of UA, if the resistance is much larger then the others. To get an overview of the thermal resistances, they are all shown in table 7.2.

		Charge 1 Condensation	Discharge 1 Evaporation	Charge 2 Condensation	Discharge 2 Evaporation	PCM Conduction
Thermal resistance	K/W	1.47 10^{-3}	9.95 10^{-4}	7.96 10^{-4}	9.95 10^{-4}	1.6 10^{-2} - 4.5 10^{-1}

Table 7.2: *Thermal resistances for condensation and boiling of HTF and conduction in PCM.*

As table 7.2 clearly shows, the highest thermal resistance is in the PCM, which indicates that adding fins to the outside of the pipe increases heat transfer.

7.2 Numerical model

As is described in section 5.1, a quasi-1D model is constructed. The model is for a smooth pipe imbedded in PCM, as shown in figure 5.1. The model is discretised in to a number of control volumes to form a mesh of nodes. The accuracy of the model increases with the number of nodes. An illustration of a control volume with a node m is presented in figure 7.3.

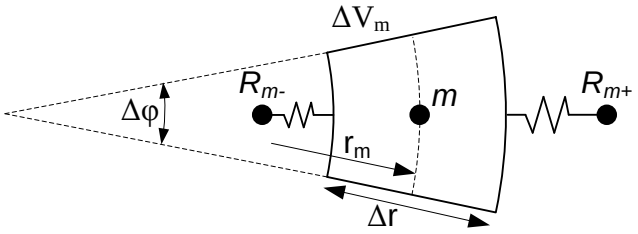

Figure 7.3: *Illustration of a node volume.*

The size of each volume is calculated as

$$\Delta \mathrm{V} = \mathrm{r}_m \Delta \mathrm{r} \Delta\phi \Delta \mathrm{z} \tag{7.15}$$

Heat conduction in to each volume is governed by thermal resistance coefficient R, which is given by

$$\mathrm{R} = \frac{\mathrm{L}}{\mathrm{kA}} \tag{7.16}$$

where L is the length in meter through the volume, k is the thermal conductivity, and A is the area connecting one volume with the neighbouring. For each node an R_{m+} and R_{m-} is found. R_m is the notation for the thermal resistance in the radial direction. Thermal resistances can also be calculated for the axial and circumferential direction for multidimensional problems.
Thermal resistances for the quasi-1D problem in a cylindrical coordinate system is found by

$$\mathrm{R}_{m+} = \frac{\Delta r}{(r_m + {}^{\Delta r}/_2)\,\Delta\phi\,\Delta z\,k} \tag{7.17}$$

$$\mathrm{R}_{m-} = \frac{\Delta r}{(r_m - {}^{\Delta r}/_2)\,\Delta\phi\,\Delta z\,k} \tag{7.18}$$

where r_m is the distance from centre to the node, Δr is the radial length of the volume and k is thermal conductivity. Δz is the volume length in axial direction, which is set to 1 in this quasi-1D model.
An important factor in the *resistance-capacitance formulation* is the C_m value which is the thermal capacitance given by

$$C_m = \rho_m \, c_{p,m} \, \Delta V \tag{7.19}$$

C_m describes how much energy must be added to the specific volume to change the temperature by 1 K.
For each control volume a heat balance can be calculated. When, as in this case, no internal heat generation is present, the heat balance is given as

$$C_m \frac{T_m^{i+1} - T_m^i}{\Delta t} = \sum_n \frac{T_n^i - T_m^i}{R_{mn}} \tag{7.20}$$

where the superscripts refer to the time step. The subscripts refer to the volume, where n refers to neighbouring volumes, while m refers to the present volume. R_{mn} is the sum of the surrounding volumes. Equation 7.20 is an explicit formulation. To preserve this formulation C_m and R_{mn} should be calculated for each time step i, when properties are temperature dependent. Properties like c_p and k are obviously temperature dependent, but if the working temperature range is relatively small, fixed values can be applied, which is also described in section 4.1.4.
Equation 7.20 can be solved for T_m^{i+1}, which gives

$$T_m^{i+1} = (1 - \frac{\Delta t}{C_m} \sum_n \frac{1}{R_{mn}}) T_m^i + \frac{\Delta t}{C_m} \sum_n \frac{T_n^i}{R_{mn}} \qquad (^\circ C) \tag{7.21}$$

7.3 Heat Balance

As energy transport in and out the system can only come from the HTF, an energy balance can be made with the heat input from the HTF compared to energy stored in the system. Energy input is calculated using equation 7.22, where ΔT is given by the difference between nodal temperature and HTF temperature. The resistance and temperature in equation 7.22 is evaluated for each timestep and finally summarized. This yields the amount of heat in to the system, and must then be compared to the energy change in the system.
For each node in the system C_m is calculated as in equation 7.19. When starting temperature and final temperature of each node is known, C_m is used to calculate the amount of heat stored in the system. The heat balance is then given as

$$\frac{\Delta T \, \Delta t}{R} = C_m \, \Delta T \tag{7.22}$$

From the simulations for 100 nodes in the mesh independency analysis in section 7.6, the amounts of heat is presented in table 7.3.

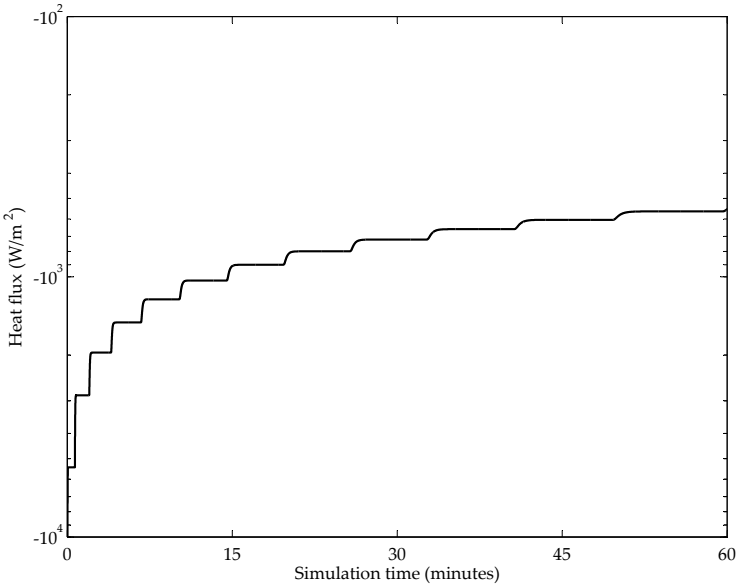

Figure 7.4: *The absolute value of heat flux is decreasing with time according the decrease in temperature difference. The steps are due to phase change in nodal points.*

Mode	Simulation time (minutes)	Heat input (J)	Net stored energy (J)
Charge 2	3	$1.9002 \cdot 10^4$	$1.9002 \cdot 10^4$
Charge 2	10	$3.6931 \cdot 10^4$	$3.6931 \cdot 10^4$
Charge 2	30	$6.8000 \cdot 10^4$	$6.8000 \cdot 10^4$
Charge 2	60	$10.0097 \cdot 10^4$	$10.0097 \cdot 10^4$
Discharge 2	3	$-1.9720 \cdot 10^4$	$-1.9720 \cdot 10^4$
Discharge 2	10	$-3.7814 \cdot 10^4$	$-3.7814 \cdot 10^4$
Discharge 2	30	$-6.8935 \cdot 10^4$	$-6.8935 \cdot 10^4$
Discharge 2	60	$-10.2050 \cdot 10^4$	$-10.2050 \cdot 10^4$

Table 7.3: *List of amounts of energy for different simulations times and modes. All energy amounts in discharge mode are negative, as energy is drawn out of the system.*

As can be seen from the table, heat input equals net stored energy. It is therefore concluded, that there is energy balance in the system. It can also be seen from table 7.3 that heat transfer is variating with time. This can also be seen when looking at the heat flux in figure 7.4 where the absolute value of heat flux decreases with time. Heat flux is negative due to the direction of heat transfer, as heat is transferred from PCM to HTF.

7.4 Phase Change Model

Modelling a phase change is often referred to as a Stefan problem, which involves solving heat conduction equation with moving boundaries. In order to solve the Stefan problem, initial and boundary conditions must by specified. Neumann pre-

sented in 1912 an analytical solution to the 1D Stefan problem. Analytical solutions are, however, not available for geometries unless it is very simple. For this reason, numerical solutions are used for solving the Stefan problem (Poirier and Salcudean, 1988).
Poirier and Salcudean (1988) have considered a number of different methods for solving the Stefan problem using numerical methods. The considered methods are

- Post Iterative (isothermal) : Keeps the temperature at phase change temperature during phase change. Accummulates energy for the individual node in an energy budget. When the heat in the energy budget equals the latent heat, the phase change takes place, and the temperature is released (Dusinberre, 1945).

- Post Iterative (mushy) : This method is the same as the postiterative isothermal method except that it accounts for a mushy range. Latent heat is released linearly with temperature over a temperature range and is assumed to be a function of the temperature in that range (Dusinberre, 1945).

- Apparent Capacity : Latent heat is accounted for be increasing the heat capacity in the phase change temperature range. Heat capacities are calculated as a function of temperature (Hashemi and Sliepcevich, 1967).

- Enthalpy Method : This method is based on a certain heat conduction equation, where an enthalpy versus temperature variation is assumed (Meyer, 1973).

- Effective Capacity : An effective heat capacity is calculated based on integration through the nodal volumes and an assumed temperature profile, instead of calculating an apparent capacity based on the nodal temperature (Poirier and Salcudean, 1988).

- Tacke Method : The method is very similar to the Enthalpy Method. The only difference is the calculations of the volume element which contains the phase front (Tacke, 1985).

These methods are evaluated and compared to an analytical solution. The results of this comparison is presented in table 7.4 as the standard deviation of the test results compared to the analytical solution in a number of points.

Standard deviations	1D Iron (°C)			1D Water (°C)		
Explicit Time Step (s)	70	140	210	2000	6000	10000
Post Iterative (isothermal)	4.3	4.6	5.2	0.17	0.17	0.17
Post Iterative (mushy)	3.8	4.1	4.7	0.16	0.16	0.17
Apparent Capacity	12.5	17.2	19.0	0.32	0.60	0.65
Enthalpy Method	3.8	4.1	4.5	0.17	0.16	0.17
Effective Capacity	3.5	4.1	4.8	0.24	0.26	0.33
Tacke Method	1.4	1.8	2.3	0.021	0.017	0.03

Table 7.4: *Standard deviations for a 1D simulation of a solidifying phase change (Poirier and Salcudean, 1988).*

Poirier and Salcudean (1988) describes the different solutions. Here, the Post Iterative method by Dusinberre (1945) is described as a simple method which is easy to apply. As can be seen from table 7.4, results produced by the Post Iterative method does not differ considerably from the other methods. Therefore this method is chosen for modelling the phase change.
The method sets up an energy budget for each node in the grid. For each time step a new temperature is calculated. This temperature is set back to the phase change temperature, until heat is accumulated in order for the material to change phase (Poirier and Salcudean, 1988)[1].
Temperature for each node is calculated by equation 7.21. When the temperature crosses phase change temperature, the phase change model take effect. The working principal of the phase change model is illustrated in figure 7.5.

[1]It has not been possible to obtain access to the article by Dusinberre (1945). Therefore the description of the method is taken from Poirier and Salcudean (1988).

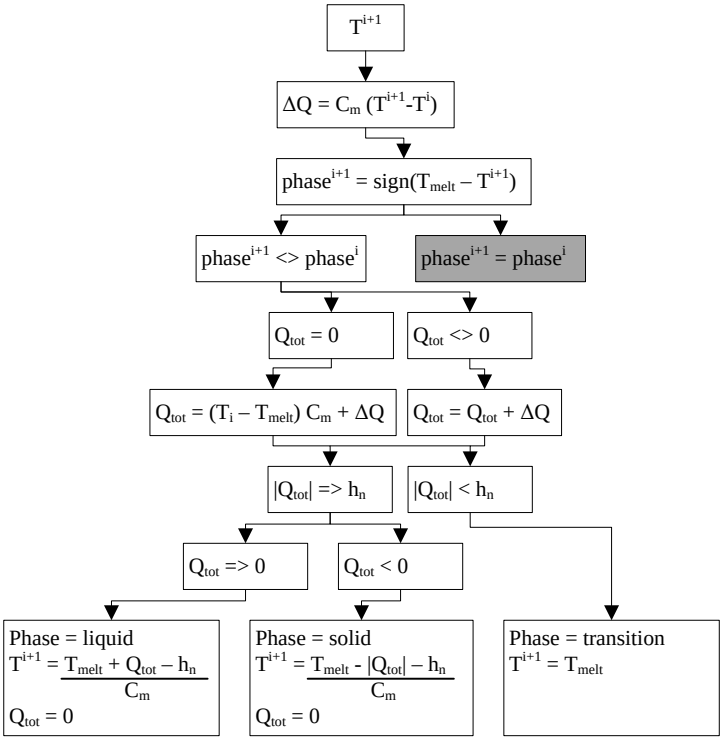

Figure 7.5: *The diagram shows how the phase change is evaluated, and how temperature is regulated according to phase change (diagram produced by the authors).*

The model starts with the new temperature T^{i+1} as calculated in equation 7.21. This temperature is calculated for each node in each time step. The new temperature is then compared to the melting temperature of the material. If T^{i+1} crosses the phase change temperature, the phase of the node changes. "i" denotes the time step. If the phase does not change, the simulation continues to next node (hence the grey filling).
If the node changes phase, it is first evaluated for accumulated energy Q_{tot}. If this is equal to zero, it means that the node have just initiated phase change. As the temperature T^i for the previous time step is different than the phase change temperature, some of the heat is used for moving from T^i to the phase change temperature. Excess heat is accumulated in Q_{tot}. If Q_{tot} is different from zero, it means that the node is already under transition, and ΔQ is added to Q_{tot}.
$|Q_{tot}|$ is then compared to the latent heat, h_n, for the given node. If $|Q_{tot}|$ is smaller than h_n, the given node is under phase transistion and the temperature is set to the phase changing temperature. If $|Q_{tot}|$ is larger than h_n, the phase change is completed, and if Q_{tot} is larger than zero, the phase is set to liquid and if Q_{tot} is smaller than zero, the phase is set to solid. In both cases, excess heat is used for changing the temperature from the phase change temperature. Q_{tot} is set to zero.

7.5 Time Step Analysis

When a simulation is run, a certain simulation time is determinded as mentioned in table 5.3. Clearly, the larger the time steps the less computation time is needed.

However, when choosing a time step to large, the solution will be inaccurate. The time step of the evaluations is given by the explicit time stability criterion (Mills, 1995) as

$$\Delta t \leq \left(\frac{C_m}{\sum_n \frac{1}{R_{mn}}} \right) \tag{7.23}$$

Equation 7.23 is to be evaluated for each node, and the time step must then be chosen accordingly to fulfillment of the criterion imposed by equation 7.23. Clearly, equation 7.23 is a function of equation 7.17 and 7.19. Furthermore, both of these equations are functions of r_m. When evaluating the functions, it becomes clear that the smaller r_m the smaller the time step. This means that the smallest time step is found from the control volumes closest to the pipe.
To ensure, that the time step found by the stability criterion in equation 7.23 does not influence the solution, a comparison is made to show the consequences of different time steps.

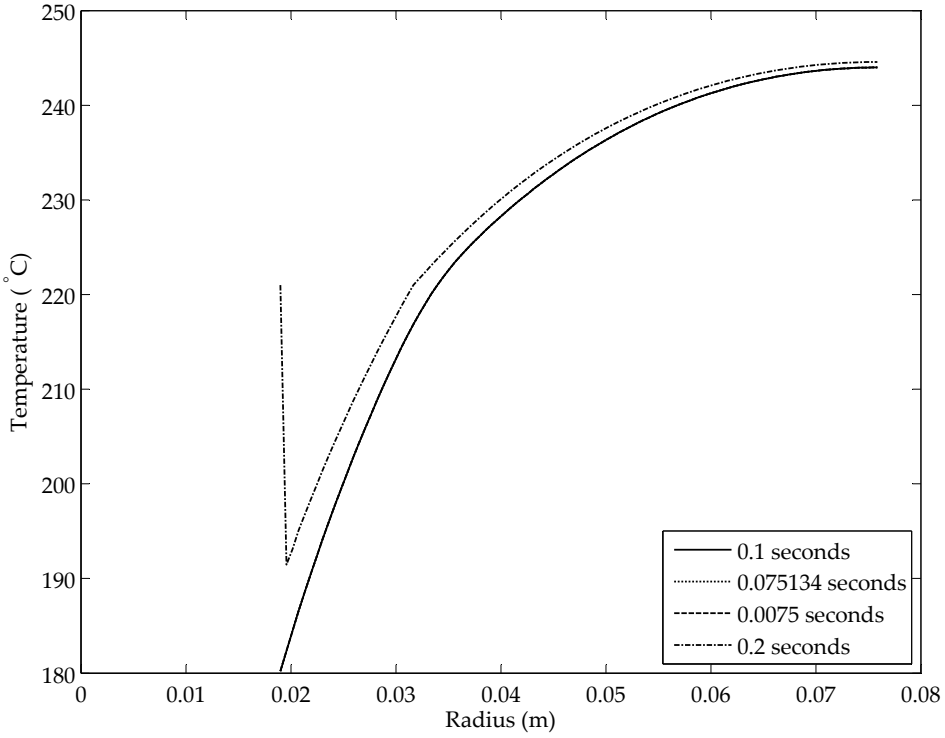

Figure 7.6: *Temperature plot of simulations with three different time steps. All have 100 nodal points in radial direction and a starting temperature of 251 °C and HFT temperature of 180° C*

Figure 7.6 is a plot of the temperature profile of a simulation with 100 nodes, initial temperature of 251°C and a HTF temperature of 180°C as in discharge 1. The time step of 0.075134 seconds is found using equation 7.23, where the time step of 0.0075 seconds is also found using equation 7.23, but then redused to an order smaller. As is clear from figure 7.6, there is no difference between these two simulations. A time step of 0.1 seconds is also presented. This time step does not show any difference,

which indicates that time steps can be slightly larger than recommended by equation 7.23. If time step is further increased, obvious indications hereof will be seen in terms of the temperature profile. Figure 7.6 also shows a simulation with a time step of 0.2 seconds, which is larger time steps than determined from the stability criterion, and as the figure clearly shows, there is a significant difference in temperature. It is therefore concluded, that the stability criterion in equation 7.23 is satisfactory.

7.6 Grid Independency Analysis

The purpose of a grid independency analysis, is to ensure, that the grid does not significantly influence the solution. As with the time step, it all depends on computation time. If computation time was not important, an almost infinitely fine grid size could be chosen. However since computation time is a factor to consider, as coarse a grid as possible is to be preferred, as it reduces computation time. A coarse grid does, however, produce a less accurate solution.
The grid independency is evaluated across the temperature profile of the model. The four different scenarios mentioned of charge and discharge mode in table 5.2 have been simulated and evaluated.

Nodes	Critical Time Step (seconds)
10	0.80
30	0.20
50	0.10
80	0.09
100	0.07
200	0.03
400	0.01

Table 7.5: *Seven different grid sizes have been evaluated. The time step is for each grid evaluated by the stability criterion in equation 7.23.*

Each grid is evaluated over four different simulation times to study if this results in a larger difference in the grids. The simulation times are 3, 10, 30 and 60 minutes as also presented in table 5.3. For each simulation time and each grid size a plot of the temperature profile is presented in figure 7.7.

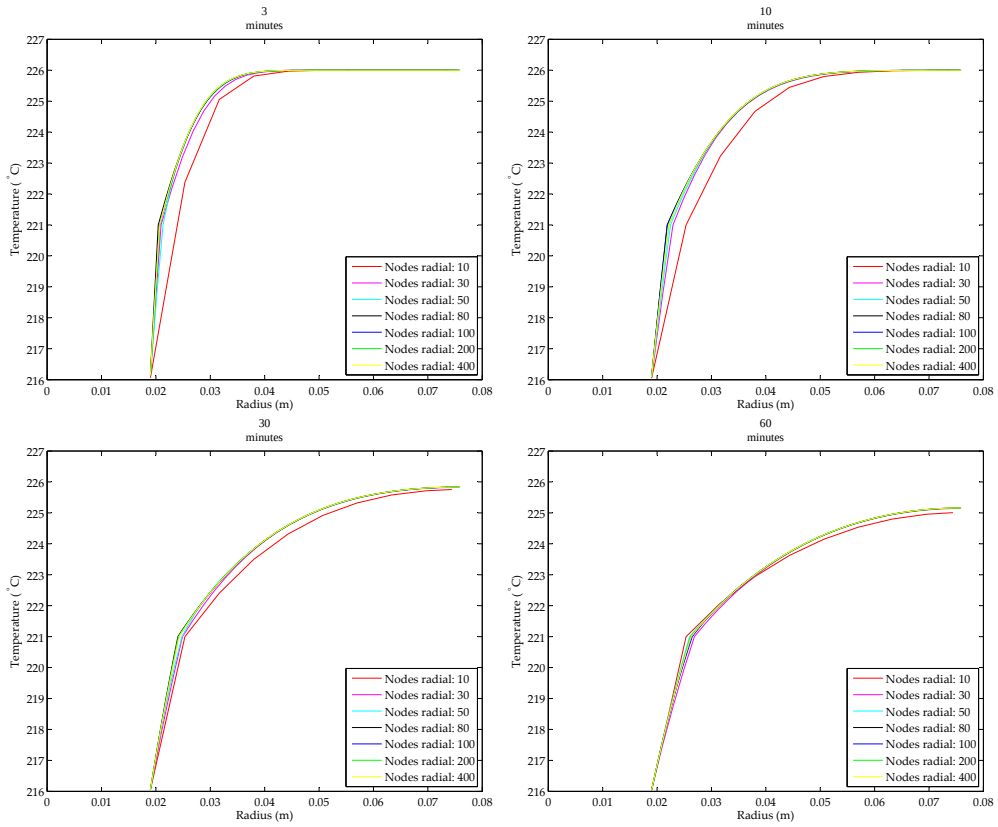

Figure 7.7: *Temperature profile of evaluated grid sizes for each simulation time.*

As figure 7.7 clearly shows, the grid size of 10 nodes is very different from the other grids. Temperature profile of 30 nodes is also a little bit different from the rest. 50 nodes seems to be very close to the higher grids. 80 nodes are chosen as the preferred grid, as this is very close to the remaining grids.

7.7 Results

Table 5.2 shows the boundary conditions for the four different simulations. With the grid size found in section 7.6 all three simulations are now computed for the four different simulation times and presented in figure 7.8.

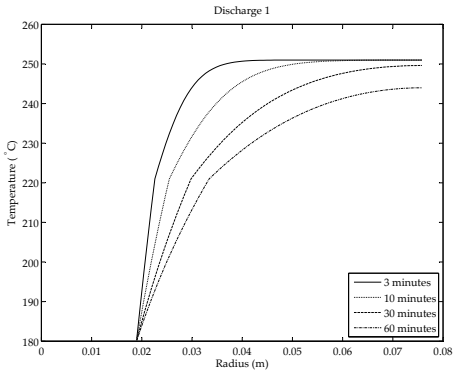

(a) *Temperature profile for simulation with 251 °C PCM as initial temperature and HTF temperature of 180 °C. Discharge mode no. 1.*

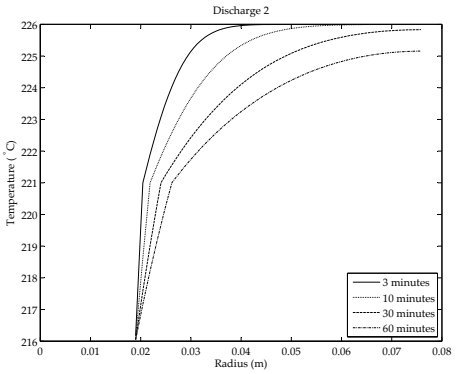

(b) *Temperature profile for simulation with 226 °C PCM as initial temperature and HTF temperature of 216 °C. Discharge mode no. 2.*

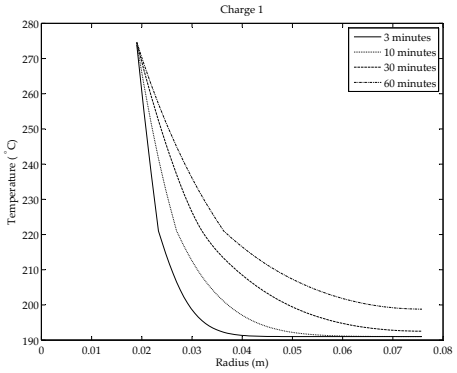

(c) *Temperature profile for simulation with 191 °C PCM as initial temperature and HTF temperature of 275 °C. Charge mode no. 1.*

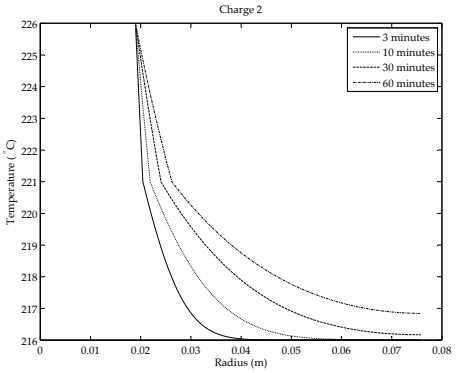

(d) *Temperature profile for simulation with 216 °C PCM as initial temperature and HTF temperature of 226 °C. Charge mode no. 2.*

Figure 7.8: *Temperature plot of four different simulation times, showing the temperature distribution in the PCM.*

All subplots of figure 7.8 show the same tendency, only from different starting and ending temperatures. All figures show a discontinuity in the profil around the melting point. This is due to the latent heat of the PCM, which absorbs heat in order to initiate the phase change. In figure 7.8b and 7.8d the discontinuity of the temperature is more distinct which again is due to the phase change. Consequently, the discontinuity can be thought of as the location of the melting front.

7.8 Computational Time

In section 7.5 it is mentioned that the size of the time steps is determining for the computation time for each simulation. Throughout the work with this numerical model, modifications have been made to the code, in order to achieve faster execution. The simulations presented in table 7.6 show how computation time have decreased significantly due to improvements of the code.

7.8.1 Pre-allocations

The model contains a large number of for-loops. Inside these loops are arrays, which increase in size for each loop run. Resizing the arrays makes MATLAB look for even larger contiguous memory blocks and the moving the array to these blocks. This is a very time consuming process, which can be avoided by pre-allocating the array. This is done by a simple command that initially fills the array of the desired size with zeros.

7.8.2 Function Inside For-Loop

During work with the model, it was realised that a function was included in the for-loop calculating the new temperature in each node. This function calculates the a part of equation 7.21. The part is shown here as equation 7.24.

$$\sum_{n} \frac{\mathrm{T}_n^i}{\mathrm{R}_{mn}} \tag{7.24}$$

As equation 7.21 is an explicit equation, all data used for calculation of the temperature in the current time step are based on temperatures from the previous time step. This means that the function does not need to be inside the for-loop and can be moved outside of this. This has a large impact on computation time, as can be seen from table 7.6.

	Computation time (index)
Function inside for-loop and no pre-allocation	100
Function inside for-loop with pre-allocation	9.00
No pre-allocation, function outside for-loop	0.30
Final model	0.06

Table 7.6: *Computation time for four different variations of the model is presented. As computation time is also depended on the computer on which the model is run, index numbers are used for showing differences in calculation time.*

The time measurement of the simulations mentioned in table 7.6 is not a very precise measurement, as the computer was running a number of other applications at the same time during measurement. It does, however, give a good indication of the significance of the code improvements. Furthermore, as seen from table 7.6, there is a large difference in computation time from the first models to the final model.
The computer used for executing the numerical model has dual core CPU. MATLAB is capable of running applications on both CPU cores. This can be done in a for-loop where two runs in the loop can be done simultaneously, provided that one loop run is independent of the previous. Unfortunately, for this model only a few small for-loops satisfy this condition. Hence, parallel computing itself does not lead to a significant decrease in execution time of this particular model.

7.9 Model Validation

To ensure coherence in both the CFD analysis and the numerical model, a comparison of the two is performed. This comparison has its origin in the temperature plot of the simulation time of 10 minutes.

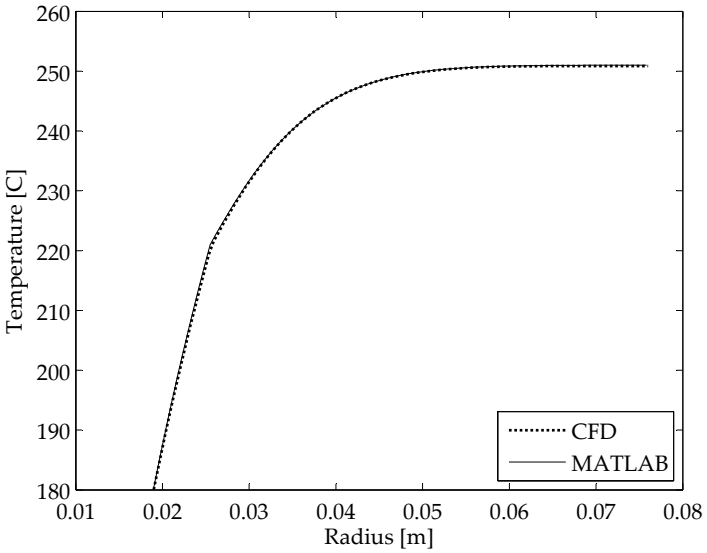

Figure 7.9: *Plot of temperature profiles from the CFD analysis and the numerical model at a simulation time of 10 minutes.*

As figure 7.9 clearly shows, the results from the two models are very close to each other. It is therefore concluded, that there is coherence between the CFD analysis and numerical model in MATLAB.

Part III

2D Study

Chapter

8

Natural Convection Contribution

As the treatment of the problem is expanded into 2D, natural convection in the liquid PCM may now become a factor to consider. If there is no convection in the liquid phase PCM, heat transfer will be by pure conduction. In natural convection heat transfer the fluid is moved around in the system driven by buoyancy differences. In order to get a clear picture of the magnitude of natural convection contribution in the liquid phase of the PCM, a number of non-dimensional figures are calculated.

8.1 Volume Expansion Coefficient

Natural convection is driven by temperature differences in the fluid. As the density of a liquid is a function of temperature, density varies along with temperature. Hence, it is convenient with a non-dimensional number for density difference as a function of temperature difference. This is found in *volume expansion coefficient* β which for constant pressure is given as

$$\beta \approx -\frac{1}{\rho_s}\frac{\rho_\infty - \rho_s}{T_\infty - T_s} \tag{8.1}$$

where ρ is the fluid density and T is the temperature. Subscripts s is at the surface and ∞ is so far away from the surface that it has no influence, respectively. β represents the fraction of volume change of a fluid relative to the temperature difference $\Delta T = T_\infty - T_s$. The flow rate of natural convection is established by the balance of buoyancy force and friction force (Çengel, 2006).

8.2 Grashof number

The ratio between buoyancy force and friction force is represented by the dimensionless Grashof number. The Grashof number controls the flow regime in natural convection and is given as

$$Gr = \frac{g\,\beta(T_s - T_\infty)L_c^3}{\nu} \tag{8.2}$$

where g is the gravitational acceleration, β is the volume expansion coefficient, L_c is the characteristic length of the geometry and ν is the kinematic viscosity of the fluid. As the Reynolds number determines whether a forced convection flow is laminar or turbulent, so does the Grashof number for natural convection (Çengel, 2006).

8.3 Prandtl number

The Prandtl number is a dimensionless figure for the relative thickness of the velocity and the thermal boundary layer and is given as

$$Pr = \frac{\mu\, c_p}{k} \tag{8.3}$$

where μ is the dynamic viscousity, c_p is the specific heat and k is the thermal conductivity.

8.4 Nusselt number

Just as with forced convection, natural convection increases heat transfer. Therefore the geometry and orientation of the surface as well as variation of temperature over the surface is determining the amount of heat transfer. With the exception of some simple cases, heat transfer relations in natural convection is primarily based on experimental studies. For most geometries empirical correlations for heat transfer by natural convection is presented in various literature. The correlations are based on the average Nusselt number and are given as

$$Nu = \frac{h\, L_c}{k} = C Ra_L^n \tag{8.4}$$

where C and n are constants based on the geometry and Ra is the Rayleigh number given as

$$Ra = GrPr \tag{8.5}$$

where Pr is the Prandtl number and Gr is the Grashof number. The average Nusselt number is the convection heat transfer relative to conduction heat transfer across a given fluid layer. The amount of heat transfer is now given as

$$\dot{Q}_{conv} = h\, A_s (T_s - T_\infty) \tag{8.6}$$

where the average heat transfer coefficient h is found by equation 8.4 (Çengel, 2006).

8.5 Evaluation of Natural Convection Present

Natural convection can only be present in the liquid part of the PCM. Hence, the temperature interval is determined by heat pipe temperature end PCM melting temperature. The evaluated geometry is the same as figure 5.1. As already determined in equation 8.1 , differences in density is a driving force in natural convection. Figure 8.1 shows the non-dimensional density of the PCM as a function of temperature in four different simulation times, depicted relative to radius.

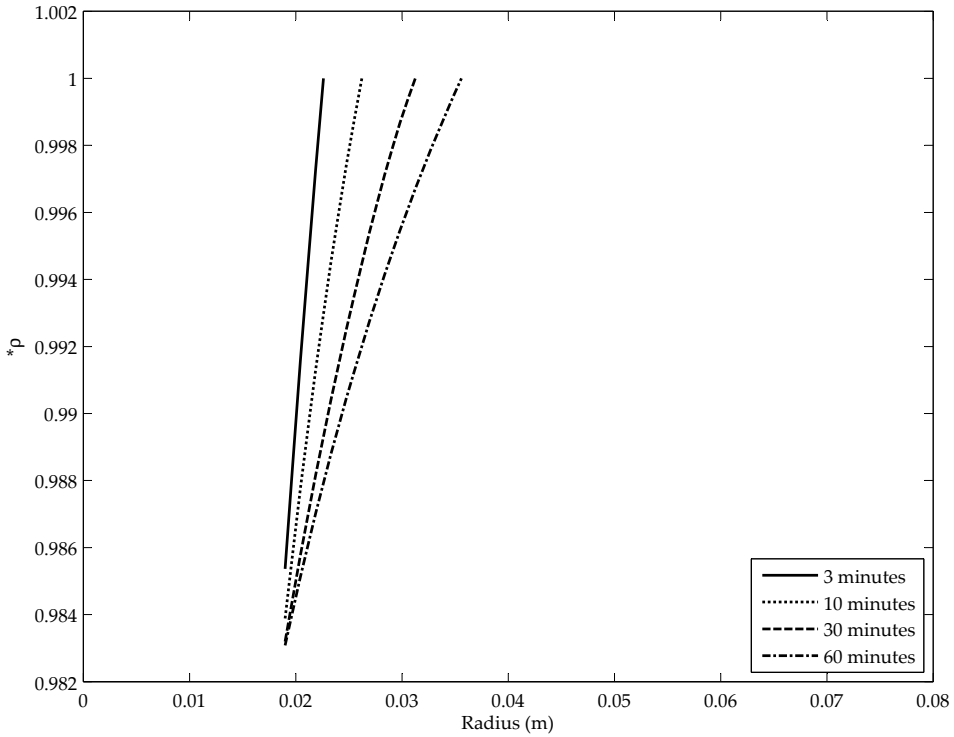

Figure 8.1: *Plot of non-dimensional density with a pipe temperature of 275° C and a PCM temperature of 221° C*

The empirical correlation for the average Nusselt number on a horizontal cylinder is

$$Nu = \left(0.6 + \frac{0.387Ra^{1/6}}{(1 + (0.559/Pr)^{9/16})^{8/27}}\right)^2 \tag{8.7}$$

Emperical correlation for a vertical cylinder can often be considered as a vertical plate. This is dependent on the cylinder diameter and the following criteria must be fulfilled:

$$D \geq \frac{35L}{Gr^{1/4}} \tag{8.8}$$

This criteria gives D $\geq$ 0.085, and as D = 0.038, the criteria is not fulfilled. Instead a correlation by VDI (2010) is used and is given as

$$f(Pr) = \left[1 + \left(\frac{0.492}{Pr}\right)^{9/16}\right]^{-16/9} \tag{8.9}$$

$$Nu_{plate} = \left(0.825 + 0.387(Ra\ f(Pr))^{1/6}\right)^2 \tag{8.10}$$

$$Nu_{cylinder} = Nu_{plate} + 0.97\,\frac{h_c}{D} \tag{8.11}$$

Equation 8.10 is valid for for both laminar and turbulent flows over a vertical plate in the range from Ra = 10^{-1} to 10^{12}. For use in heat transfer from a vertical cylinder, equation 8.11 is used, where *height* is the height of the cylinder, which is also used

as characteristic length in the vertical plate correlation, equation 8.10 and D is the cylinder diameter (VDI, 2010).
Using this equation 8.11 along with previously mentioned equations for non-dimensional numbers regarding natural convection, the following results for charge mode appear.

Material		PCM		$Water_{@100bar}$	
Temperature interval		221-275 °C		221-275 °C	
Orientation		Horizontal	Vertical	Horizontal	Vertical
β		$3.3020 \cdot 10^{-4}$	$3.3020 \cdot 10^{-4}$	0.0019	0.0019
Grashof		$1.5729 \cdot 10^{6}$	$2.8864 \cdot 10^{10}$	$3.1318 \cdot 10^{9}$	$5.7074 \cdot 10^{13}$
Prandtl		14.3267	14.3267	0.8258	0.8258
Rayleigh		$2.2534 \cdot 10^{7}$	$4.1066 \cdot 10^{11}$	$2.5863 \cdot 10^{9}$	$4.7134 \cdot 10^{13}$
Nu		47	1104	160	4016
h	(W/m^2K)	598	552	2640	2521

Table 8.1: *Non-dimensional figures for evaluation of natural convection of 1 meter heat pipe at 275° C and PCM at 221° C. Simulation is in charge mode 1.*

Material		PCM		$Water_{@100bar}$	
Temperature interval		221-226 °C		221-226 °C	
Orientation		Horizontal	Vertical	Horizontal	Vertical
β		$3.3424 \cdot 10^{-4}$	$3.3424 \cdot 10^{-4}$	0.0015	0.0015
Grashof		$1.0124 \cdot 10^{5}$	$1.8451 \cdot 10^{9}$	$1.9871 \cdot 10^{8}$	$3.6212 \cdot 10^{12}$
Prandtl		17.1295	17.1295	0.8512	0.8512
Rayleigh		$1.7343 \cdot 10^{6}$	$3.1606 \cdot 10^{10}$	$1.6914 \cdot 10^{8}$	$3.0824 \cdot 10^{12}$
Nu		22	500	68	1664
h	(W/m^2K)	278	250	1172	1086

Table 8.2: *Non-dimensional figures for evaluation of natural convection of 1 meter heat pipe at 226° C and PCM at 221° C. Simulation is in charge mode 2.*

Figures for vertical are evaluated with a characteristic length of 1 m. For comparison natural convection for both horizontal and vertical tubes are calculated for pressurised water. Water is pressurised in order to keep it in liquid phase. Rayleigh number for PCM around vertical tubes indicates that the flow is turbulent, as the transition range between laminar and turbulent flow is $10^8 \leq \mathrm{Ra} \leq 10^9$ (VDI, 2010). The resulting heat transfer coefficient, h, in tables 8.1 and 8.2 appears larger than initially expected. Due to the low difference in density at the given temperature intervals, it was expected that natural convection was insignificant. This, however, appeared not to be the case.

Chapter

9

Finned Tubes

It was seen in Part II that the poor thermal conductivity of the PCM seriously impedes rapid phase change, and that a heating surface design of smooth pipes does not seem to be feasible solution. Because of this, a strategy of extending the heat transfer surface area is pursued in the present part of the report. Furthermore, of all the possible ways to do this, some of which were mentioned in section 1.2.1, the approach of using finned tubes in the heating surface of the storage have been chosen. However, the sheer addition of material onto a pipe does not itself guarantee a significant increase in heat transfer. In order to ensure efficient use of the additional fin material, an investigation of determining a proper fin for this particular application is carried out. It is structured by first conducting a brief and narrow literature search on this specific topic to locate a suitable fin shape. This is followed up by analytical calculations to come up with the best design dimensions of the given fin shape, and finally using this in a 2D CFD analysis to investigate the interaction of the solid-liquid interface with the heating surface geometry.

9.1 Finned Surfaces in Latent Heat Storage Applications

In order to benefit from the work already made within application of finned tubes in PCM based heat storage facilities, some of the advances are reviewed in the following.

A review paper by Kenisarin and Mahkamov (2007) describes results of experimental tests of three design of finned tubes: longitudinal fins with a rectangular profile, closely spaced and thin circular fins, and a tube with a more sparse use of fins. During a five hour period with micro-encapsulated PCM slurry as storage medium, the total amount of transferred heat was evaluated compared to the performance of a plain tube. Here, the longitudinal fins showed the largest increase in heat transfer by 11.4 % and 9.7 % in charge and discharge mode, respectively. In terms of circular fins, the design with a small fin spacing raised heat transfer about 8.1 % and 5.3 % where these figures for larger fin spacing was reduced to 3.9 % and 1.3 % for charge and discharge mode, respectively. The height of both longitudinal and circular fin were about 27 mm. However, since dimensions on fin thicknesses were not provided, final conclusions regarding optimum use of the fin material are hard to make. Finally, the circular fin tube designs had 34 and 17 fins per meter pipe corresponding

to 56 and 28 mm of exposed plain tube between each fin.
DLR have conducted their own test of steel, aluminum, and expanded graphite fins with an eutectic KNO_3-$NaNO_3$ composition as PCM. In general, DLR endorse the use of fins and especially emphasises graphite as being an cost-effective material for the purpose. This is due to low density and price of the material combined with its high thermal conductivity relative to carbon steel (for material property details, please see sections 4.1.1 and 4.1.2). As shown in figure 9.1, DLR found that considerably more material is required for steel fins than for graphite fins.
Furthermore, other favourable characteristics of graphite fins are reported: *"Expanded graphite shows good chemical stability in nitrates and nitrites at temperatures up to 250 °C and galvanic corrosion does not occur in contact with steel tubes."* (Laing et al., 2009, 3) and *"The experiments did not show any degradation of the graphite foils or the PCM resulting from the charging/discharging cycles."* (Laing et al., 2009, 4).

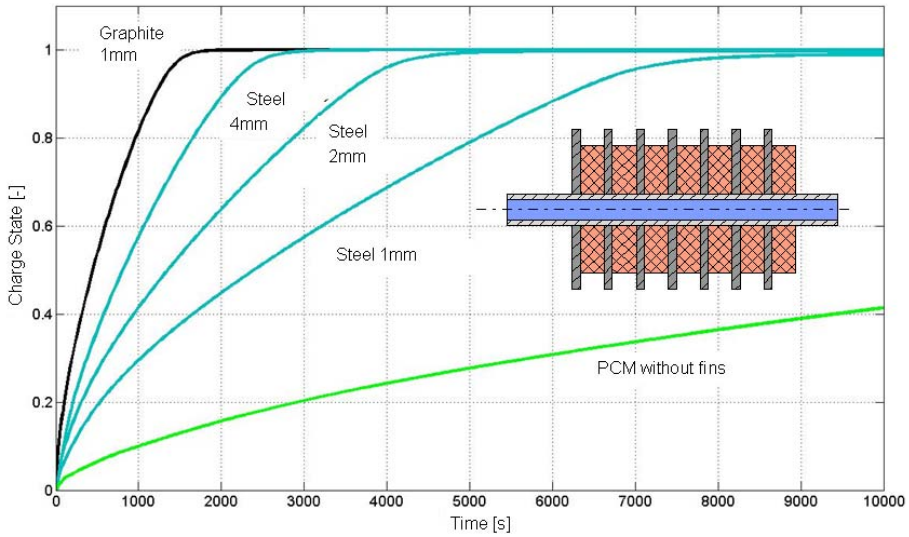

Figure 9.1: *Charge state vs. time for various fin thicknesses of steel fins compared to graphite fins and a plain tube. Taken from Laing et al. (2009).*

Expanded graphite fins were also tested within the framework of DISTOR project mentioned in section 1.2.1, which DLR also was involved in. In this connection, the most significant guidelines from this work were that fin thicknesses from 0.5 to 1 mm were used and pipe interspacing ranging from 50 to 100 mm could be used according to desired power output (Steinmann and Tamme, 2008).

9.2 Fin Efficiency

Heat transfer from a surface at an elevated temperature T_s to a surrounding medium at some lower temperature T_∞ is expressed by Newton's law of cooling:

$$Q = h\,A\,(T_s - T_\infty) \tag{9.1}$$

If, as in the present case, the amount of heat transfer is insufficient from the body surface to the surrounding PCM, the must obvious way to increase it is by increasing the heat transfer surface area A, as the temperatures are fixed by the system requirements. Moreover, an increased heat transfer coefficient h would require raised flow velocities provided for example by agitation equipment, which seem infeasible for an application that involves solid/liqiud phase change. However, increasing A by equipping the tubes with fins is not equivalent to increasing the surface area of the pipe itself. The extended fin surface is somewhat less capable of transporting heat due to a temperature difference occurring along its length (or height for *e.g.* circular fins). From the base of the fin towards the tip, the temperature T_s gradually approaches that of the external fluid T_∞ which decreases the term $(T_s - T_\infty)$ and thereby the ability to transport heat as temperature is the driving force behind all heat transfer. Consequently, geometrical limitations exists in terms of the fin design before fins are no longer economically feasible. Fins should therefore always be designed according to an acceptable fin efficiency in order to ensure high utilisation of the added fin material.
Furthermore, when compared to a smooth pipe, the heat transfer coefficient h will experience some reduction in size due to the temperature gradient along the fin length. However, A is normally increased several times by the use of fins, which justifies this method of extending the heat transfer surface area.
Based on the preceding section 9.1, a circular disk fin geometry is chosen for further studies. Furthermore, Aalborg CSP have expressed an interest in using a so-called *Sunrod* tube, which is the product name for a finned tube with steel pins radiating from the outer pipe surface. Therefore, a Sunrod tube with pins arranged orthogonally to the outer pipe surface is also considered in the following studies of extending the heat transfer surface area.
Calculations of the fin efficiency of a circular fin is done according to the method given in Brandt (1985), which will be presented in the following. This method is meant to be used in connection with finned heating surfaces in steam producing facilities *i.e.* boilers, and is therefore based on a forced convectional flow of flue gas across a tube bank. However, as the given problem involves a latent heat storage, forced convection is replaced by a weak natural convection flow and flue gas is replaced by PCM. This means that the velocity of the external flow generally is much smaller, and that the flowing fluid is characterised by properties which are quite different from those of a flue gas. Consequently, a few assumptions and estimations are made in order to apply the method to the given problem.
As for fin efficiency calculations on the Sunrod tube, a method from VDI (2010) section M1 concerning pin-shaped fins on a flat plate is used with a few modifications and assumptions (Sørensen, 2011). Heat transfer coefficients for a smooth pipe determined in the same fashion as presented in section 8.5 and an approximate relation is applied to come up with heat transfer coefficients for a finned tube.
Finally, fin efficiency is exclusively evaluated for discharge mode as this is the only mode of operation modelled in the 2D CFD analysis in chapter 10.

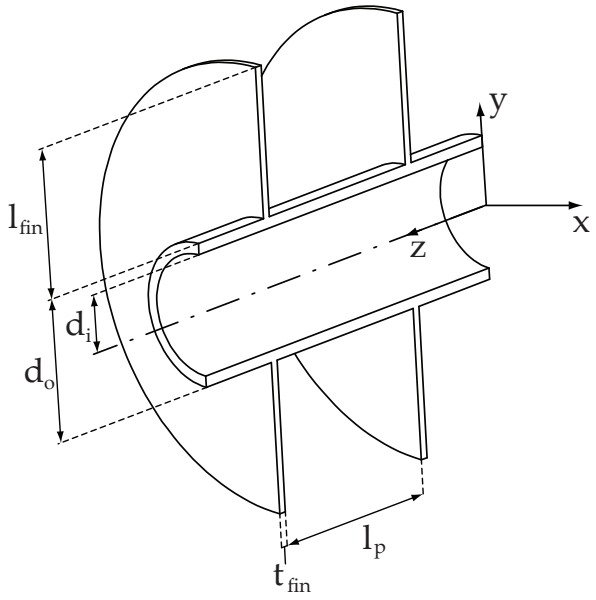

Figure 9.2: *Section cut view of a pipe with circular fins and corresponding nomenclature adopted from Brandt (1985) for pipe and fin dimensions.*

9.2.1 Efficiency of Circular Fins

Generally, own nomenclature is applied in the following calculation procedure, but in a few cases terms are adopted from the literature. The procedure of Brandt (1985) starts out by determining some geometrical definitions based on the nomenclature for pipe and fin dimensions shown in figure 9.2. Three design variables are available, namely: fin thickness (t_{fin}), fin pitch (l_p), and fin height (l_{fin}). Geometrical definitions are given in equation 9.2 for the surface area of the fin, 9.3 for fin tip area, and 9.4 for the exposed pipe surface.

$$a_{fin} = 2\pi\, Z_f\, l_{fin}\, (d_o\, l_{fin}) \tag{9.2}$$

$$a_{tip} = \pi\, Z_f\, t_{fin}\, (d_o\, 2\, l_{fin}) \tag{9.3}$$

$$a_p = \pi\, Z_f\, d_o\, (l_p - t_{fin}) \tag{9.4}$$

$$Z_f = \frac{1}{l_p + t_{fin}} \tag{9.5}$$

$$l_p = \frac{1}{Z_f} \tag{9.6}$$

Z_f expresses the number of fins per meter pipe and l_p expresses the distance between fins. In the program code developed for the purpose, Z_f is rounded off to nearest integer. Equations 9.2 to 9.4 combines to

$$a = a_{fin} + a_{tip} + a_p \tag{9.7}$$

which describes the combined area of the finned tube. From this, a characteristic length is defined as

$$l_c = \frac{a}{\pi} \tag{9.8}$$

At this point, the method prescribes calculation of the minimum flow area between the pipes A_Q, which is used together with the flue gas mass flow rate $\dot{m}$, characteristic length l_c, and dynamic viscosity μ to determine the Reynolds number Re. This is shown in 9.9 and is a merely a rewritten version of the classic formulation of the Reynolds number (eqn. 9.11) by means of equation 9.10.

$$Re = \frac{\dot{m}\, l_c}{A_Q\, \mu} \tag{9.9}$$

$$\dot{m} = \rho\, A_Q\, V \qquad \Rightarrow \qquad \frac{\dot{m}}{A_Q} = \rho\, V \tag{9.10}$$

$$\Rightarrow \; Re = \frac{\rho\, V\, l_c}{\mu} \tag{9.11}$$

The latent heat storage is basically an enclosed container with finned tubes immersed in PCM, hence there is no flow of mass across the entire tube bank as such; the only flow present are small scale natural convection flows induced locally in close vicinity of the heating surface pipes. Because of this, an estimate is made on the magnitude of the maximum velocity of the natural convection flow, and the simple correlation presented in equation 9.13 from Mills (1995) is used for this purpose. It is based on the natural convection phenomenon of a heated vertical plate, where the motion of a fluid particle along a streamline is observed. Due to the density change of the fluid, the particle will start to move upwards. If viscous forces are neglected, the gain in kinetic energy of the particle can roughly be related to the work done by the buoyancy force due to change of fluid density. This is expressed in equation 9.12 where the characteristic length l_c is the height of the vertical plate (Mills, 1995). However, the assumption of neglectable viscosity is only acceptable in case of low Prandtl number fluids, and since the PCM Prandtl number is ∼15 some error will be introduced in this regard. Nonetheless, in lack of any better analytical method to estimate the velocity of the natural convection flow, this method is applied and a Reynolds number is calculated by 9.11.

$$\frac{1}{2}\, \rho\, V^2 \approx g\, \Delta\rho\, l_c \tag{9.12}$$

$$\Rightarrow \; V \approx \left(\frac{\Delta\rho}{\rho}\, g\, l_c \right)^{1/2} \tag{9.13}$$

The values of V comes to 0.06 and 0.08 $^m/_s$ for discharge and charge modes, respectively. As only discharge mode is considered in this chapter, $V = 0.06$ $^m/_s$ is used in the calculations.

The next step is to determine a heat transfer coefficient for the fin h_{fin}, through a power-law relation for the Nusselt number of the external flow:

$$Nu = C\, Re^{5/8}\, Pr^{1/3} \tag{9.14}$$

$$Nu = \frac{h_{fin}\, l_c}{k} \qquad \Rightarrow \qquad h_{fin} = \frac{Nu\, k}{l_c} \tag{9.15}$$

where k is the thermal conductivity of the external fluid. The geometry constant C is given as 0.3 for *in-line* tube configuration while it assumes the value of 0.45 for *staggered* tubes banks.
Before the actual fin efficiency η_{fin} can be computed, a few ratios are defined

$$f_1 = \sqrt{\frac{2\,h_{fin}}{t_{fin}\,k_{fin}}}\,l_{fin} \tag{9.16}$$

$$f_2 = \frac{l_{fin}}{d_o} \tag{9.17}$$

$$f_3 = \frac{t_{fin}}{l_{fin}}\,\frac{h_{tip}}{h_{fin}} \approx \frac{t_{fin}}{l_{fin}} \tag{9.18}$$

$$x_0 = \frac{f_1}{2\,f_2} = \sqrt{\frac{2\,h_{fin}}{t_{fin}\,k_{fin}}}\,\frac{d_o}{2} \tag{9.19}$$

$$x_1 = x_0 + f_1 = \sqrt{\frac{2\,h_{fin}}{t_{fin}\,k_{fin}}}\,\left(\frac{d_o}{2} + l_{fin}\right) \tag{9.20}$$

Here, k_{fin} is the thermal conductivity of the fin material. Equations 9.16 to 9.18 are used together with the modified Bessel functions K^* and I^*:

$$K^* = K_1(x_1) - \frac{1}{2}\,f_1\,f_3\,K_0(x_1) \tag{9.21}$$

$$I^* = I_1(x_1) - \frac{1}{2}\,f_1\,f_3\,I_0(x_1) \tag{9.22}$$

Finally, the fin efficiency is given by

$$\eta_{fin} = \frac{1}{f_1\,(1 + f_2 + f_2\,f_3 + 1/2\,f_3)}\,\frac{I^*\,K_1(x_0) - K^*\,I_1(x_0)}{I^*\,K_0(x_0) + K^*\,I_0(x_0)} \tag{9.23}$$

Furthermore, an outer heat transfer coefficient corrected with the fin efficiency η_{fin} can be calculated for the finned tube by

$$h_a = \frac{h_p\,a_p + \eta_{fin}\,h_{fin}(a_{fin} + a_{tip})}{a} \tag{9.24}$$

The heat transfer coefficient of the pipe h_p can be replaced by that of the fin h_{fin} in the case that the area of the exposed pipe is significantly smaller than the fin surface area.

Thermophysical PCM Properties

The thermophysical properties used for the circular fin calculations are based on the property functions presented in section 4.1.5. The PCM temperature only appears in the equation array from 9.2 to 9.24 in connection with evaluating thermal properties and specific temperatures on the fin surface. It is not explicitly involved in the calculation of the fin efficiency, and initial studies showed that a larger temperature range in this regard could be simplified to a mean temperature with reasonable

accuracy. Though the operational mode of discharge 1 is considered in the present, basing the properties on the mean temperature of the entire span is meaningless as the PCM appears as a solid in the range 221 to 180 °C. Because of this, properties are evaluated at the mean temperature of the liquid PCM range; $(221+251)/2 = 263\,°C$.

Property	Value	Unit
μ	$5.2 \cdot 10^{-3}$	Pa · s
ρ	1940	$\frac{kg}{m^3}$
Pr	15.64	

Table 9.1: *Thermophysical properties used for fin efficiency calculations. The properties are evaluated for the mean liquid temperature of discharge mode 1; 236 °C.*

Materials and Geometry

Based on the above discussion and section 9.1, values for the three design variables; fin thickness (t_{fin}), fin pitch (l_p), and fin height (l_{fin}), are chosen presented in 9.25 to 9.27. Values of the thickness variable t_{fin} are inspired by those presented in figure 9.1 by Laing et al. (2009).

$$t_{fin} = [1, 2, 3] \quad (mm) \tag{9.25}$$

$$l_p = [10, 20, 30, 40] \quad (mm) \tag{9.26}$$

$$l_{fin} = [15, 25, 35, 45] \quad (mm) \tag{9.27}$$

Furthermore, calculations are made with both steel St.35.8 and expanded graphite as fin material. Results of fin efficiencies based on the procedure presented in the above are showed in figures 9.3b to 9.4b. Plots of 1 mm steel fins along with 3 mm graphite fins are placed in appendix E.

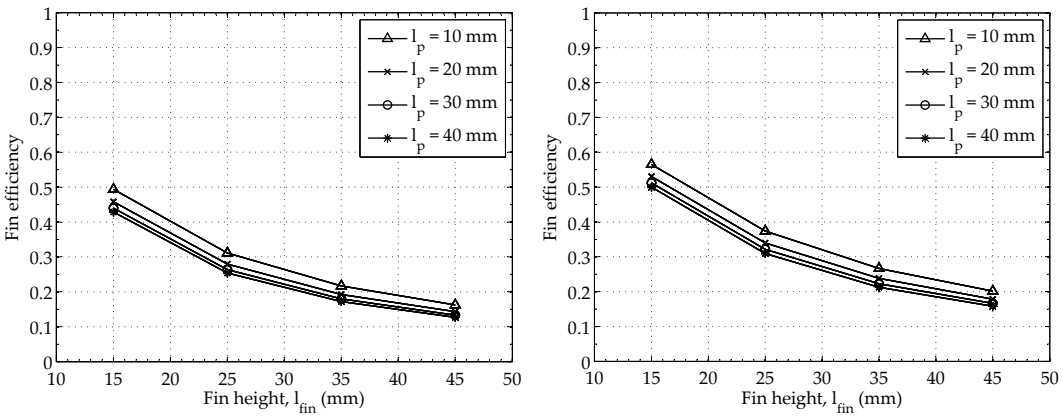

(a) *Circular steel fin, 2 mm in thickness.* **(b)** *Circular steel fin, 3 mm thickness.*

Figure 9.3: *Efficiency of circular steel fins vs. fin height and pitch l_p, discharge mode 1.*

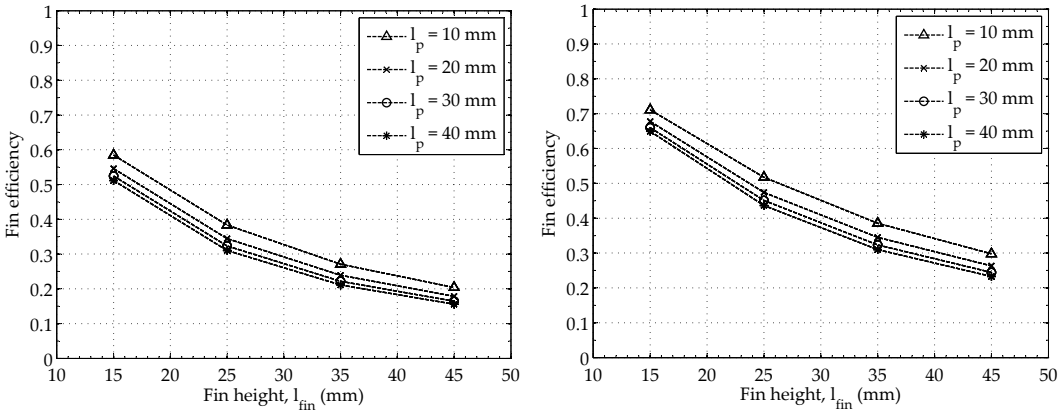

(a) *Circular graphite fin, 1 mm in thickness.* **(b)** *Circular graphite fin, 2 mm thickness.*

Figure 9.4: *Efficiency of circular graphite fins vs. fin height and pitch l_p, discharge mode 1.*

9.2.2 Efficiency of the Sunrod Tube

Regarding analytical calculations of the efficiency of Sunrod pins, a rough approach is used. First, heat transfer coefficients calculated for a plain tube based on the method mentioned in section 8.5 and evaluated in discharge modes 1 and 2 comes to 485.75 and 278.23 $^{W}/_{m^2K}$, respectively. Now, as a rule of thumb, a practical engineering relation regarding finned surfaces estimates the heat transfer coefficient by the velocity in the narrowest space between the pipes

$$h_{smoothpipe} = 20\sqrt{V} \tag{9.28}$$

$$h_{finnedtube} = 12.5\sqrt{V} \tag{9.29}$$

where the lower value of h for finned tubes is clearly expressed in the coefficient which is reduced about 37.5 % (Condra, 2011). As a rough estimation of the heat transfer coefficient for finned surfaces, the figures mentioned above are reduced by this percentage. It should be noted that equations 9.28 and 9.29 are based on fluids with Pr ≈ 1 (gasses).

According to fig 9.5, the pin length is defined as l_{fin} and pin diameter is given as t_{fin}. For now, it is assumed that each disc of pins contains 12 pins based on a Sunrod product sample from Aalborg CSP. The pipe dimensions are assumed fixed as it was the case with the circular fins. The method from VDI (2010) does not deal with the longitudinal distance between pins l_p, however, even though this parameter is not a part of the equation array, values identical to those of circular fins given in equation 9.26 are assumed for the sake of comparison. Of course, this does not change the fact that the method is based on a single pin and neglects the effects of neighbouring pins.
From this point on, the method for calculating efficiency of pin on a flat plate is

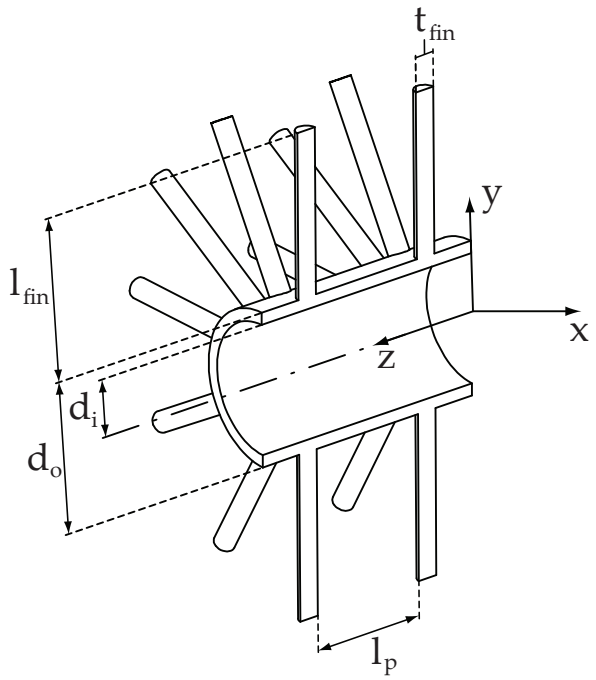

Figure 9.5: *Section cut view of the Sunrod tube and corresponding nomenclature for pipe and fin dimensions.*

applied. The geometrical parameter δ is initially defined:

$$\delta = \frac{1}{2} t_{fin} \tag{9.30}$$

Then, the efficiency of the pin geometry η_f is given as

$$\eta_f = \frac{\tanh X}{X} \tag{9.31}$$

where

$$X = \sqrt{\frac{2\,h_m}{k_{fin}\,\delta}} \tag{9.32}$$

h_m is a uniform heat transfer coefficient which is replaced by the adjusted values of heat transfer coefficients, and k_{fin} is the thermal conductivity of the fin material which is taken to be steel St.35.8.
Values chosen for the two design variables; pin diameter t_{fin} and pin length l_{fin}, are presented in 9.33 and 9.34. Results of the efficiencies if pins of varying length and diameter are presented in figure 9.6. If pin diameter and length are combined to a volume and depicted against the efficiency of the pins, it might be easier to determine which geometry is the best choice. This is done in figure 9.7.

$$t_{fin} = [2, 3, 4, 5, 6, 7] \quad (mm) \tag{9.33}$$

$$l_{fin} = [20, 25, 30, 35, 40, 45, 50] \quad (mm) \tag{9.34}$$

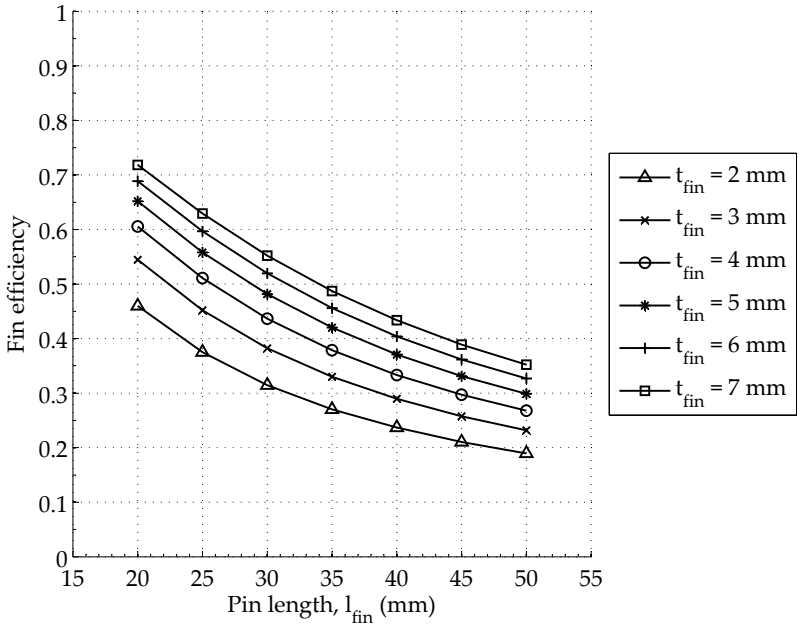

Figure 9.6: *Efficiency of pins on the Sunrod tube as a function of pin length and diameter.*

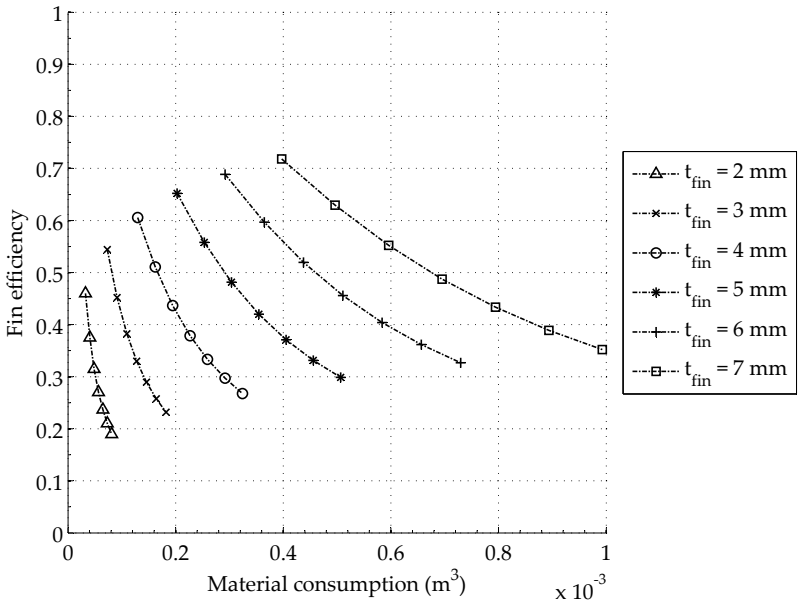

Figure 9.7: *Volume of fin material vs. fin efficiency for the Sunrod tube.*

9.3 Finned Tube Material Consumption and Design Selection

The purpose of the fin efficiency studies was to form a basis for design selection of circular fins and pins for further studies in the 2D CFD analysis in chapter 10. As a preliminary selection of designs, two possible solutions are selected for each type of fin; one based on high efficiency and one being a more economic design *i.e.* a trade-off between efficiency and consumption of fin material. Based on this, the following designs and materials are selected as shown in tables 9.2 and 9.3.

The value of fin pitch l_p is equal for all designs, and its size is estimated from solidification rates. The objective in this regard is that the cavity between the fins should be entirely replaced by solid PCM under 1 hour of discharge. From figures 9.3b and 9.4b is it seen that the size of l_p affects the efficiency the most at its lowest value of 10 mm, while only posing a minor effect at larger values. In terms of the solidification rate it is observed from figure 6.12 that solid front has progressed 17 mm in the radial direction during 1 hour. Due to the efficiency of fins, it is estimated that solidification rate in longitudinal direction will be somewhat slower than the rate in radial direction. Therefore, the fin pitch l_p is chosen to 20 mm for all designs considered.

Proposed circular fins

Material	t_{fin}	l_p	l_{fin}	Unit
Steel St.35.8	2	20	[15, 20]	mm
Steel St.35.8	3	20	[15, 20, 25]	mm
Expanded graphite	1	20	[15, 20]	mm
Expanded graphite	2	20	[15, 20, 25, 30]	mm

Table 9.2: *Specific circular fin design preliminary chosen on the basis of efficiency.*

Sunrod

Material	t_{fin}	l_p	l_{fin}	Unit
Steel St.35.8	5	20	[20, 25, 30, 35]	mm
Steel St.35.8	7	20	[20, 25, 30, 35]	mm

Table 9.3: *Sunrod tube design chosen on the basis of efficiency.*

Before the final fin designs are selected for closer studies through a CFD analysis, the volumetric consumption of fin material of preliminary design is evaluated. This is done in order to examine whether increased fin volume is proportional to the increase in fin efficiency and thereby whether it can be justified to pursue this in a design process. Figure 9.8 shows the volumetric material use for the selected fins per meter of pipe and table 9.4 shows estimated prices of the materials. The material used for the pipe itself is assumed constant for all cases, and therefore not involved in these considerations. Furthermore, it is assumed that short fins/pins will result in smaller spacing between pipes in the heating surface and thereby increasing the specific number of pipes. The objective is to maintain the fin/pin length at some intermediate level where both acceptable efficiency and material use are achieved. The final selection of fin designs for further studies are presented in table 9.5.

Circular Steel Fins

In general, the efficiencies of the steel fins proved to be quite poor, and from an economic point of view their existence are hard to justify if figures 9.3a and 9.3b are considered. Before a somewhat reasonable efficiency can be reached, the fin thickness must be increased to 3 mm. Even though the efficiency is poor at moderate and large

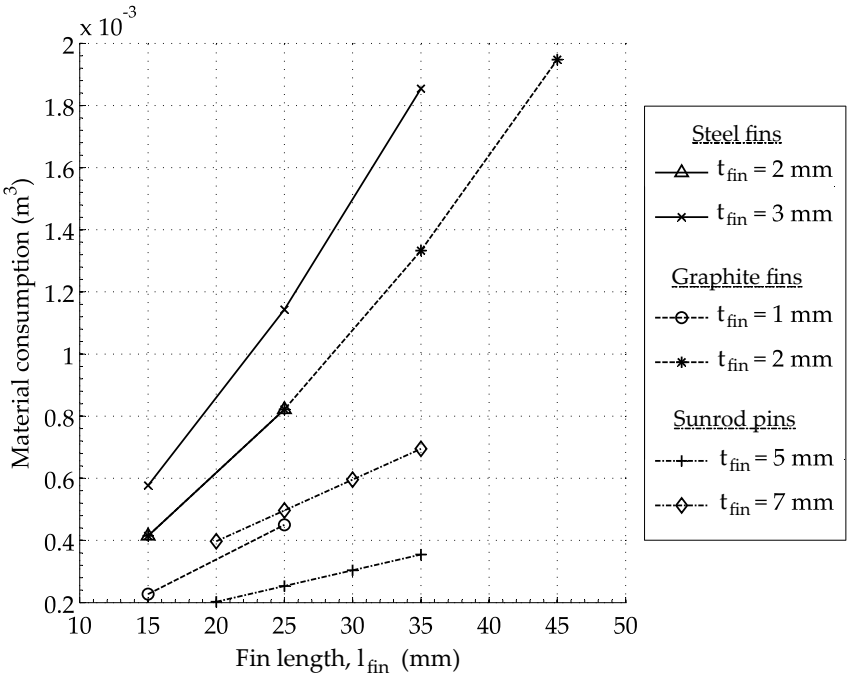

Figure 9.8: *Volumetric material use for the selected fins per meter of pipe.*

Fin material prices

Material	Density	Unit	Vol. spec. cost	Unit
Carbon Steel	7850	kg/m^3	15000	$\$/m^3$
Expanded graphite	1000		10000	

Table 9.4: *Estimated prices on fin material on a volume basis. Extracted from Laing et al. (2009)*

fin heights, the choice is made of having a fin height of 25 mm in order to keep the total number of pipes in the heating surface at a reasonable level.

Circular Graphite Fins

When comparing figures 9.4a and 9.4b, there is a considerable gain in efficiency from 1 mm to 2 mm in thickness. Furthermore, a 2 mm can be chosen with only a moderate increase of material consumption as shown in figure 9.8. Acceptable efficiency can still be reached with a fin height of 25 mm, which is the reason for choosing this dimension for the circular graphite fin.

Sunrod Steel Pins

The pin diameter of 5 mm selected based on the relative small increase in efficiency from 5 to 7 mm seen in figure 9.6 is associated with a relative large consumption of material, which can be seen from figure 9.7. Due to increased thickness of the pins compared to the thickness of circular fins, the larger length of pins can generally be

justified when comparing to the circular fin type. Therefore, the pin length is chosen to be 30 mm.

Selected fin designs

Material	Type	t_{fin}	l_p	l_{fin}	Unit
Steel St.35.8	Circular	3	20	25	mm
Expanded graphite	Circular	2	20	25	mm
Steel St.35.8	Pins	5	20	30	mm

Table 9.5: *Final fin designs selected for further CFD based studies.*

Finally, the outer heat transfer coefficients h_a calculated in equation 9.24 during the evaluation of fin efficiency of circular fins are presented in table 9.6. These figures are, as expected, lower than that of a smooth pipe as presented in section 9.2.2 (485.75 $^{W}/_{m^2K}$).

Heat transfer coefficients

Material	Type	h_a	Unit
Steel St.35.8	Circular	253.7	$^{W}/_{m^2K}$
Expanded graphite	Circular	312.5	

Table 9.6: *Outer heat transfer coefficient h_a of selected circular fin designs.*

Chapter

10

2D CFD Analysis

In continuation of the quasi-1D CFD analysis in section 6.3, the 2D part of the CFD study starts out by considering solidification around a smooth pipe. In contrast to the quasi-1D CFD study, the present analysis includes 2D convectional flow effects induced by density differences occurring locally in the melt, which will, as presented in the following, cause a different behaviour of the solidification process. All real flows governed by buoyancy forces are indeed affected by the gravitational pull of the Earth, which is why an gravitational acceleration of -9.82 $^{m}/_{s^2}$ acting in the y-axis direction is implemented in all simulation cases. Furthermore, the temperature dependent thermophysical properties described in section 4.1.5 are applied. Both modes of discharge are considered, and boundary conditions correspond to those presented in table 5.2. Due to time constraints, simulations involving simulation times of 60 minutes have been granted the main focus in the following.

10.1 2D Simulation of Smooth Vertical Pipe

The grid used to study the solidification around a smooth pipe during discharge modes 1 and 2 is presented in figure 10.1. As before, a cross-sectional area in the close vicinity of a vertical smooth pipe is considered. Only the right half of the area is selected as the computational domain due to the assumption that 2D effects on both sides of the pipe will be identical. Another difference from the previous study lies in the rectangularly shaped domain as opposed to the annular space between two concentric circles. In the latter design, a constant temperature[1] at the outer PCM *wall* type boundary (outer circle) was specified, and even though this boundary is placed far from the inner boundary, it might not be the best representation of the real problem. A workaround of this limitation is attempted in the present grid design by constructing a rectangular grid with all outer edges being of the *symmetric* type. The dimensions of the grid correspond to the pipe dimensions given in table 5.1.

10.1.1 Grid Independence and Quality of 2D Smooth Pipe Grid

Figures concerning the grid size and quality are presented in table 10.1. As a further explanation of column three of this table, the number of cells specified here refers to the cells along the dashed line on the x-axis in figure 10.1.
A significant change in terms of grid quality, is for instance the increase of the angular

[1] The initial liquid PCM temperature, actually.

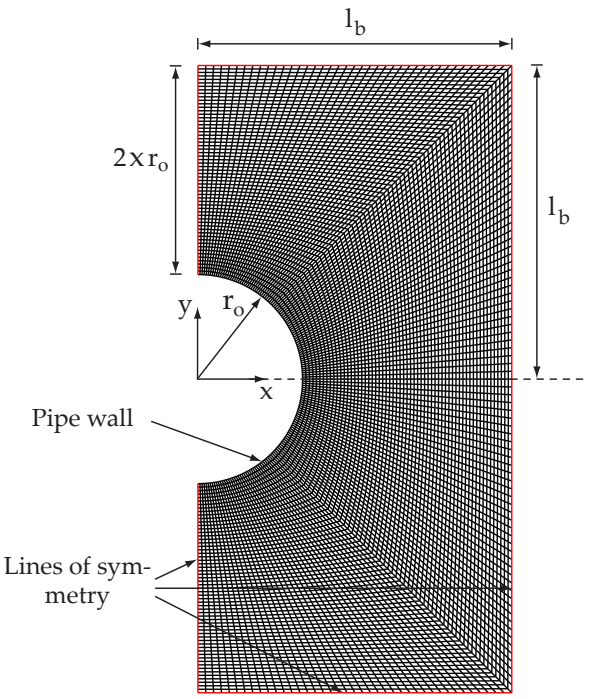

Figure 10.1: *Grid and geometrical ratios of the 2D smooth vertical pipe computational domain.*

skewness of cells, Q_{EAS}. This distortion of the cells occurs due to grid lines radiating from the curved outer surface of the pipe being merged to the straight lines of the outer boundaries of the domain. The highest values of Q_{EAS} correspond to cells adjacent to +/- 45° angle lines from the origin.

Index	No. of cells, tot. domain	No. of cells, x-axis	Angular skewness Q_{EAS}	Size change Q_{SC}	Aspect ratio Q_{AR}
24	960	24	0 - 0.51	0.99 - 1.34	1 - 2.52
100	4000	40	0 - 0.51	0.99 - 1.07	1 - 2.6
240	9600	60	0 - 0.5	0.99 - 1.05	1 - 2.76

Table 10.1: *Grid size details and characteristic numbers for the grid qualities of the three grids considered for the 2D smooth pipe grid.*

The grid's effect on the solution are evaluated by the same means as presented earlier in this report; namely by comparing the temperature profile along some predefined line in the computational domain. Here, this is done along the dashed vertical line on the x-axis in figure 10.1 and the results hereof are provided in figure 10.2. From this, some minor variation is seen. However, surprisingly the line of the coarsest grid lies between the lines of the significantly denser grids. Though the differences may be small in terms of temperature along a given line, there are major differences in terms of resolution and shape of the solid-liquid moving front, as presented in figure 10.3a to 10.3c. Because of this, Grid 240 is selected as the grid to be used for simulations. Furthermore, this example showed that the method of selecting a grid purely on the basis of a temperature profile along a straight line, may not always be

the optimal approach.

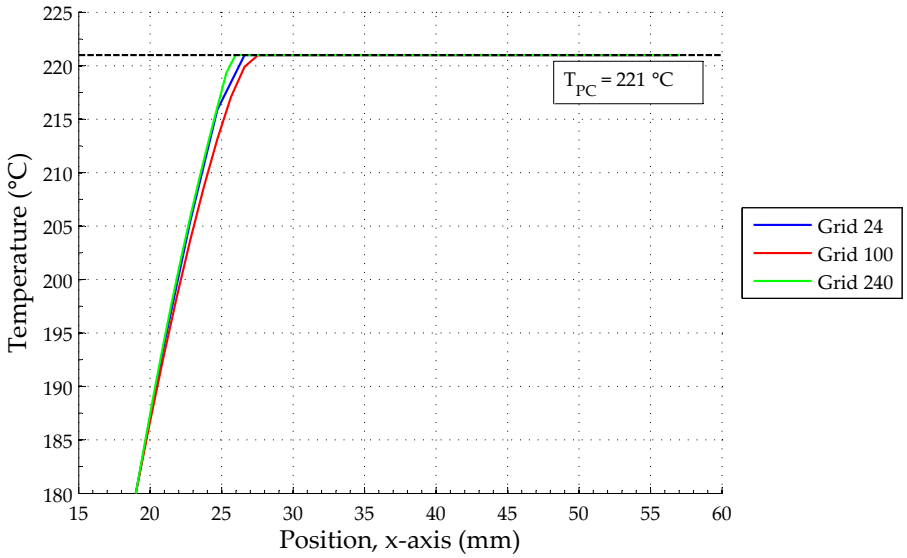

Figure 10.2: *Temperature profiles along the x-axis of the domain cf. figure 10.2 for the three grids of the grid independence study. Shown for discharge mode 1, 10 minutes.*

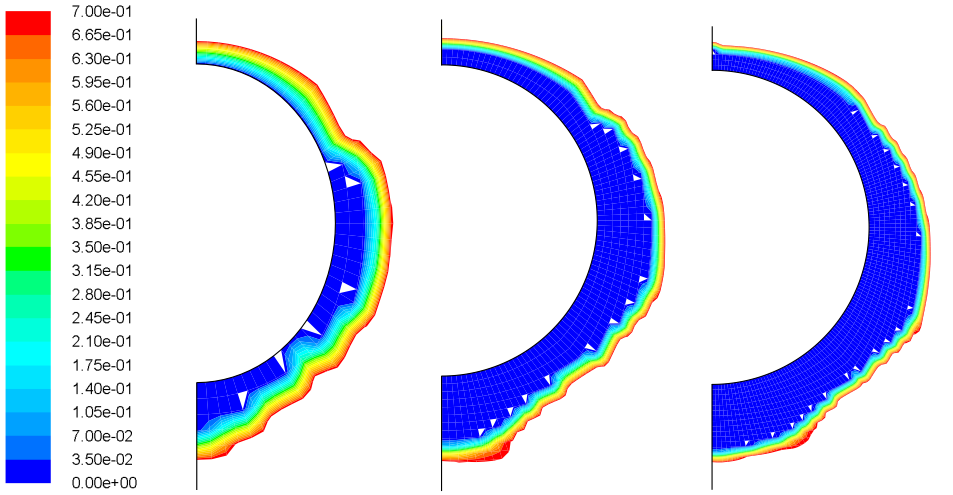

(a) *Interface of Grid 24.*

(b) *Interface of Grid 100.*

(c) *Interface of Grid 240.*

Figure 10.3: *Solid-liquid interface of grids 24, 100, and 240. Included are all cells with liquid fraction from 0 to 0.7. Discharge mode 1, 10 minutes elapsed time. Note that the white triangles are merely graphical errors without connection to the solution.*

10.1.2 Results of the 2D Smooth Vertical Pipe Simulation

CFD simulations are carried out by first computing four time steps of the solution with a time step size of 0.5 s and subsequently reducing this to 0.1 s for the remaining solution. Moreover, the maximum allowable number of iterations for the first four time steps is set to 35, and usually the residuals come close to convergence by the

last iteration. The advantage arises when remaining time steps are computed, which experience faster convergence than if the same time step size is used throughout the solution. This was found to be an acceptable trade-off between a large time step size and number of iterations required to meet convergence criteria, which proved overall to be the most time-economical choice of parameters. Furthermore, the simulations were done with the First Order upwind discretisation scheme. Contour plots of temperature and liquid fraction for both modes of discharge and for a simulation time of 60 minutes are presented in figures 10.5a to 10.6b.
The results of the study indicate that two distinct phenomena occur within the time frame of the simulation from zero to 60 minutes. The first of these is short-lived as it dominates the heat transfer in the initial minutes before it dies out in less than 10 minutes of elapsed time. In this period, natural convection driven flows circulate PCM in the bottom half of the domain, and hereby eventually causes an even distribution of temperature in this zone. Apparently due to momentum diffusion, the circulating motion does not significantly affect the upper half of the domain, which causes stratification of temperatures in the y-axis direction.

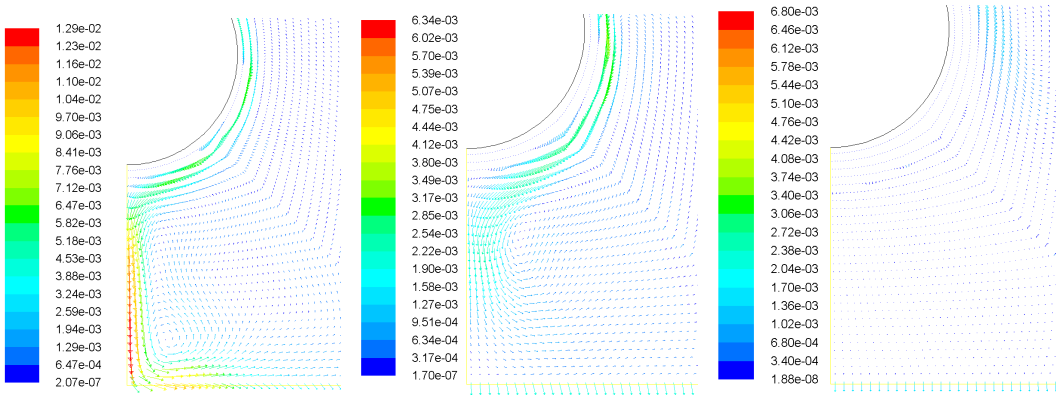

(a) *2 minutes.* **(b)** *4.5 minutes.* **(c)** *7 minutes.*

Figure 10.4: *Velocity vector plot of the start-up behaviour shown for 2, 4.5 , and 7 minutes. Note the scale is presented in $^{m}/_{s}$. Discharge mode 1.*

After a few minutes, the temperature in the bottom half zone approaches the PCM phase change temperature where it remains until the PCM is solidified. Consequently, the circulating motion comes to a halt as the temperature and thus the density is close to uniform across the region, and the natural convection dominated heat transfer comes to an end. This behaviour may be seen from the velocity vector field plots provided for 2, 4.5, and 7 minutes in figures 10.4a to 10.4c. This first period is characterised by the extraction of the PCM's sensible heat, and therefore only minor solidification is taking place in this phase of the process.
At the end of the first period, the PCM is approximately stationary and its sensible heat in the bottom half zone is reduced to the level at which phase change can be initiated. This is already seen after 10 minutes *e.g.* in figure 10.2 or even by 7 minutes in figure 10.4c. Beyond this point, conduction is responsible for the extraction

of (latent) heat from the PCM with considerable solidification as a result.
In this second period, temperatures remain stratified (see figures 10.5a and 10.5b), which, at least for discharge 1, causes the main part of the solidification to happen in the bottom half of the domain. Furthermore, the differences in ΔT from one mode of discharge to the other (temperatures are provided in table 5.2) seem to have an effect on the rate of solidification when comparing figures 10.6a and 10.6b. Regarding the above mentioned plots, the scale of liquid fraction is the same in both cases (between 0 and 1), which is the reason for only presenting it for figure 10.6a.

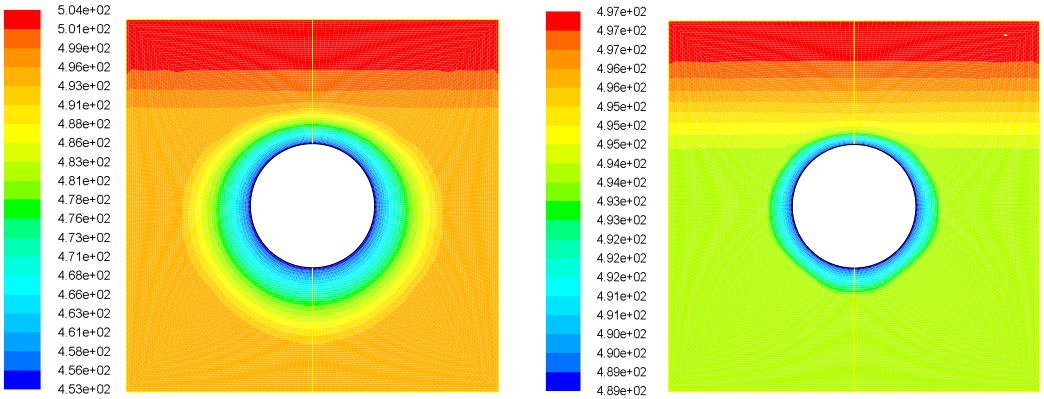

(a) *Discharge mode 1.* **(b)** *Discharge mode 2.*

Figure 10.5: *Temperature contours of both modes of discharge after 60 minutes elapsed time. Graphics are produced by reflection around the y-axis (see figure 10.1). Note temperature scales are presented in K.*

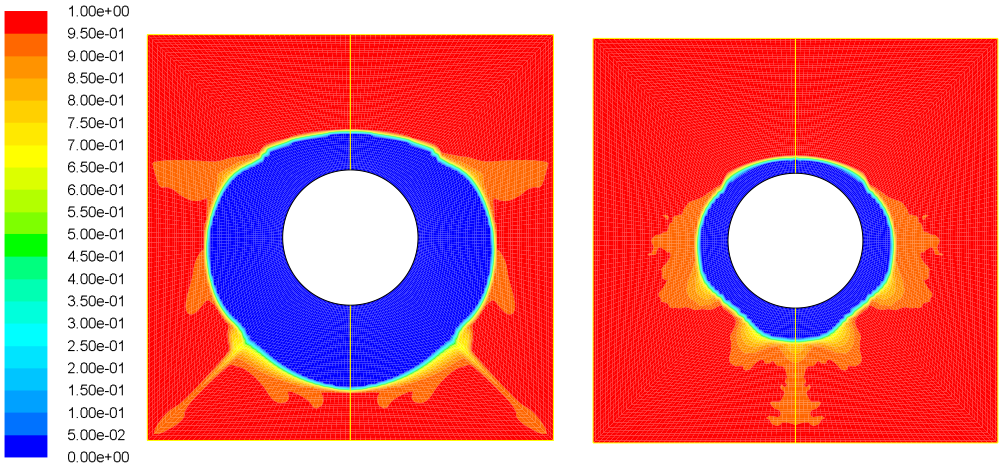

(a) *Discharge mode 1.* **(b)** *Discharge mode 2.*

Figure 10.6: *Contours of liquid fraction for discharge modes 1 and 2 after 60 minutes simulation time. Graphics are reflected with respect to the y-axis (see figure 10.1).*

The temperature stratification could be connected to the shape of the computational domain. If a heating surface consisting of smooth pipes is considered, then the fluid

density changes would not be restricted to the local area around a given pipe, but cause PCM of increasing density to move downwards past several rows of pipes placed on top of each other. This can be imitated in the CFD software by applying a pair of so-called *periodic boundaries* to the domain, which allows outflow across one boundary to be the inflow across the other. The flow of flue gas across a tube bank can for example be modelled by selecting a representative domain and apply periodic boundary conditions due to the repeating nature of the flow field. However, either the pressure drop across the tube bank or the mass flow rate of flue gas is usually known in advance in this case. The present problem, on the other hand, differs considerably from the tube bank example by having a pressure drop that is practically zero and a small and time dependent mass flow rate across boundaries. Consequently, applying periodic conditions to the top and bottom boundaries of the present domain did not yield results with any physical meaning, unfortunately.

10.2 2D Simulation of Circular Annular Finned Tube

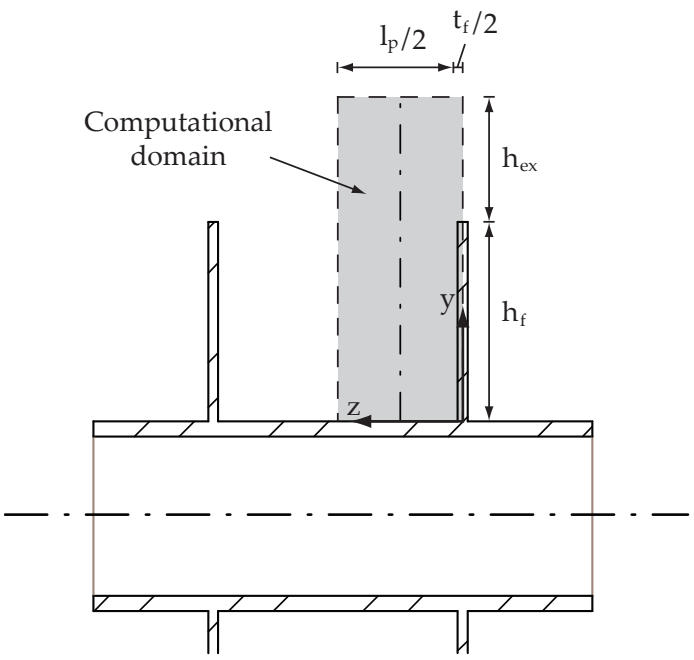

(a) *Sketch of the longitudinal section cut view of a circular finned tube.*

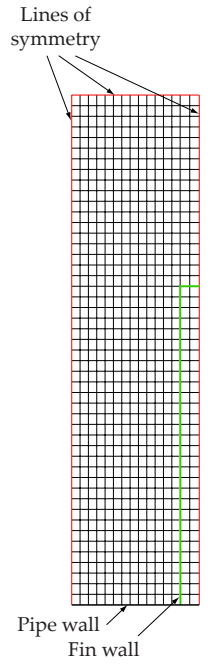

(b) *Computational grid used in the CFD study.*

Figure 10.7: *Section cut view of a pipe with circular fins, and a presentation of the CFD grid.*

The computational domain chosen to represent the geometry of a pipe with circular fins is shown in figure 10.7a. It is based on a section cut view in the longitudinal direction of the pipe. The vertical boundaries are placed in the center of the fin and midway between two fins due to symmetry considerations. The dimensions of the grid are provided in table 10.2 and correspond to those determined for proper design of circular fins in section 9.3.

Measure	Value	Unit
l_p	20	mm
h_f	25	
h_{ex}	15	
t_f	[2,3]	

Table 10.2: *Physical dimensions of the computational domain of the 2D circular fin grid. Characteristic names refer to figure 10.7a.*

10.2.1 Grid Independence and Quality of 2D Circular Fin Grid

Details of the grid in terms of size and quality are summarised in table 10.3. Due to all cells of the domain being completely orthogonal, the grid can easily be constructed with a high quality, which is clearly reflected in the characteristic numbers presented in table 10.3. The grid independence study is based on the temperature profile

Index	No. of cells, tot. domain	No. of cells, y-axis	Angular skewness Q_{EAS}	Size change Q_{SC}	Aspect ratio Q_{AR}
53	720	48	0 - 0.01	0.99 - 1	1.1 - 1.3
100	1344	64	0 - 0.01	0.99 - 1	1.24 - 1.33
270	3640	104	0 - 0.01	0.99 - 1	1.28 - 1.36

Table 10.3: *Grid size details and characteristic numbers for the grid qualities of the three grids considered for the 2D circular fin grid.*

along the vertical dash-dot line in through the center of the domain shown in figure 10.7a. Though showing some limitations in the previous section, the method is found acceptable for evaluation of these grids, as given temperature fluctuations are likely to appear along this line (see figures 10.10a and 10.10b).
Temperature profile of the three grids are plotted in figure 10.8, from which it is clear that the lines to a high degree are coincident. Because of this, the coarsest grid is selected to ease the computational load.

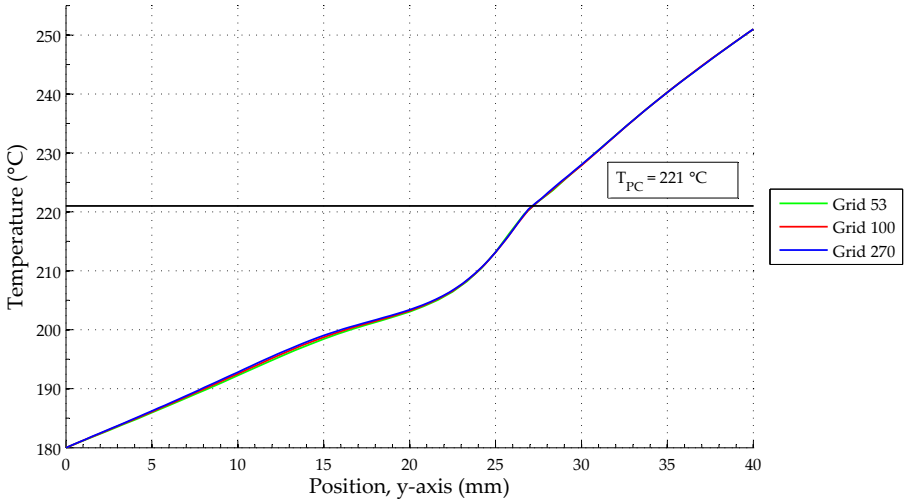

Figure 10.8: *Temperature profiles of the grids considered for the grid independency study (discharge mode 1, 10 minutes simulation time).*

10.2.2 Results of the 2D Circular Fin Simulation

The first 4 time steps of the solution were computed with a time step size of 1 s. All remaining time steps were of the size 0.5 s and used the First Order Upwind scheme as discretisation procedure. A plot of the residuals of the first 16 time steps is presented in figure 10.9. Convergence is almost achieved for the first 4 time steps while the convergence criteria are easily met for the following time steps. By inspection of

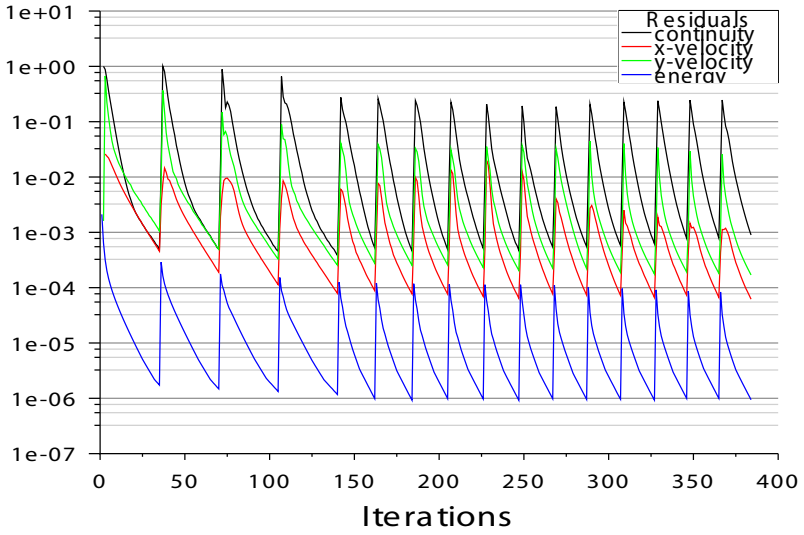

Figure 10.9: *Residuals of the first 16 time steps of the discharge 1 simulation.*

the output data from the simulation[2], the number of iterations later decreased to a steady level of about 6-8 per time step. The convergence behaviour for the smooth pipe simulation presented in section 10.1 is very similar to that shown in figure 10.9. Like the preceding section, the main focus is directed towards the longer time scale of the problem, and therefore contour plots are presented for 1 hour of simulation time. Temperature and liquid fraction information for discharge modes 1 and 2 are given in figures 10.10a to 10.11b. Note that the illustrations share the same scale, which is the reason for only presenting one scale for each pair of plots. Recall that discharge mode 1 considers a significant amount of sensible heat, while mode 2 mainly focuses on the latent heat of phase change (see table 5.2 for details). The geometry considered here, is that of a 2 mm thick graphite fin.

The results indicate that the fin does indeed affect the temperature of the PCM out to a larger radius than for a smooth pipe. Thereby solidification can progress further out away from the pipe by the use of circular fins. In line with the results found in the previous section 10.1, the larger differences in temperature associated with the first mode of discharge causes more effective heat transfer and ultimately solidification. In fact, figure 10.11b shows that the entire domain is completely solidified by 60 minutes of elapsed time.

From figure 10.10a and 10.10b, it is seen that the temperature profile along the length of the fin is only experiencing minor changes. As the fin efficiency is a measure of the temperature distribution along the fin length, a very high fin efficiency is observed from this CFD analysis, which contrasts to the low theoretically calculated efficiencies of section 9.2.

[2]In order to put this into perspective, 60 minutes simulation time with the given choices of time step size provides a total of 7196 time steps to be computed.

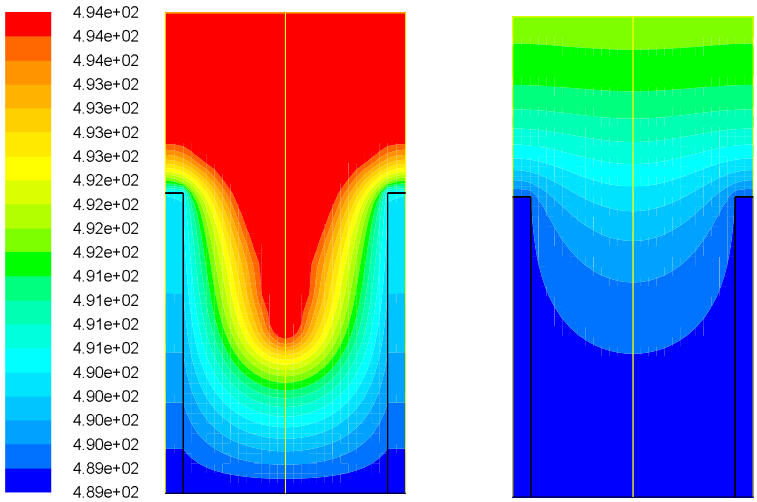

(a) *discharge mode 2.* **(b)** *discharge mode 1.*

Figure 10.10: *Contour plots of temperature in the computational domain after 60 minutes of elapsed time. Note that plots are reflected around the left vertical boundary of the domain and that temperatures are presented in K.*

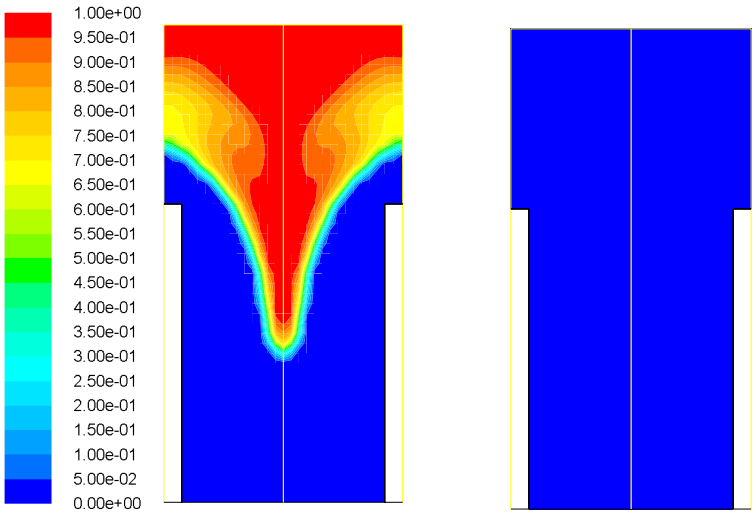

(a) *discharge mode 2.* **(b)** *discharge mode 1.*

Figure 10.11: *Liquid fraction contours for both modes of discharge. Evaluated after 60 minutes. Plots are reflected around the left vertical boundary of the domain.*

10.3 Summary of 2D CFD Analysis

The two dimensional treatment of a smooth pipe immersed in liquid PCM in discharge operational mode suggests that two distinct periods can be defined within the time frame considered of zero to 60 minutes. Within the first period, which stretches from $t = 0$ to $t \approx 7$ minutes, the mode of heat transfer happens predominantly due to natural convection flows occurring in the bottom half of the domain. Towards the end of period one, the PCM in the bottom half approaches isothermal conditions,

causing the natural convection flow to fade and the second period is commenced. Here, the PCM is almost stationary, hence the primary mode of heat transfer is conduction. At this point, most of the sensible heat has already been extracted in the first period, which means the content of latent heat starts to decrease and consequently causing the PCM to change phase.
A 2D simulation of the fin geometry determined in section 9.3 indicated that a finned pipe surface is able to increase the rate of solidification outwards in the radial direction from the pipe surface. Furthermore, the simulation suggests that discharge 1 is associated with a significantly higher rate of PCM solidification than mode 2, which must be caused by the larger ΔT of mode 1. This tendency was also seen in the results of the smooth pipe. However, as the solid-liquid interface shape was found to be irregular, assumably due to temperature stratification in the vertical direction, the assumption that solidification happen uniformly around the pipe might be a little off. The two dimensional treatment of the finned surface constrains the movement of the PCM from flowing past the pipe, thus some important 3D effects of the natural convection induced flow might be omitted by this approach.

Part IV

3D Study

Chapter

11

3D CFD Analysis

In section 10.3 it is mentioned how a 2D CFD simulation has some limitations regarding resembling the real three dimensional geometry of a circular finned tube. To overcome these limitations, a 3D simulation is created. This simulation is primarily evalutated on the solidification of the PCM, as the desire of the study (among other things) is to be able to estimate a reasonable heat surface design.
The computational domain in question is presented in figure 11.1. To keep computational time at a reasonable level, the computational domain is kept as small as possible. This is done by placing the vertical boundaries of the domain in the center of the fins, in order to exploit the symmetry of the geometry considered.

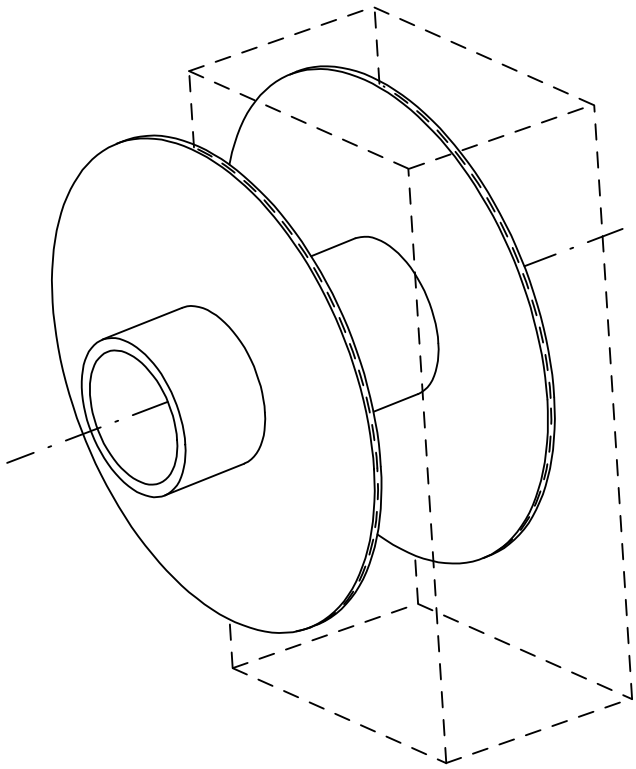

Figure 11.1: *Tube with circular fins marked with the section considered for the 3D computational domain.*

All sides of the domain are made as a symmetry. This means that the model acts as a similar domain is in all directions. This simulates that the heat surfaces are in a larger system with similar neighbouring finned tubes.

11.1 3D Grid Independence

Just as in section 6.4, a grid independency analysis for the 3D grid is done. This is to ensure a valid solution and to reduces the risk of non-convergence. The grid is first presented in its basic parts. The basic parts consist of a pipe, fin, fin edge and the surrounding box. The surrounding box is the computational domain, which is presented in figure 11.1.

11.1.1 Grid Presentation

Creating a grid of the pipe is carried out by setting a certain number of cells in the axial direction of the pipe. Fins are attached in each end of the pipe. It is expected that the PCM changes phase at both the fin surface and pipe surface, a grading is added to the pipe mesh to ensure dense grid near the fins. Grading is a grid ratio in a certain direction. This reduces the density of the grid at the middle of the pipe.

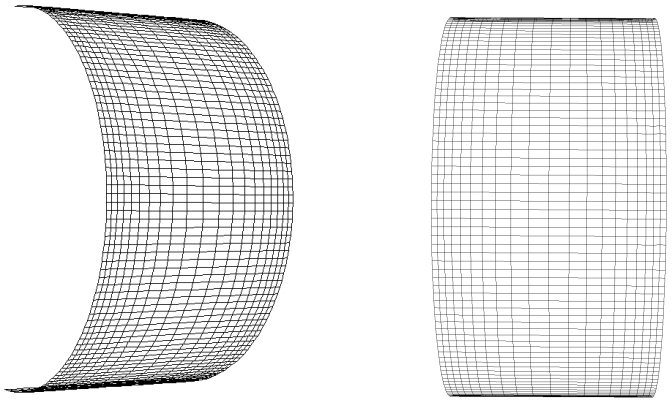

(a) *The pipe grid is shown in perspective.*

(b) *Pipe grid is here shown normal to the surface.*

Figure 11.2: *Presentation of pipe grid from two differenct views. The figure clearly shows the grading in the axial direction.*

The grid at the circumference of the pipe, is governed by the fin grid, which is presented in figure 11.3. The number of cells in the fin circumference equals the number on the pipes circumference. This grid has no grading, as there are no changes in the geometry in this direction. The radial direction of the fin has a small grading to keep a low change in aspect ratio. This also ensures a dense grid at the pipe surface.

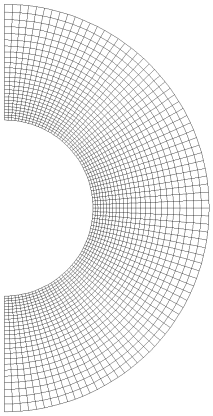

Figure 11.3: *Presentation of the grid of the fin in radial direction. It is clearly shown, that the radial grading ensures a low change in aspect ratio.*

Grid at the fin edge is shown in figure 11.4. Due to only half of the fin thickness being included in the domain, this region is quite thin therefore contains only a small amount of cells across.

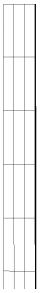

Figure 11.4: *The fin edges only contains few cells across. No grading is present.*

Due to the small amount of cells in the fin edge, grading is not present. To contain a certain amount of PCM in the model, a box is created around the pipe and fins. This box is divided in to an upper and a lower part. The number of cells in the circumference is determined by grid in the fins. The number of cells in radial direction is determined by the need for a low aspect ratio. This is in this case a compromise between a large aspect ratio and large cells, which can be seen in figure 11.5.

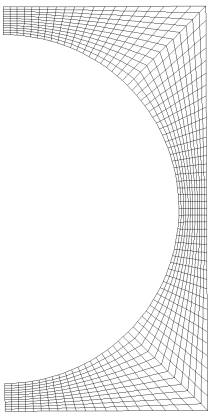

Figure 11.5: *The figure presents the domain which only contains PCM.*

Here it is clear that large aspect ratios appears where the box walls are close the fins. Reducing the number of cells in radial direction would reduce this aspect ratio, but this increases the cell size at the corner edges. The corner edges also contains the cells with the largest angular skewness.
Each grid in this study is presented in table 11.1.

Index	Cells, total	Circumference	Pipe	Fin, radial	Fin, across	Box, radial
41	31920	30	15	19	2	9
69	52992	36	17	22	3	10
100	76960	40	20	25	3	12
165	126720	48	24	30	3	14
320	246240	60	30	36	4	18

Table 11.1: *Grid size details of the five grids considered for this grid independency study.*

Each grid is evaluated according to the same key figures as in section 6.4. It can be seen from table 11.2, that the investigated grids fulfill the requirements mentioned in section 6.4. That means that the angular skewness $Q_{EAS,max}$ is < 0.56, Size change Q_{SC} is < 2 and that aspect ratio Q_{AR} does not exceed the range 20 to 100 in important regions. The figures for Q_{AR} are for the entire grid.

Index	No. of cells	Angular skewness Q_{EAS}	Size change Q_{SC}	Aspect ratio Q_{AR}
41	31920	0 - 0.5	0.98 - 1.50	1.0 - 6.28
69	52992	0 - 0.5	0.97 - 1.40	1.1 - 8.50
100	76960	0 - 0.5	0.99 - 1.62	1.0 - 8.36
165	126720	0 - 0.5	0.97 - 1.24	1.0 - 9.5
320	246240	0 - 0.5	0.97 - 1.40	1.0 - 13.8

Table 11.2: *Characteristic numbers of the grid quality.*

All five grids are modelled with a simulation time of 10 minutes. To evaluate the difference of each grid, a temperature plot is made. The temperature is measured from the pipe surface in radial direction to the domain boundary.

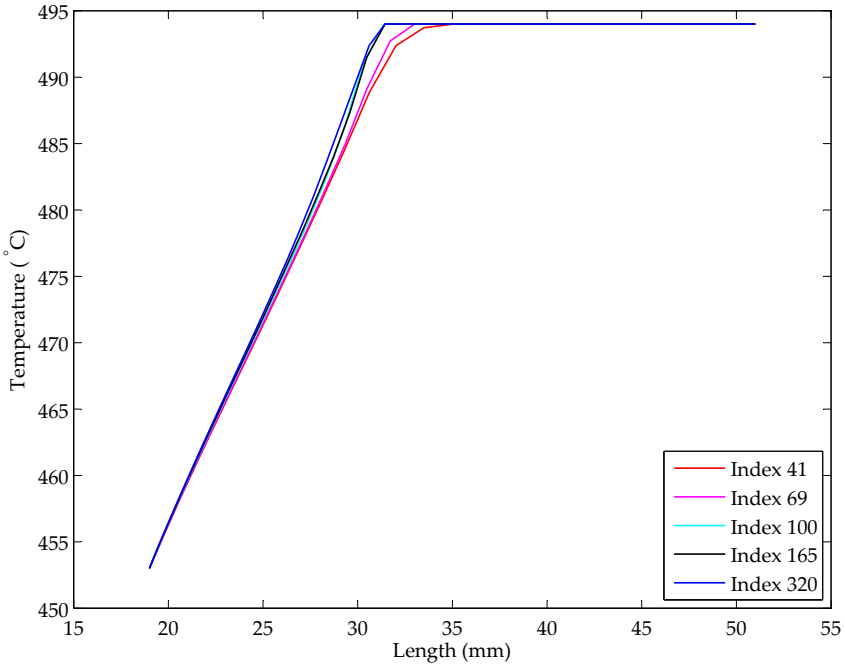

Figure 11.6: *Temperature plot for five different grid sizes.*

As figure 11.6 clearly shows, grid index 41 and 69 deviate clearly from index 100, 165 and 320. There is a slight difference between index 100 and index 165, while index 165 and 320 are almost identical. The small difference between index 100 and index 165/320 is considered to be insignificant. Hence, index 100 is chosen as the preferred grid for further simulations.
The domain in the grid independency analysis has been modelled with a simulation time of 10 minutes. From the evaluation of these simulations, it appears that the domain around the fin and pipe is not large enough. This means that a significant large amount of PCM is solidified, which leads to the conclusion, that the 60 minute simulations would not show any significant difference in temperature. Therefore the domain is expanded. To keep the same grid size proportionally, additional grid points are inserted according to this expansion. That means that the grid is similar to index 100 but slightly larger.

Cells, total	Circumference	Pipe	Fin, radial	Fin, across	Box, radial
120960	40	20	25	3	29

Table 11.3: *Final grid dimensions for evaluating the 3D model.*

No. of cells	Angular skewness Q_{EAS}	Size change Q_{SC}	Aspect ratio Q_{AR}
120960	0 - 0.5	0.99 - 1.35	1.0 - 12.8

Table 11.4: *Characteristic numbers of the final grid quality.*

11.2 3D CFD Results

The, in table 11.3, chosen grid is used for further investigations. This is done in two simulations, split into four different time scenarios. The two simulations are for a circular graphite fin and a circular steel fin. Both models are nearly similar. Only difference is the fin thickness, which is 2 mm for graphite fin and 3 mm for steel fin. Simulation times are according to table 5.3.
The models are set up as a transient model with initial time step size of 5 seconds for the first 4 time steps. After this, the time step size is reduced to 1 second. *Pressure-Velocity Coupling* scheme is set to the *SIMPLE-algorithm* and spatial and temporal discretisation of momentum and energy is set to *First Order Upwind*. Figure 11.7 shows the convergence history for the initial time steps. The model does not converge with time steps of 5 seconds, but converges when time step size is reduced to 1 second.

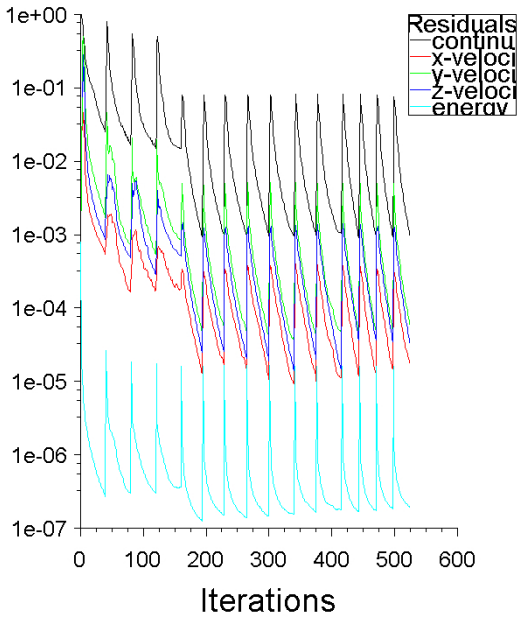

Figure 11.7: *Convergence history for the 3D simulation for the pipe with circular fins.*

The results of the simulations are presented in figure 11.8a. The figure shows how five planes are placed in the computational domain. The five planes are denoted, *north (N), northeast (NE), east (E), southeast (SE)* and *south (S)*. Each plane presents the conditions of the solid-liquid interface in discharge mode 1.

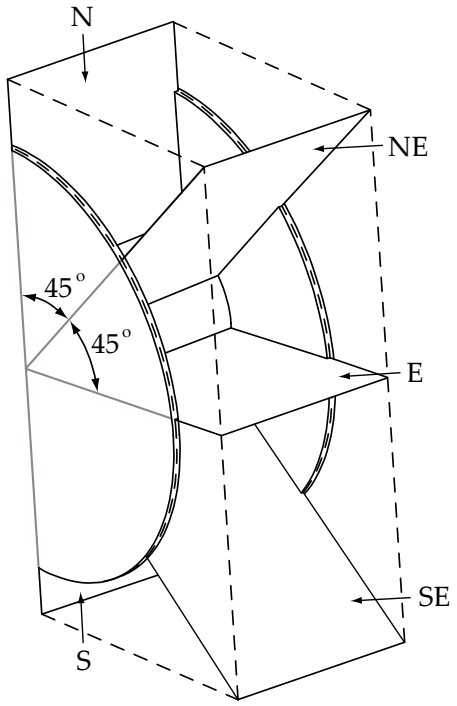

(a) *The figure shows how the planes are taken from the domain. The five planes are north, northeast, east, south east and south.*

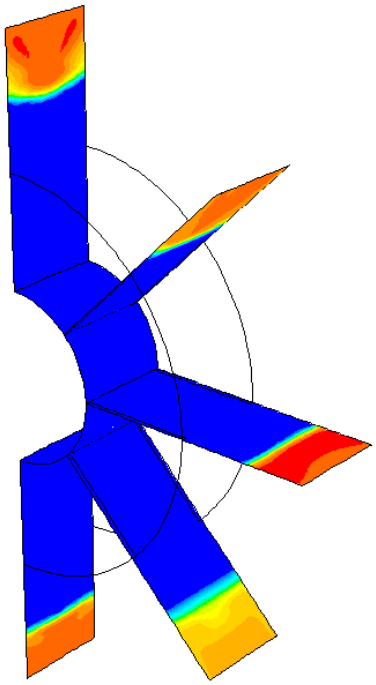

(b) *The planes shown in figure 11.8a are here shown in the FLUENT model.*

Figure 11.8: *Illustration of the location of the five planes.*

Each plane represent the conditions at its location. This is used to evaluate the solidification front around the fins. When all five planes are presented, this gives a good picture of the conditions in the domain. All five planes for 2 mm graphite fin and 3 mm steel fin are presented in figure 11.9 and 11.10, respectively.

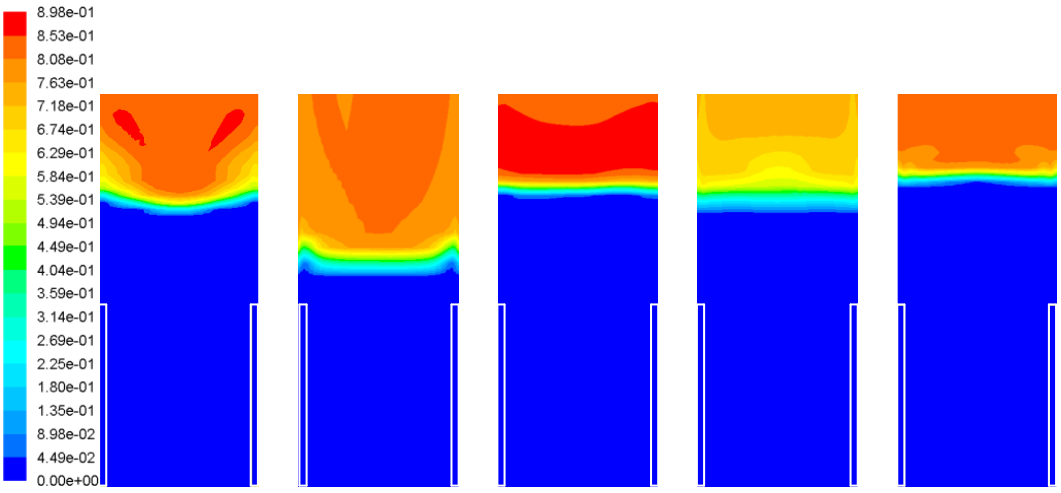

Figure 11.9: *All five planes are presented here. From left to right, it is north, north-east, east, south-east and south, according to figure 11.8a. Presented here is 2 mm graphite fins after 60 minuts of simulation time.*

It is clear from the figures that a very large part of the PCM is solid. Four of the five planes have an almost similar height of the solidification front. Only northeast plane stands out. The figure also shows, that all PCM is solidified between the fins. Figure 7.4 on page 72 showed that heat flux decreases with increasing layer of solid PCM. This indicates, that heat transfer after 60 minutes, as in the model of figure 11.9, is low. To evaluate this, the heat flux at each simulation time is presented in figure 11.12.
To compare steel and graphite as fin material, a model with steel fins is made. Here the fin thickness is increased to 3 mm. The result is presented in the same manner as 2 mm graphite fins.

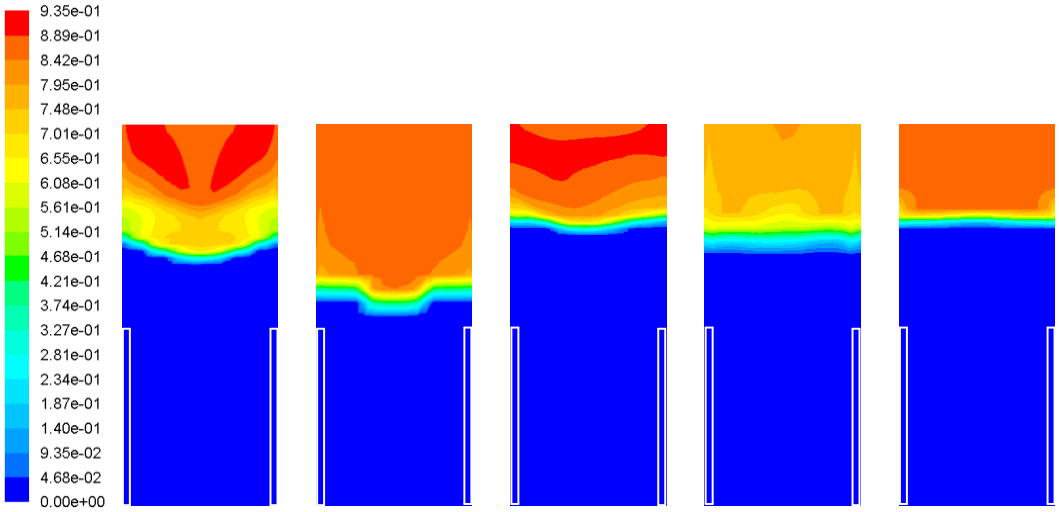

Figure 11.10: *Steel fins are here modelled and presented in the five planes. From left to right, it is north, north-east, east, south-east and south, according to figure 11.8a.*

Just as with 2 mm graphite fins, the PCM is solidified between the fins. The height of the solidification front is almost the same as for graphite fins. This indicates, that after 60 minutes, there is only small difference in heat transfer between 2 mm graphite fins and 3 mm steel fins. To further compare the two fin types, a presentation of liquid fraction of the domain and pipe heat flux is presented.
Each model contains the same volume of PCM. Therefore it can be compared to the fraction of liquid PCM after end of the simulation time. This is presented in figure 11.11.
Figure 11.11 clearly shows that there is not much difference between the two fin types. Graphite is slightly better at the start of the simulation, but as time progresses, the curves of the two fin types are almost parallel. Similar tendencies can be seen in figure 11.12 for the heat flux.
Here it is seen, that graphite has the highest heat flux at the beginning, but as time progresses, steel seems to have a higher heat flux. Just as with liquid fraction, the curves are almost parallel, which shows, that there is not much difference in heat transfer between the two fin types in discharge mode. The heat flux is quite high at the beginning, which is due to the high temperature difference between PCM and HTF, and the fact, that there is only little PCM on the heat surfaces. Similar can

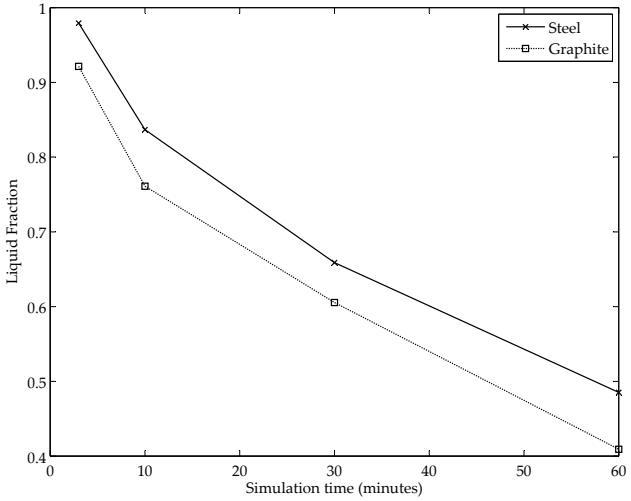

Figure 11.11: *Liquid fraction for both graphite and steel fins is plotted according to the four simulation times.*

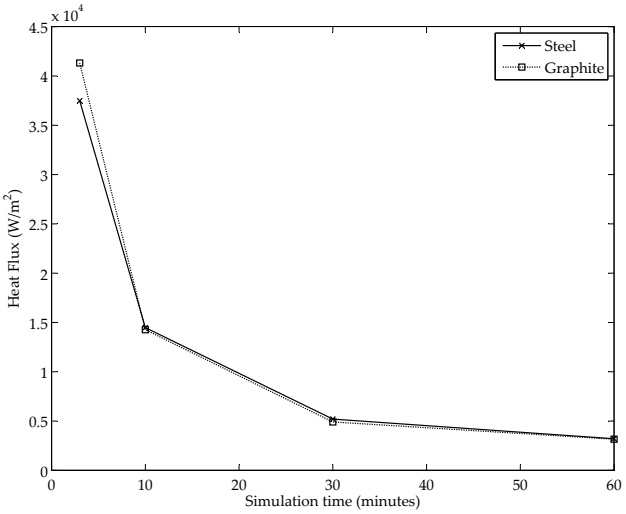

Figure 11.12: *Heat flux as a function of simulation time. This is applicable for both graphite and steel fins.*

be seen from figure 11.13 which shows the average temperature of the PCM.
Figure 11.13 shows how the average temperature of the PCM decreases faster with graphite fins. The temperature difference between the two fin types is, however, decreasing as a function of time. This is a result of the larger heat flux of steel fins from 10 to 60 minutes.

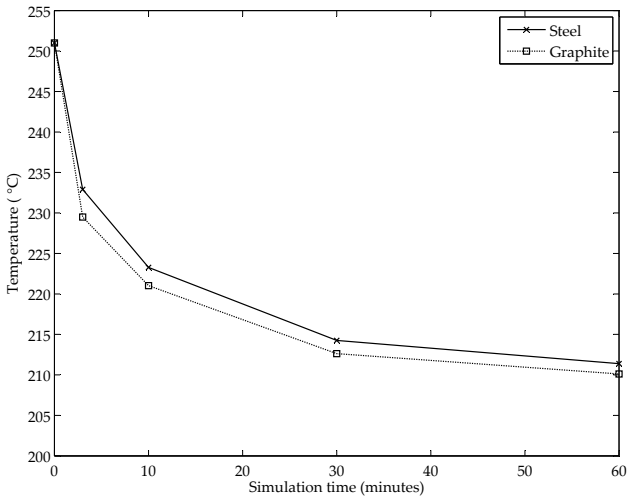

Figure 11.13: *The figure shows the behavior of the PCM mean temperature as a function of simulation time.*

11.3 Summary of 3D CFD Analysis

As could be seen from figure 11.12, the heat flux decreases rapidly. When figure 7.4 is considered, it becomes clear that figure 11.12 show the same tendency. With this in mind, it becomes obvious that as long as the PCM solidifies on the heat surface, the heat surface material is of less importance, due to the low conductivity of PCM, which acts as an insulation on the heating surface. This is, however, only valid during discharge. Figure 9.1 shows a different tendency during charge. During charge, there is no solid PCM directly on the heat surface, and as could be seen from table 8.1, the contribution from natural convection is substantial.

Chapter

12

Heating Surface Design

In section 11.2 is was shown how the PCM solidifies around the heat surfaces with a decreasing heat flux as a result. This was shown in figure 11.12. Figure 11.9 and 11.10 also showed how all PCM between the fins was solidified after 60 minutes of simulation time. Figure 12.1 shows the temperature in the PCM after 60 minutes with 3 mm steel fins.

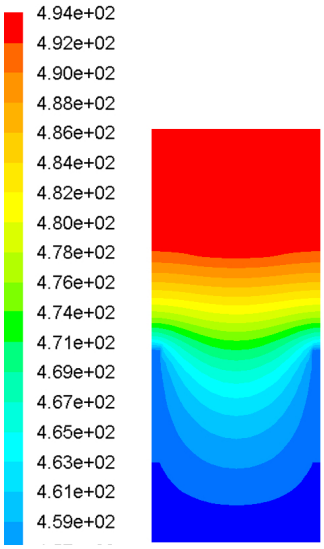

Figure 12.1: *Temperature plot of north face with graphite fins.*

Figure 12.1 show only minor temperature difference in the axial direction, and as heat transfer is a function of temperature difference, this reduces heat transfer. It is therefore disirable to increase this temperature difference, in order to reach a higher heat transfer.
In order to increase the temperature difference between the fins, there are two obvious directions to take. One is to increase the pitch between the fins. The other is to increase the fin height. Both suggestions are shown in figure 12.2
Four new simulations are therefore made, each to evaluate a new designs. Each new model takes its origin in the model with 3 mm steel fins used in section 11.2. Three models have an unchanged fin height of 25 mm but alternating pitch between the fins. The original model has 20 mm pitch, but the new models are made with 30, 40 and 50 mm, respectively. One new model is also made with an increased fin height.

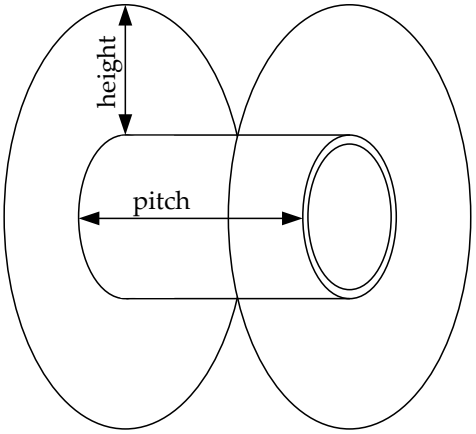

Figure 12.2: *Illustration of the design changes purposed.*

The fin height is increased to 50 mm and the fin pitch is maintained at 20 mm. Only one dimension is changed per model. This is to be able to evaluated the changed result with respect to the changed dimension. If two dimensions are changed, it can be difficult to determine what caused the change. The four new model dimensions are presented in table 12.1

Fin Height	Fin Pitch
25	30
25	40
25	50
50	20

Table 12.1: *Four new models are created with different dimensions. All dimensions mentioned are in mm.*

Due to limitation in computational time, the new models are only simulated for 3 and 10 minutes. This however seems to give a clear picture of the tendencies when comparing these models. The results are illustrated in figure 12.3.
The red curve in figure 12.3 is for a 25 mm fin height and 20 mm fin pitch, which was the size of the original model. This is in full already presented in figure 11.12, and is inserted here for comparison. It is clear from figure 12.3 that increased fin pitch causes heat flux to decrease when compared to the original design. A larger fin height, however, seems to be a better solution, as heat flux for this design is significantly higher than both the remaining new model and the original model.
Although increased fin height seems to be a better solution, it is however not without problems. A limitation of heating surface design is the actual construction of the finned tube. The tubes are often bend to get multible runs through the domain. To ensure that the tube is not damaged during the bend, a certain minimum bending radius is required. Typically the bending radius is the tube diameter (Condra, 2011). This is illustrated in figure 12.4.
When using finned tubes, the length of the fins must also be considered.

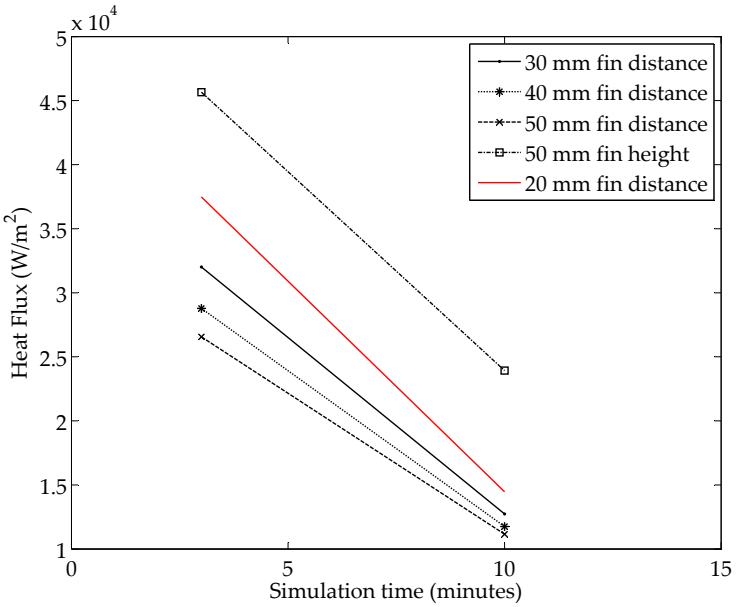

Figure 12.3: *Plot of teh heat flux of the new fin designs. The new models are simulated for 3 and 10 minutes.*

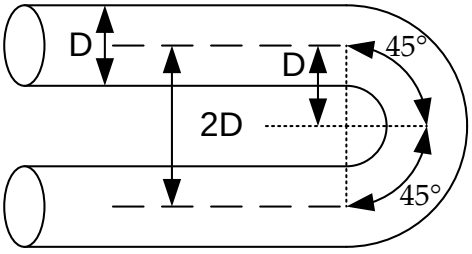

Figure 12.4: *To ensure minimum risk of damage during tube bend, a minimum bending radius is used. This bend is illustrated in the figure.*

As figure 12.5 shows, the location of fin must be considered. If fins are positioned precisely opposite of each other, fin height can only be half the diameter of the tube. Otherwiser there will be contact between the fins from the opposite pipe, as shown in figure 12.5a. If the fins are staggered as in figure 12.5b, fins can be higher. This design however decreases the area between the fins. The centerline in figure 12.5a and 12.5b illustrates the mittel of the space between the tubes. The fin height and fin location must therefore be considered along the tube bending radius, when designing the heat surface.

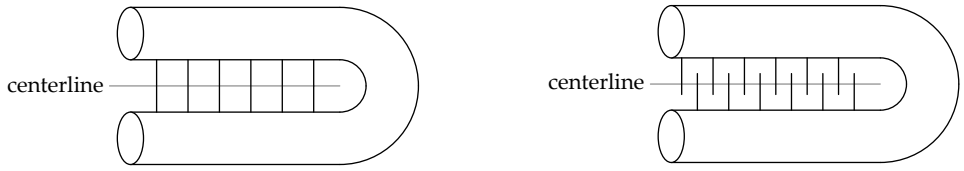

(a) *It is here shown how the fins meet along the centerline. This gives a maximum length of the fins when using the minimum bending radius.*

(b) *If fins are staggered, it enables them to be longer. This however reduces the free area between the fins at the other side.*

Figure 12.5: *When placing fins on a tube, it must be considered according to the neighboring tube. This is to reduce risk of fin contact.*

12.1 Future Work

It has been shown how the increased fin height have a positive effect on the heat flux. This could lead to the conclusion, that the higher fins the better. But if that is the truth, is the optimum solution then a system with only one tube and very large fins? This could be a matter to investigate, and to find the optimum solution between number of tubes in the system and the optimum fin height. This could be an optimum of best possible performance or of a minimum performance at the lowest production cost.

Fin thickness could also be a matter to investigate. As the PCM solidifies on the fin surface causing rapid decrease in heat transfer, the fin does need to be very thick in order to transfer the heat. This design parameter could be included in an optimisation study on the project.

Due to time constraints, only a single increased fin height was considered in this report, which was simulated for 3 and 10 minutes. Future work could be further investigation of this in order to evaluate performance after 30 and 60 minutes as was the case with the original model. Further time periods could also be investigated. This would depend on the requirements of the heat storage. For this work, the focus has predominantly been directed towards simulation time of 1 hour.

Chapter

13

Conclusion

In this report, studies have been carried out concerning the heat transfer and phase change phenomena of a phase change material (PCM) in a latent heat storage. A eutectic composition of potassium nitrate and sodium nitrate salt ($NaNO_3$-KNO_3) have been used as PCM throughout the study. This material is cheap, easy to handle, and has homogeneous and well-defined solidification properties. Furthermore, eutectic $NaNO_3$-KNO_3 has reportedly good stability properties, and no severe corrosion problems were found in connection with carbon steel, which is a commonly used heating surface material.

As opposed to older PCM heat storage technology, the general storage design considered is based on a container with stationary PCM and a heating surface immersed herein. However, due to the poor thermal conductivity of the PCM, heat transfer must be enhanced in order to a achieve a feasible storage design concept. In this report, this matter was investigated through the use of fins on the heating surface, with a main focus on the discharge aspect of the storage. The investigation was segregated into three stages: quasi-1D, 2D, and 3D. First, a quasi-1D study was conducted where the problem was treated as a transient heat diffusion problem including solid/liqiud phase change. Here, both CFD-based simulations and predictions made by a numerical model constructed for the purpose were made. However, as the quasi-1D study was only intended as a preliminary study, is was predominantly used to provide an preliminary idea of the rate of solidification/melting of PCM. In addition, it was shown that a simple numerical model involving prediction of the solid-liquid could be constructed, and that good resemblance with the results produced by the CFD code could be achieved.

In the 2D and 3D studies, the presence of natural convection in the PCM was included in the treatment of the problem. Calculations regarding the natural convection contribution to heat transfer within the storage indicated that this is an significant measure to include. This was confirmed by the CFD-simulations which suggested a non-uniform shape of the solid-liquid interface and temperature stratification along the vertical direction. Furthermore, both conduction and convectional heat transfer was observed in the simulations, but these were supposedly connected to separate time periods during the discharge process. Due to the importance of natural convection, it should be accounted for as much as possible in the heating surface design.

A proper fin geometry to be used for the heating surface was determined through theoretical evaluation of efficiency of circular steel and expanded graphite fins. However, large discrepancies were seen from these results to the results of the CFD simula-

tions. Because of this, it is the opinion of the authors that analytical fin efficiency considerations known from regular heating surface design, does not apply well to the nature of the given problem. That being said, CFD simulations did indicate that fins could effectively be applied for the purpose of extracting heat from the PCM at a radius further away from a heating surface pipe.
Further investigation of the heating surfaces revealed that solidified PCM on the heating surfaces acts as a thermal insulator, which appear as being the limiting factor of heat transfer in discharge mode. This also led to the result, that the choice of fin material was of lesser importance. Graphite and steel fins showed only minor differences in performance, however, this may not be the case when charging the storage. In order to increase heat transfer from the heating surfaces, a series of new designs were evaluated. Three different pitches and one new fin height. Of the new designs considered, only an increase in fin height lead to a significantly larger heat transfer.

Bibliography

ANSYS (2009a). ANSYS FLUENT 12.0 Theory Guide. Technical report, ANSYS Inc.

ANSYS (2009b). ANSYS FLUENT 12.0 User's Guide. Technical report, ANSYS Inc.

Baker, B., T. Heffler, and C. Márquez (2010). The Concentrated Solar Power Markets Report 2010. Technical report, CSPToday.

Bayón, R., E. Rojas, L. Valenzuela, E. Zarza, and J. León (2010). Analysis of the Experimental Behaviour of a 100 kWth Latent Heat Storage System for Direct Steam Generation in Solar Thermal Power Plants. *Applied Thermal Engineering 30*, 2643–2651.

Berg, R. W. and D. H. Kerridge (2002). Raman Mapping in the Elucidation of Solid Salt Eutectic and Near Eutectic Structures. *Journal of Raman Spectroscopy 33*, 165–172.

Bloch, H. P. (1995). *A Practical Guide to Steam Turbine Technology*. McGraw-Hill.

Brandt, F. (1985). *Wärmeübertragung in Dampferzeugern und Wärmeaustauschen - FDBR-Fachbuchreihe Band 2*. Vulkan-Verlag.

Casey, M. and T. Wintergerste (2000). Best Practice Guidelines. Technical report, European Research Community on Flow, Turbulence and Combustion (ERCOFTAC).

Çengel, Y. A. (2006). *Heat and Mass Transfer - A Practical Approach* (3 ed.). Mc.

Condra, T. (2011, May). Personal Communication.

DLR (2005). Concentrating Solar Power for the Mediterranean Region, Executive Summary. Technical report, German Aerospace Center (DLR) Institute of Technical Thermodynamics.

DLR (2006). Trans-Mediterranean Interconnection for Concentrating Solar Power, Executive Summary. Technical report, German Aerospace Center (DLR) Institute of Technical Thermodynamics.

DLR (2007). Concentrating Solar Power for Seawater Desalination, Executive Summary. Technical report, German Aerospace Center (DLR) Institute of Technical Thermodynamics.

DLR (2008). Project DISTOR. www.dlr.de. [Online; accessed 10-April-2011], Deutsches Zentrum für Luft- und Raumfahrt.

DLR (2009). DESERTEC: Solar power from the desert. www.dlr.de. [Online; accessed 14-April-2011], Deutsches Zentrum für Luft- und Raumfahrt.

Dusinberre, G. M. (1945). Numerical Methods for Transient Heat Flows. *Trans. ASME 67*, 703.

Energinet.dk (2011, February). Extracted Marketdata. www.energinet.dk. [Online; accessed 25-February-2011].

Goods, S. and R. Bradshaw (2004, February). Corrosion of Stainless Steels and Carbon Steel by Molten Mixtures of Commercial Nitrate Salts. *Journal of Materials Engineering and Performance 13*(1), 78–87.

Hashemi, H. T. and C. Sliepcevich (1967). A Numerical Method for Solving Two-Dimensional Problems of Heat Conduction With Change of Phase. *Chem. Eng. Prog. Symp. 63*(79), 34–41.

Herrmann, U. and D. W. Kearney (2002). Survey of Thermal Energy Storage for Parabolic Trough Power Plants. *Journal of Solar Energy Engineering 124*, 145–152.

Kamimoto, M., T. Tanaka, T. Tani, and T. Horigome (1980). Investigation of Nitrate Salts for Solar Latent Heat Storage. *Solar Energy 24*, 581–587.

Kenisarin, M. and K. Mahkamov (2007). Solar Energy Storage Using Phase Change Materials. *Renewable and Sustainable Energy Reviews 11*. 1913-1965.

Kenisarin, M. M. (2010). High-temperature Phase Change Materials for Thermal Energy Storage. *Renewable and Sustainable Energy Reviews 14*.

Kerridge, D. H., A. Horsewell, and R. W. Berg (2009). The Structure of Solid Salt Eutectics - Why Lamellar or Conglomerate? *Solid State Ionics 180*, 1453–1456.

Kramer, C. M., Z. A. Munir, and J. V. Volponi (1982). Differential Scanning Calorimetry of Sodium and Potassium Nitrates and Nitrites. *Thernrochimica Acta 55*, 11–17.

Kreith, F., R. F. Boehm, and G. D. Raithby (1999). *Mechanical Engineering Handbook*. CRC Press LLC.

Laing, D., T. Bauer, W. Steinmann, and D. Lehmann (2009). Advanced High Temperature Latent Heat Storage System - Design and Test Results. In *The 11th International Conference on Thermal Energy Storage - Effstock 14-17 June 2009 in Stockholm, Sweden.*

LOGSTOR (2011). *Material Specifications of Steel 35.8.*

Mandø, M. (2009). Numerical Fluid Dynamics - Lectures 7-8. Internal Teaching Notes, Dept. of Energy Technology, Aalborg University.

McDonald, J. and H. T. Davis (1970). Thermal Conductivity of Binary Mixtures of Alkali Nitrates. *The Journal of Physical Chemistry 74*, 725–730.

Medrano, M., A. Gil, I. Martorell, X. Potau, and L. F. Cabeza (2009, January). State of the Art on High-Temperature Thermal Energy Storage for Power Generation. Part 2 - Case Studies. *Renewable and Sustainable Energy Reviews 14*(1), 56–72.

Mehling, H. and L. F. Cabeza (2008). *Heat and Cold Heat Storage with PCM*. Springer-Verlag.

Meyer, G. H. (1973). Multidimensional Stefan Problems. *Siam Journal on Numerical Analysis 10*(3), 522–538.

Mills, A. F. (1995). *Heat and Mass Transfer*. Richard D. Irwin, Inc.

Omotani, T., Y. Nagasaka, and A. Nagashima (1982). Measurement of the Thermal Conductivity of KNO3-NaNO3 Mixtures Using a Transient Hot-Wire Method with a Liquid Metal in a Capillary Probe. *International Journal of Thermophysics 3*(1), 17–26.

Pacheco, J. E., M. E. Ralph, J. M. Chavez, S. R. Dunkin, E. E. Rush, C. M. Ghanbari, and M. W. Matthews (1995). Results of Molten Salt Panel and Component Experiments for Solar Central Receivers. Technical report, Sandia National Laboratories, US Department of Energy.

Papon, P., J. Leblond, and P. H. E. Meijer (1999). *The Physics of Phase Transitions*. Springer-Verlag.

Patankar, S. V. (1980). *Numerical Heat Transfer and Fluid Flow*. McGraw-Hill.

Peng, Q., J. Ding, X. Wei, J. Yang, and X. Yang (2010). The Preparation and Properties of Multi-Component Molten Salts. *Applied Energy 87*.

Pincemin, S., X. Py, R. Olives, M. Christ, and O. Oettinger (2008). Elaboration of Conductive Thermal Storage Composites Made of Phase Change Materials and Graphite for Solar Plant. *Journal of Solar Energy Engineering 130*, 51–55.

Poirier, D. and M. Salcudean (1988). On Numerical Methods Used in Mathematical Modeling of Phase Change in Liquid Metals. *Journal of Heat Transfer 110*, 562–570.

Price, H., E. Lüpfert, D. Kearney, E. Zarza, G. Cohen, R. Gee, and R. Mahoney (2002). Advances in Parabolic Trough Solar Power Technology. *Journal of Solar Energy Engineering 124*, 109–125.

Silverman, M. D. and J. R. Engel (1977). Survey of Technology for Storage of Thermal Energy in Heat Transfer Salt. Technical report, Oak Ridge National Laboratory.

Skumanich, A. (2010, September/October). CSP: Developments in Heat Transfer and Storage Materials. *Renewable Energy Focus 11*(5), 40–43.

Sørensen, K. (2011, May). Personal Communication.

Steinmann, W.-D. and R. Tamme (2008). Latent Heat Storage for Solar Steam Systems. *Journal of Solar Energy Engineering 130*, 41–45.

Tacke, K.-H. (1985). Discretization of the Expliclt Enthalpy Method for Planar Phase Change. *International Journal for Numerical Methods in Engineering 21*(3), 543–554.

Tamme, R., D. Laing, and W.-D. Steinmann (2004). Advanced Thermal Energy Storage Technology for Parabolic Trough. *Journal of Solar Energy Engineering 126*, 794–800.

Tufeu, R., J. P. Petitet, L. Denielou, and B. L. Neindre (1985). Experimental Determination of the Thermal Conductivity of Molten Pure Salts and Salt Mixtures. *International Journal of Thermophysics 6*(4), 315–330.

VDI (2010). *VDI Heat Atlas* (2 ed.). Verein Deutscher Ingenieure.

Versteeg, H. K. and W. Malalasekera (2007). *An Introduction to Computational Fluid Dynamics - The Finite Volume Method*. Pearson Education Limited.

Vogel, C., C. Juhl, and E. Maahn (2001). *Metallurgi for Ingeniører*. Polyteknisk Forlag.

Voller, V. R. and C. Prakash (1987). A Fixed Grid Numerical Modelling Methodology for Convection-diffusion Mushy Region Phase-change Problems. *International Journal for Heat and Mass Transfer 30*, 1709–1719.

Witte, U. (1976). *Steinmüller - Steam Generation*. Vulkan-Verlag.

Zarza, E., L. Valenzuela, J. León, K. Hennecke, M. Eck, H. Weyers, and M. Eickhoff (2004). Direct Steam Generation in Parabolic Troughs: Final Results and Conclusions of the DISS Project. *Energy 29*.

Zhang, X., J. Tian, K. Xu, and Y. Gao (2003). Thermodynamic Evaluation of Phase Equilibria in NaNO3-KNO3 System. *Journal of Phase Equilibria 24*(5), 441–446.

Part V

Appendices

Appendix

A

Parabolic Trough Collectors

Of the different varieties of solar collector concepts presented in section 1.1, the parabolic trough collector has, so far, been the preferred choice in the majority of CSP plant designs, which is evident from the data presented in figure A.4b. Moreover, the future would belong to the parabolic trough design as well (please consider the plots A.1 and A.2). Therefore, a short review of the advances in the development of the technology is presented in the following.

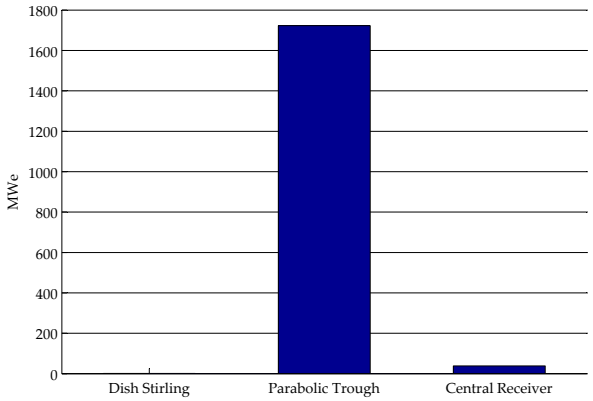

Figure A.1: *MW_e of collector technology used in CSP plants worldwide currently under construction. Number are of 2010. Plot reproduced by the authors with data from Baker et al. (2010).*

The use of PTCs was originally intended for industrial process steam production, which was the primary role of the technology in the 1970s and 1980s. However, this purpose often proved not to be a feasible choice due a number of market barriers, some of which are: high engineering and marketing requirements and non-competitive returns of these projects. One of the pioneering facilities with regard to PTC-based power production was the so-called Solar Electric Generating System (SEGS) plants I and II in Kramer Junction, California, where a total of nine plants were built and operated from 1985 to 1991 with an accumulated capacity of 354 MW. Since then, PTC technology has experienced increasing interest, for instance as a result of the increasing interest in renewable energy sources in recent years (Price et al., 2002). Details of the individual SEGS plants are presented in figures A.3a and A.3b. On European grounds, the large DIrect Solar Steam (DISS) project was launched in 1995, where PTCs were installed at *Plataforma Solar de Almeria* (PSA), Spain, to investigate the feasibility of the Direct Steam Generation (DSG) operation principle

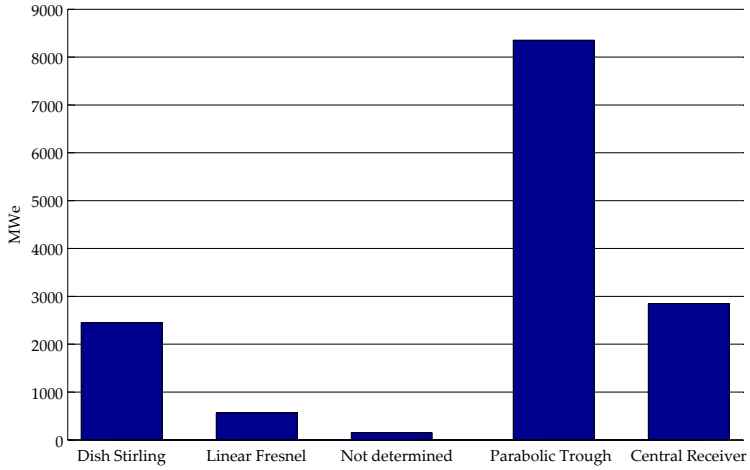

Figure A.2: *MW_e of collector technology of planned CSP plants worldwide. Number are of 2010. Plot reproduced by the authors with data from Baker et al. (2010).*

of a CSP plant.

PTC Improvements

It is beyond the scope of this report to provide a complete summary of the advances made through the years within PTC designs, but the EuroTrough concept is singled out and reviewed in the following, as it is popular amongst many CSP project developers (including tests at PSA during the DISS project) and because it includes good examples of the progress made in this area. The reader is referred to Price et al. (2002) for further details on trough design development of other platforms.
The EuroTrough collector was carefully developed as a replacement of the earlier LS 1, 2, and 3 designs which were used at the SEGS plants in California. It is based on a 12 m long steel space-frame and includes mirrors, absorber pipes, and a solar tracking system. A picture of a EuroTrough prototype from the PSA facility in Almeria, Spain is shown in figure 1.1. These units can be connected in series with a single drive in one end to rotate the entire length of collectors.
The structural frame was improved by conducting wind load analysis and finite element studies, which led to a number benefits regarding performance, manufacturing, transportation and on-site installation. For instance, the rotational axis was placed just above the center of gravity, and better torsional and bending stiffness of the structure was achieved. This improved the optical performance of the collector, and extended the total collector length from 100 m to 150 m and hereby reducing the number of drives required per solar field and the amount of interconnecting pipes, which lowers total collector costs and thermal losses. The simplicity of the space-frame design with significantly fewer components than the LS-3 concept, enabled the use of simpler manufacturing techniques and eased the on-site assembly. Furthermore, the improved design is less demanding in terms of preparation of the given site as the collectors can be installed on a slightly sloping terrain. As a result, the

SEGS Plant	First Year of Operation	Net Output (MW_e)	Solar Field Outlet Temperature (°C)	Solar Field Area (m^2)	Solar/Fossil Turbine Efficiency (%)	Annual Output (MWh)	Dispatchability Provided by
I	1985	13.8	307	82,960	31.5/NA	30,100	3 hours—thermal storage Gas-fired superheater
II	1986	30	316	190,338	29.4/37.3	80,500	Gas-fired boiler
III/IV	1987	30	349	230,300	30.6/37.4	92,780	Gas-fired boiler
V	1988	30	349	250,500	30.6/37.4	91,820	Gas-fired boiler
VI	1989	30	390	188,000	37.5/39.5	90,850	Gas-fired boiler
VII	1989	30	390	194,280	37.5/39.5	92,646	Gas-fired boiler
VIII	1990	80	390	464,340	37.6/37.6	252,750	Gas-fired HTF heater
IX	1991	80	390	483,960	37.6/37.6	256,125	Gas-fired HTF heater

Collector	Structure	Aperture width m	Focal length m	Length per element m^2	Length per collector m	Mirror Area per drive m^2	Receiver Diameter m	Geometric concentration sun	Mirror Type	Drive	Module Weight per m2 kg	peak optical efficiency %	Reference
LS-1	Torque tube	2.55	0.94	6.3	50.2	128	0.04	61:1	Silvered low-iron float glass	Gear	n/a	71	SEGS I+II
LS-2	Torque tube	5	1.49	8	49	235	0.07	71:1	Silvered low-iron float glass	Gear	29	76	SEGS II–VII
LS-3	V-truss framework	5.76	1.71	12	99	545	0.07	82:1	Silvered low-iron float glass	Hydraulic	33	80	SEGS V–IX
New IST	Space frame	2.3	0.76	6.1	49	424	0.04	50:1	Silvered thin glass	Jack screw	24	78	IST [14]
Euro-Trough	Square truss torque box	5.76	1.71	12	150	817	0.07	82:1	Silvered low-iron float glass	Hydraulic	29	80	PSA [9]
Duke Solar	Aluminum space frame	5	1.49	8	49–65	235–313	0.07	71:1	Silvered low-iron float glass	Hydraulic or gear	24	80 (projected)	Duke DS1 [12]

Note: Module weight is for the tracking parabolic concentrator unit and includes the structure, mirrors, receiver, and receiver supports. The pylons, drive system, and flexible interconnections are not accounted for in the module weight.

Figure A.3: *Characteristics of SEGS I through IX in Kramer Junction, California, and characteristics of different of parabolic trough collector designs. From Price et al. (2002).*

EuroTrough collector is cheaper, more efficient[1], and 14 % lighter than the LS-3 design (Price et al., 2002).

Apart from the structural frame, the reflector panels and absorber pipes have also undergone improvements. At the time of writing, the commonly used reflector is the *thick glass* type which are costly, but much attention is focussed on lighter and cheaper concepts *e.g. thin glass* which on the other hand are more prone to shattering. However, efforts are made to come up with a feasible thin glass design using special coating and other advanced manufacturing measures. Another example is NRELs longtime development of a cheap and light polymer reflector, but so far it has not met the requirements of lifetime operation in a solar field. More examples of

[1]About 3 % more efficient than the LS-3 was reported from prototype testing at PSA (Price et al., 2002).

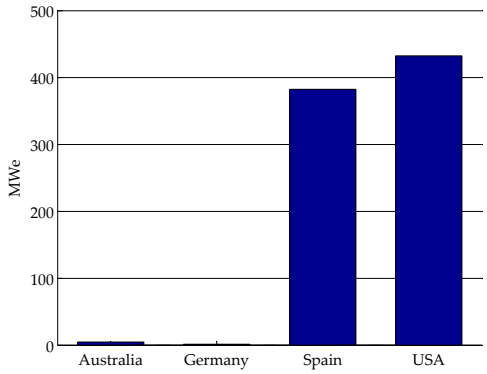

(a) *Installed CSP capacity distributed on countries as of by 2010.*

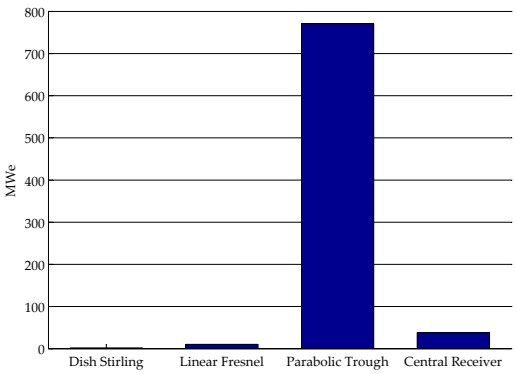

(b) *Installed CSP capacity distributed on solar collector technology as reported by 2010.*

Figure A.4: *Installed CSP capacity in relation to countries and collector technology as reported by 2010. Plots reproduced by the authors with data from Baker et al. (2010).*

special combinations of materials, coatings, etc. are provided in Price et al. (2002). The long-term durability is a crucial property of the panels as wind loads are significantly higher at the edge of the solar field causing more frequent panel breakage in this region. In this connection, the properties of the supporting structure is important as it should relieve the load imposed on the reflectors, which for instance was done successfully by a factor of three in the EuroTrough design when compared to LS-3 (Price et al., 2002).

The present day absorber technology of PTCs is based on a evacuated double pipe principle with a inner steel pipe absorbing and transferring heat to the HTF flowing internally. A cermet[2] coating of the pipe ensures optimal selective optical performance in terms of high absorbance of direct solar radiation and low emissivity to reduce thermal radiation losses. Surrounding this pipe is a glass tube with an antireflective coating on both inner and outer surfaces. The space between the concentric pipes is held at vacuum (typically ∼0.0013 Pa) to impede heat transfer away from steel pipe at high temperatures and to stop oxidation of the cermet surface. Each pipe section is fitted with bellows in each end to account for thermal expansion issues between the steel and glass materials. A sketch of the evacuated double pipe absorber concept is presented in figure A.5a. (Price et al., 2002).

The bellows, which also upholds the vacuum in the annulus, has previously been the Achilles' heel, so to speak, of the construction. It is a crucial component as the cermet surface will oxidise, with a resulting depleted performance, if it fails. However, finite element analysis has revealed that these glass-to-metal seals are particular sensitive to concentrated solar flux, so efforts are in progress to produce a new and more durable bellow design.

A newly introduced PTC absorber product, the UVEC of Solel Solar Systems, has a number improvements: more efficient cermet coating which is less sensitive to oxidation issues and shielding of the bellows. Though long-term durability still needs to be verified, reports from tests carried out so far showed improved performance of this

[2]Cermet (or CerMet) is a composite material based on ceramic and metal.

absorber pipe. Therefore, the UVEC is most likely the absorber to be used in future PTC installations, however, because the replacement of damaged absorber pipes typically is costly some cheaper alternatives are often used with existing PTCs. This involves removal of the outer glass tube and treatment of the exposed steel absorber pipe with special paints, coatings, and gels, which can reach 80-90 % performance of a new and fully functional UVEC absorber at about 20-30 % of the cost. Research in this area seem to be focussed on developing cheaper coatings and gels with acceptable optical properties to be implemented in future absorber designs (Price et al., 2002).
The double pipe concept can be modified with a secondary reflector fitted on the inner glass tube surface to catch "stray" rays from the mirrors (primary reflector). A sketch of this is presented in figure A.5b. Calculations show an increased overall performance of ∼2 % with a secondary reflector, and furthermore it allows for slacker tolerances with respect to optical precision of the primary reflector and more evenly distributed flux around the pipe circumference. However, it is estimated that the addition of a secondary reflector is still not a cost-effective modification from a cost-benefit point of view (Price et al., 2002).

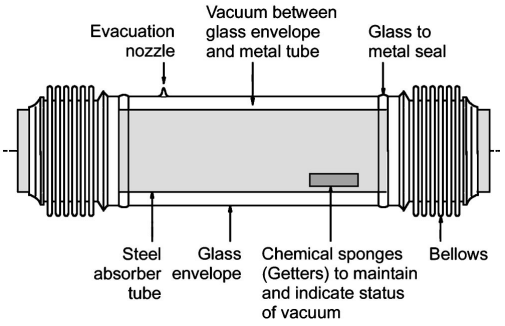

(a) *Double pipe absorber used in PTC. An evacuated glass pipe surrounds an internal pipe which carries the HTF.*

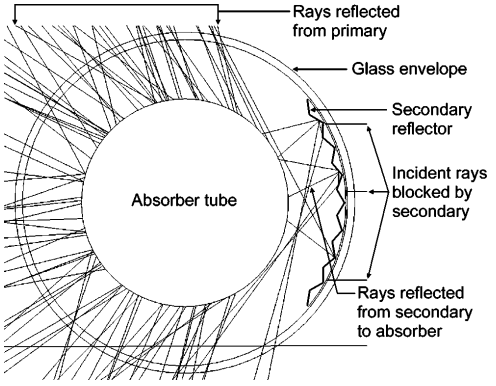

(b) *Double pipe absorber presented in a cross-sectional view to show the effect of a secondary reflector.*

Figure A.5: *Details of the double pipe absorber design. Taken from Price et al. (2002).*

Process Improvements

Traditionally, thermal oil or molten salt have been used as HTF, but recently direct steam generation by circulating water in the absorber pipe, have received increasing interest. On the up side, the expensive oil, which has a maximum operation temperature of 375 °C before it deteriorates, and the extra heat exchanger to transfer solar energy to the steam cycle, can be avoided. In addition, a lot of the extra equipment associated with using oil as HTF, such as fire extinguishing system, oil expansion tank, etc., can be dropped as well. On the down side, all piping in the PTC loop must be able to withstand high steam pressures which is associated with high costs. Furthermore, DSG is not limited to an upper temperature level, which

means that steam temperatures closer to the optimal steam temperature of 550 °C for a steam turbine can be achieved (Price et al., 2002). For example, an overall solar-to-electricity conversion efficiency of 22.6 % was reached for DSG operation with 450 °C turbine inlet steam temperature, while this was 21.3 % for a PTC plant with oil as HTF with 375 °C as inlet temperature (Zarza et al., 2004). Therefore, DSG emerges as the most competitive concept of the two, and much of the practical DSG operation experience were collected through the DISS (short for *DIrect Solar Steam*) project in Almeria, Spain. To provide the reader with an idea of the quantities involved in DGS operation mode of a PTC system, table A.1 includes details from the DISS solar field.

Property	**Value**	**Unit**
No. of parabolic trough modules	40	
Module aperture/length	5.76 / 12	m
Total row length	550	m
Surface of reflecting mirrors	3000	m^2
Absorber pipe inner/outer diameter	50 / 70	mm
Steam mass flow per row	0.8	kg/s
Max. water recirculation rate	4	
Max. outlet steam temperature	400	°C
Max. outlet steam pressure	100	bar

Table A.1: *Details of the DSG operated PTC solar field at Plataforma Solar de Almeria, Spain, in connection with the DISS project. Extract from Zarza et al. (2004).*

The project included tests of improved PTC equipment under real operation conditions, and the purpose was to investigate a commercially feasible setup for DSG in PTC, and, amongst other things, to achieve better integration of the PTC loop with the power block. For instance, experiments were carried out to identify the better of the two process configurations; *once-through* or *recirculation* which are presented in figure A.6. As expected, the easiest handling of pressure and temperature levels was achieved with the recirculation process, but reasonable control could be reached with the once-through process as well, which is shown in figure A.7. The recirculation process was found to the best choice from a financial, technical and operation and maintenance point of view even when rates of recirculation was low, which makes the use of small and cheap water/steam separators possible (Zarza et al., 2004).
Further testing of the DSG concept is needed, but so far it has proven to be a promising application in PTC technology. For instance, there still remains some concern regarding the long-term operation and maintenance aspects of the high pressure system, but so far steam production tests at 100 bar have been carried out at PSA without any problems (Price et al., 2002).

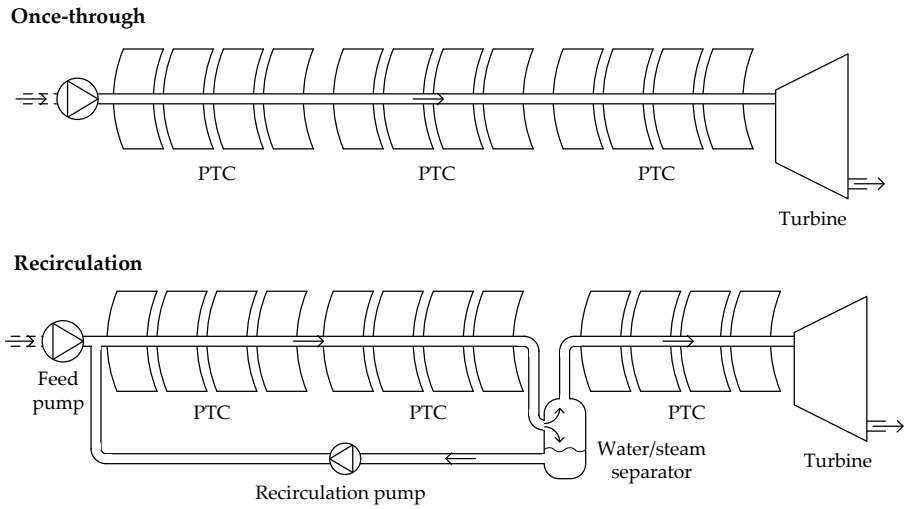

Figure A.6: *Schematics of the once through and recirculation processes of DSG. Modified from Price et al. (2002).*

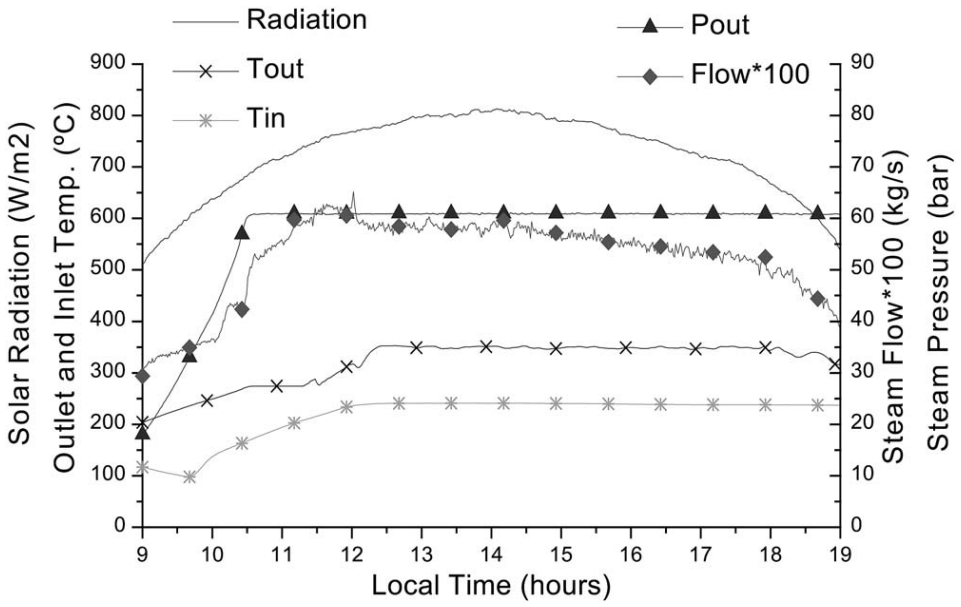

Figure A.7: *Operation in once-through mode at 60 bar. From Zarza et al. (2004).*

Appendix

B

Weight Loss and Thermal Cycling of Ternary Salt Mixture

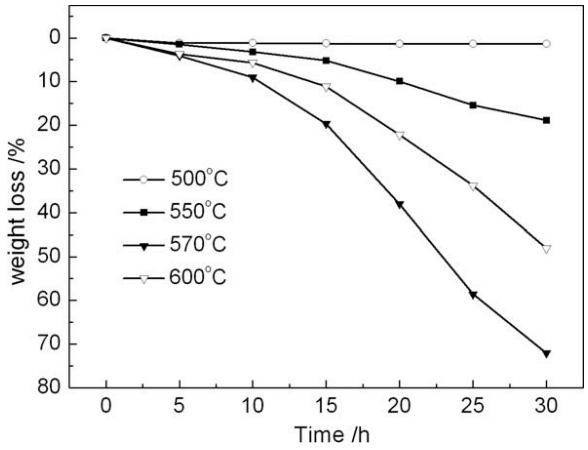

Figure B.1: *Weight loss plotted against temperature for ternary nitrate salt. Taken from Peng et al. (2010).*

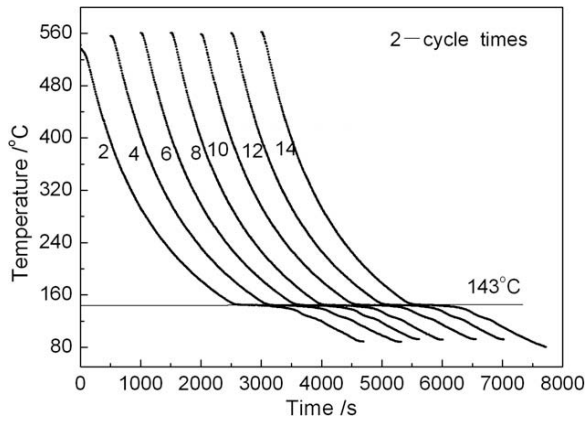

Figure B.2: *Cooling curve of 14 thermal cycles of ternary nitrate salt ($NaNO_3$, KNO_3 and $NaNO_2$, 7/53/40 mass %). Taken from Peng et al. (2010).*

Appendix

C

Steamlines in the Liquid Melt Around a Vertical Pipe

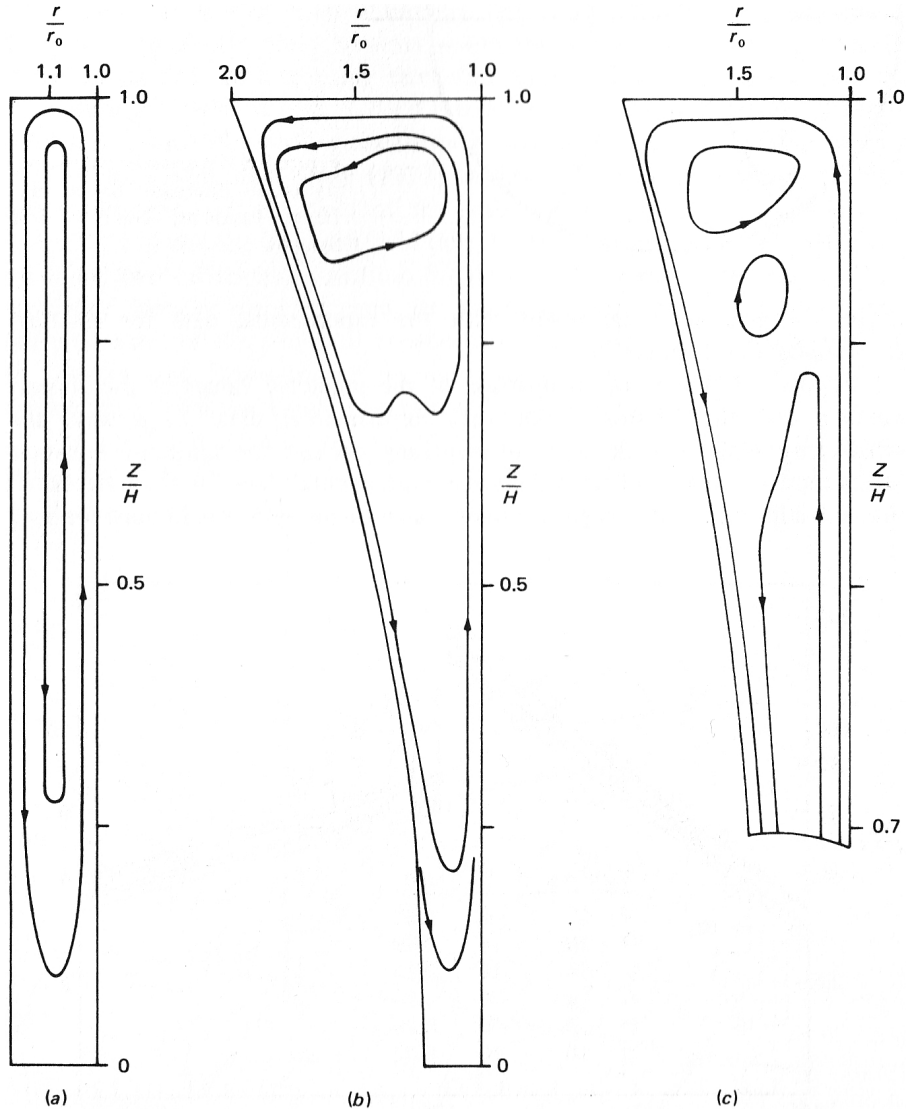

Figure C.1: *Representative streamlines of the fluid flow. (a) shows the rectangular shape of the cavity at small simulation times, while (b) and (c) clearly shows the effects of heat transfer dominated by natural convection at later times. Taken from Patankar (1980).*

Appendix

D

Practical Approach of CFD-simulations

Some of the CFD cases are quite demanding for common laptop computer to handle in terms of computational power, so all CFD simulations are carried out on the computational cluster located at The Department of Energy Technology, Aalborg University. The cluster consists of computer racks, which holds a number of individual computers or *nodes*. Through an internet connection, files needed to run a simulation on a node are uploaded to a local hard drive in the cluster as presented in figure D.1. The entire setup for a given CFD-simulation in FLUENT (grid, boundary conditions, solver settings, etc.) can be saved to a so-called *case-file*, which is uploaded to the cluster hard drive along with a couple of command files. The purpose of the command files is to do the actual execution of the calculation. Furthermore, a few directions can be given in the command files with respect to time step size, number of time steps, and allowable number of iterations per time step. This means, that a number of simulations with a varying parameter (*e.g.* different time step sizes) can be run just by writing different command files containing the parameter. These command files all refer to the same case-file hence only a single FLUENT case-file is necessary to produce a range of results, which of course is a time-saving advantage. In reality, two programs are needed to run a CFD-job on the cluster from a local PC: one for data exchange to/from the local cluster hard drive, and one for executing files on this hard drive. The first mentioned, is carried out by the freeware program WinSCP, which enables secure transfer of data between a local and a remote computer by using the *Secure Copying Protocol*. While the computational cluster runs on a Unix platform the user's laptop might be based on a different operating system *e.g.* Windows as in our particular case. Therefore, the free application PuTTY is used to handle this interconnection between two systems, which allows for instance for a user with a Windows-based laptop to execute commands in the Unix environment of the nodes on cluster. This is also presented in figure D.1. When a job is initiated through the PuTTY-interface, the case-file and command files are loaded from the local hard drive and saved to a file as prescribed in a command file once the computation is completed. The user can then copy these completed simulations onto his or hers own hard drive and analyse or post process the results.

To enable comparison of required computational time for various grid densities, dis-

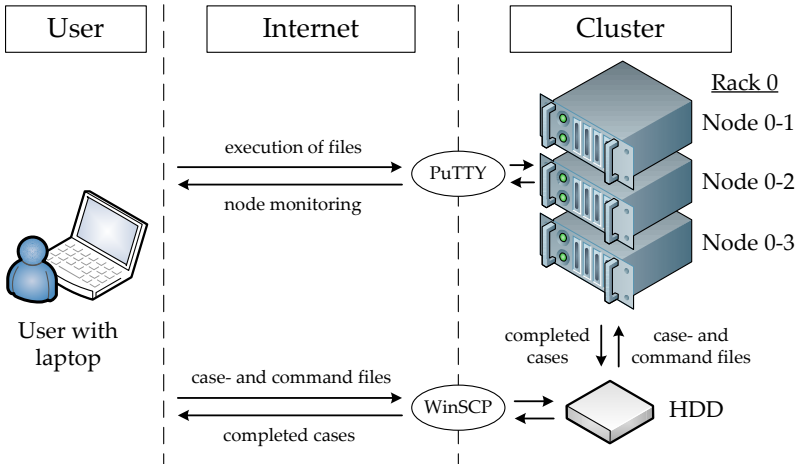

Figure D.1: *Sketch of the basic communication between a student laptop and the computational cluster at The Department of Energy Technology, Aalborg University.*

cretisation schemes, and sizes of time steps, all calculations are carried out on nodes with the exact same hardware setup, which is presented in table D.1. Only one CPU was dedicated to each simulation.

Node details	
No. of CPUs	4
CPU speed	2992 MHz
Total node memory	4047.8 MB

Table D.1: *Hardware details of the student node of the cluster used for all quasi-1D CFD simulations.*

Appendix

E

Fin Efficiency Plots

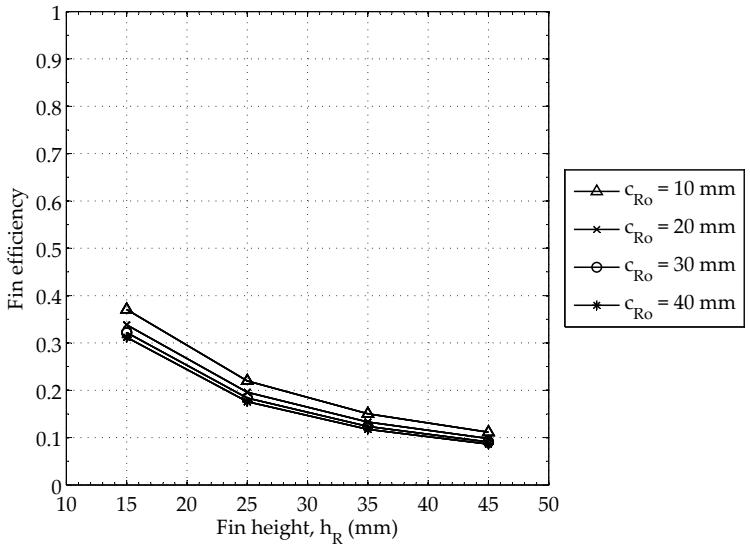

Figure E.1: *Fin efficiency vs. fin height and pitch c_{Ro}. 1 mm thick circular steel fin, discharge mode 1.*

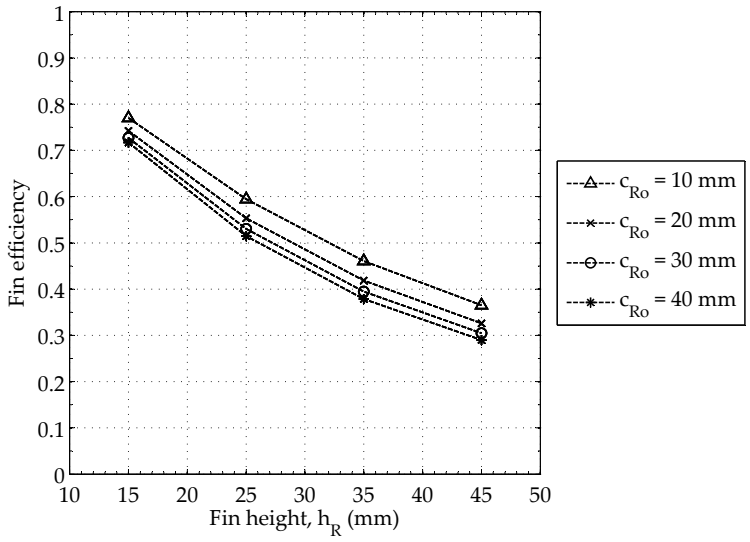

Figure E.2: *Fin efficiency vs. fin height and pitch c_{Ro}. 3 mm thick circular expanded graphite fin, discharge mode 1.*

Appendix

F

Mail Correspondence, Nitrate Salt Properties

Dear Mr. Peter,
Please find attached a paper that might help you at least with some properites you are looking for (p. 108). If you are looking at PCM storage it might also help you to contact Dr. Tamme from the DLR in Stuttgart who is working on especially that topic for a long time. Probably he has more detailed data at hand.
Could you be so kind and tell me where I can find that paper from Bayon you mentioned? We are also always interested in getting more sources for comparing our data base entries for liquid salt. PCM storage is at the moment not in our focus.

Mit freundlichen Grüßen - Best regards

Nils Gathmann

- Head of Process Development -

FLAGSOL

Flagsol GmbH
Agrippinawerft 30
50678 Koeln

Tel. +49 221 925 970-92
Fax +49 221 925 970-99

nils.gathmann@flagsol.de
www.flagsol.de

From: Nis Peter [mailto:nreinh06@student.aau.dk]
Sent: Donnerstag, 31. März 2011 02:17
To: Herrmann, Ulf
Subject: Thermophysical properties of nitrate salts

Hello Ulf,

I'm a master student at Department of Energy Technology at Aalborg University, Denmark, and along with a fellow student I'm currently engaged in a study concerning a phase change heat storage for concentrated solar power applications. In this connection, we're looking for a reliable set of thermophysical properties for a NaNO3-KNO3 50:50 mole% nitrate salt composition. So far, the only data found has been scattered across a number of different data sources/researchers.
The paper by Bayón et al. (2010) "*Analysis of the experimental behaviour of a 100 kWth latent heat storage system for direct steam generation in solar thermal power plants*", contains a list of properties in both solid and liquid state, which we need. However, it does not explicitly say where they have obtained these data, so we would like to verify these data against an additional set of data.

Are you in possession of such data or do you know were we can find it?

Figure F.1: *Mail correspondence with Mr. Nils Gathmann of Flagsol GmbH*